THE STRUCTURE AND MECHANICS OF ATOMICALLY-THIN GRAPHENE MEMBRANES

A Dissertation

Presented to the Faculty of the Graduate School

of Cornell University

in Partial Fulfillment of the Requirements for the Degree of

Doctor of Philosophy

by

Arend van der Zande

May 2011

THE STRUCTURE AND MECHANICS OF ATOMICALLY-THIN GRAPHENE MEMBRANES

Arend van der Zande, Ph.D.

Cornell University 2011

Graphene is an exciting new atomically-thin two dimensional system with applications ranging from next generation transistors, to transparent and flexible electrodes, to nanomechanical systems. We study the structure, electronic, and mechanical properties of suspended graphene membranes, and use them to produce mechanical resonators.

We first showed that it was possible to produce suspended graphene membranes even down to one atom thick using exfoliated graphene, and resonate the membranes using optical interferometry. The resonators had frequencies in the MHz and quality factors from 20-850, but showed no reproducibility.

In order to produce predictable and reproducible graphene resonators we developed methods for making large arrays of single-layer graphene membranes of controlled size, shape and tension using chemical vapor deposition (CVD) grown graphene. We used transmission electron microscopy to study the polycrystalline structure of the graphene, we found that the different grains stitched together by disordered lines of 5-7 defects. Using electron transport and scanned probe techniques, we found that the polycrystalline grain structure reduces the ultimate strength of the graphene, but did not as strongly affect the electrical properties.

We systematically studied the mechanical resonance of the single-layer CVD

graphene membranes as a function of the size, clamping geometry, temperature and electrostatic tensioning. We found that the CVD graphene produces tensioned, electrically conducting, highly-tunable resonators. In addition we found that clamping the graphene membrane on all sides reduces the variation in the resonance frequency, and makes the behavior more predictable.

BIOGRAPHICAL SKETCH

Arend van der Zande was born on December 27, 1981 in Santa Cruz, California. Arend showed an inclination for math and science from an early age. A report card from the sixth grade reads "Arend is a very good student. He really gets IN to his experiments". By which the teacher meant that he usually left the classroom dripping with something. Arend chose to follow an unusual educational path. Rather than go to highschool, He took the high school equivalency exam at age 14, and started taking classes at Cabrillo Community College. After a year, he transferred to the University of California, Santa Cruz. He majored in Physics and Mathematics, and spent summers doing research at the Santa Cruz Institute for Particle Physics, (SCIPP), Columbia University, and University of Washington. After finishing his undergraduate degree Arend started a PhD in Physics at Cornell University. He shortly settled on working with Professor Paul McEuen studying nanomechanics of carbon systems. After graduating, he will take 2 months to travel the world, then work as a post-doc with Professor Jim Hone at Columbia University.

ACKNOWLEDGEMENTS

This thesis is the product of contributions, both academic and social, from a huge number of people.

First and foremost, I want to thank Professor Paul McEuen for being the prime example of a good advisor and a good scientist. I am constantly impressed by his deep insight and how he is able to pull the core idea from a complex set of facts and observations, as well as his patient guidance and courage to stare uncertainty in the face.

There are a few other people who deserve special note for what they have taught me and their contributions to this work. The first person is Vera Sazonova, who trained me and set me on the path of nanomechanics. Her exceptional talent and unwavering scientific ethic have served as prime example to me on how to approach tangled data sets with honesty and multiple perspectives. I will not discuss the work that she and I collaborated on in this thesis, but I still use the techniques I learned with her every day.

Next are Scott Bunch, who got me started on graphene, and Scott Verbridge, a graduate student in the Craighead/Parpia group and an expert in optically detected nanomechanical systems. The Scotts and I had very fruitful collaboration studying the first exfoliated graphene resonators. I greatly admire Scott Bunch's "just do it" attitude as well as Scott Verbridge's patient systematic approach and try very hard to emulate them both.

This collaboration formed the foundation for the Graphene Interdisciplinary Research Group (IRG) in the Cornell Center for Materials Research (CCMR), and I have continued to push it forward even after the Scotts moved on. Of particular help in this uphill battle were Rob Barton, Jonathan Alden, and Carlos Ruiz-

Vargas. Together the four of us had to work through the challenges of reliably creating and manipulating a suspended single layer of atoms which was a much more daunting task then we originally realized. Jonathan's unbeatable ability to characterize complicated processes, Carlos' creative out of the box thinking, and Rob's cheerful willingness to try out all of our crazy ideas have pushed our work forward in a way that would not have been possible alone.

Finally, Pinshane Huang showed us all how powerful electron microscopy is and what being able to look at what you are working with on the nanoscale can allow you to do. Pinshane, Carlos, and I collaborated together to understand graphene on a level that I thought previously impossible. Pinshane's proactive learning and motivation make her technical knowledge and productivity far exceed her experience. I constantly wish that I had a bit of more of those habits when I got started, and will take her approach with me to the future.

Many professors have contributed their experience and resources to get this work done. Of particular note, Jeevak Parpia and Harold Craighead have supported our strange studies of graphene with their optical interferometry setups, and graduate students. Without their support none of this work would be possible. Jiwoong Park has been instrumental in pushing the Carbon nanosystems studies forward at Cornell. His energy and organization have pulled together a few scattered graphene and carbon nanotube researchers at Cornell into a 50+ person supergroup which is one of the centers of graphene/nanotube research in the world. David Muller has brought his incredible experience with electron microscopy to the table. I usually come away from discussions with him with many new ideas to try. Tomas Arias and Alan Zehnder and their students have helped me make sense of nonsensensical data on nanomechanics. David Tanenbaum has showed me that

there are other kinds of professorships than the ivy league super-prof, and that it is possible to be involved in world class research at a liberal-arts college. Rena Zieve taught me low temperature physics. Earlier in my career, David Dorfan at UC Santa Cruz, Stefan Westerhoff at Columbia University, and Gerald Seidler at University of Washington set my steps on the research path.

I have had many opportunities to work with many talented researchers in my graduate career. All of the members of of the McEuen group: Jun Zhu, Yuval Yaish, Shahal Ilani, Xiaodong Xu, Yaqiong Xu, Patrycja Paruch, Ken Bosnick, Ethan Minot, Markus Brink, Vera Sazonova, Sami Rosenblatt, Scott Bunch, Lisa Larrimore, Xinjian Zhou, Luke Donev, Nathan Gabor. I have enjoyed your friendship and learned a lot from each of you. I know I am leaving the lab in good hands with Samantha Roberts, Jonathan Alden, Melina Blees, Arthur Barnard, and Isaac Storch.

I have many more collaborators who also deserve acknowledgement: Chris Hensley in the Gaeta Group; Ferdinand Kuemmeth, Kirill Bolotin, Sufei Shi, Josh Parks, Eugenia Tam and Wan Li from Ralph Group, Judy Cha, and Pinshane Huang from the Muller Group; Carlos Ruiz-Vargas, Mark Levendorf, Adam Wei Tsen, and Lihong Herman, Mike Segal, and Lola Brown from the Park Group; Jennifer Rieser and Huolong Zhuang from the Hennig Group; Robert Reichenbach, Scott Vebridge, Darren Southworth, and Robert Barton from the Craighead/Parpia lab, and Josh Kevek from the Minot Lab.

I have had the opportunity to mentor many talented undergrads during my time here. Ian Frank and Scott Berkley came from Pomona and did much of our early work with making pushing on exfoliated graphene membranes and are now in graduate school at Harvard and Columbia respectively. Phi Pham and William

Whitney set up our CVD graphene furnace and provided an unending supply of graphene to many groups at Cornell. Peijie Ong, Alex Ruyack, and Si Ping Wang will continue the healthy tradition of learning and support that we have developed. I cannot tell you the pride I feel to see them growing up as scientists and succeeding in their new fields.

Without the unbeatable shared facilities at Cornell, none of this work would be possible. I cannot count the number of times I have said "I wish we had X" only to find that there was a state-of-the-art facility with free training and experienced staff down the street. I owe huge debts to Rob Ilic, Michael Skvarla, Meredith Metzler, and Gary Borndonaro at the CNF; Kit Umbach, John Grazul and Mick Thomas at the CCMR, and John Shu at the CNS.

Outside of work, I owe a lot to the friends and housemates who have made my time at Cornell an enjoyable one with lots of personal growth.

I fondly look back on all of the housemates who have supported my crazy work schedule and propensity for both adventures and misadventures. Simon, Shira, Sarah, Sinja, Joern, Duane, Jonathan, Melina and Pinshane. You have turned a house into a home and have become my family.

After seven years at a university, with its transitory lifestyle, I can't count the number friends that have come and gone. I have many fond memories of time spent with the Physics Cohort, The Ranchers, The Crammies, The Brewing Conspiracy, The SC crew and many others. In particular, I want to acknowledge the driving forces behind those groups Attila, Brooke, James, Mark, Gordon, Ben, Sharon, John, Matt, Ryan, Mike, Annie, Ben, Gretchen, Cloe, Heather, Ben, Punita, Sarah, Madeline, Milan, Caroline, Kavita, Bruno, Nhu, Lucy, Jack, Ivan, Nadia, Kassie, Eliott, Srikant, Chin, Avtar, Catherine, Janelle, Kevin, Noah and

many more. You have all touched me, and changed my view of the world.

My family has shown remarkable love, support and patience even though I have chosen to live far from home. My parents Ed and Irene, my sister Chantal, my brother in law Brian, my niece Svea, as well as my grandparents, aunts, uncles, and cousins. I love you all.

Finally, this work could not have been performed without the financial support of several government grants. In particular, my work has been supported for many years through the NSF by the Cornell Center for Materials Research.

TABLE OF CONTENTS

LIST OF FIGURES

Chapter 1

Introduction

1.1 Introduction

I make and play the smallest musical instruments in the world. At least, that is what I tell people at cocktail parties. More specifically, I build nanomechanical systems out of graphene, and use them to examine the structure and mechanical properties of this material. I take this knowledge, use it to build structures that have never existed before, and manipulate them in new ways. This thesis is about building, playing, understanding, controlling, and using these tiny new instruments.

First, let me answer the question of why we do this.

1.2 Principles of Nanoscience

Science is all about understanding and controlling the world around us. This cycle of understanding and control is what drives human progress. The understanding allows us to appreciate how the world works and develop new tools for controlling all of the different aspects of nature . Improved control brings the ability to understand new things, and new technologies to improve our lives. For example, understanding and controlling purity of materials and the interaction of mechanical forces has led to our being able to construct larger and ever more complicated structures such as the bridge shown in Figure 1.1a.

Nanoscience is all about understanding, controlling, and manipulating objects and materials on ever finer size scales, down to the nano scale. Nano scale refers to the size of objects, with one nanometer being 10^{-9} meters, or about 10 times

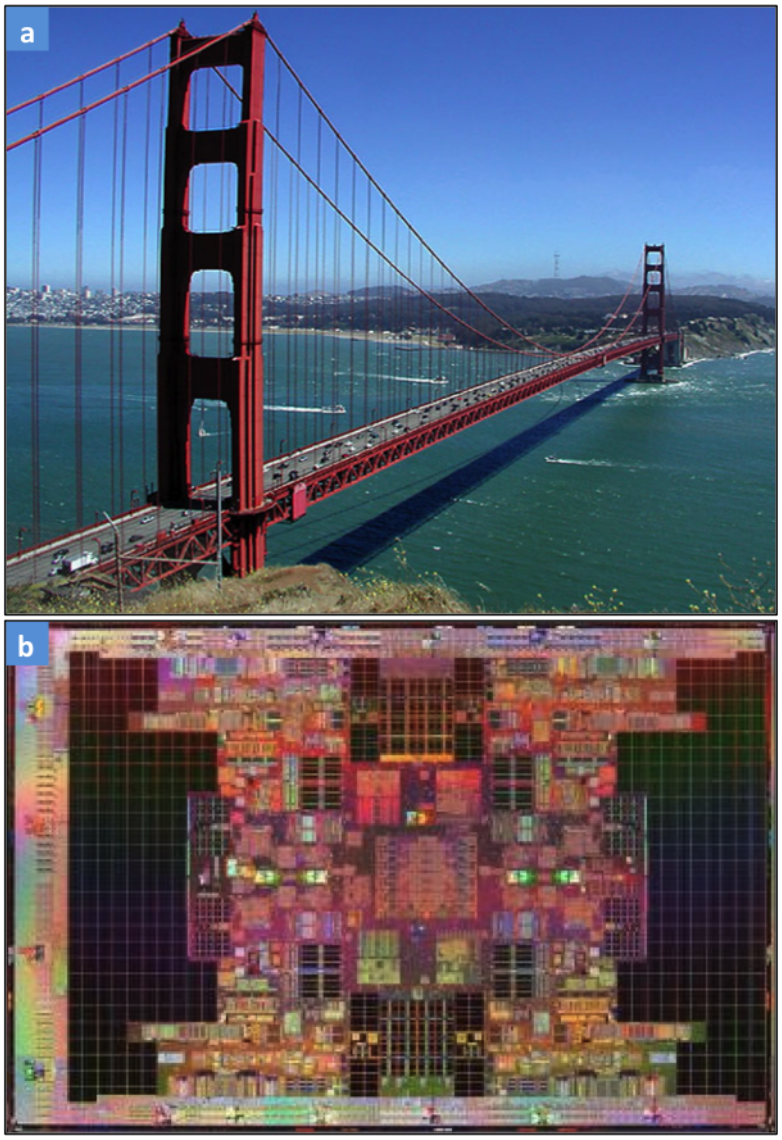

Figure 1.1: a) The Golden Gate Bridge b) Optical picture of an Intel computer chip. This chip contains 2 billion transistors on an object the size of a postage stamp.

the size of a hydrogen atom.

This new science has brought with it a new kind of complexity. Rather than building larger, more complex structures, we are fitting more complex structures into smaller and smaller spaces. The most famous example of this up until now is the computer chip, such as the one shown in Figure 1.1b. The understanding and control of how to manipulate the flow of electrons on the nanoscale has allowed us to build billions of transistors onto an object the size of a postage stamp, a feat of engineering easily on par in complexity with constructing an entire city.

Of course, computer chips are only one application of nanotechnology. There are many different subfields. Each field deals with different aspects of nature and how we control it on the nanoscale. For example: Nanomaterials is the field creating nano sized objects with novel properties not found in macroscale materials; Nanoelectronics and nanophotonics are the fields of manipulating the flow and interaction of electrons and photons on the nanoscale; Nanomechanics is the field of making structures vibrate and move on the nanoscale.

1.3 Nanotechnology from the top-down versus the bottom-up

So how does one make a nanoscale system? There are two different approaches – Working from the top down or building from the bottom up. The top-down approach uses lithography and CMOS techniques to pattern bulk materials into nanoscale elements like transistors, solar cells, waveguides, or suspended mechanical beams. This approach has traditionally been used in nanotechnology. For example, the computer chip made in Figure 1.1b was made with this approach. There are two downsides of the top-down approach. First, patterning smaller and smaller features using lithography room size tools becomes prohibitively more and

more difficult. Second the properties of materials change when they get very small. Below a certain size, the electrical conductivity, and mechanical strength, and even the structural integrity of bulk materials begins to degrade, which puts limits on the size of structures we can fabricate.

The bottom-up approach starts with nanoscale materials and builds them up into electrical, optical, and mechanical circuits. The difference between these two approaches is analogous to using bricks to build a house versus carving a statue out of a marble block.

There are many different nanoscale materials that are being studied as candidates for building blocks. For example, research groups are actively studying various materials such as metal nanoparticles as well as synthesized or biological molecules to find ways of integrating them into nanotechnology. The main requirement for such materials is that they must be mechanically stable structures down to the nanoscale. Beyond that, the requirements depend on the desired application. Generally desirable traits are materials that are conducting or semiconducting, materials that absorb or emit light, materials that are mechanically very strong, and materials that are easy to make and manipulate. One material that is especially promising is graphene.

1.4 Graphene

Graphene is a sheet of carbon atoms bonded into a flat hexagonal lattice that is only one atom thick, as shown schematically in Figure 1.2. Because it is only one atom thick, graphene is the prototypical two dimensional (2D) system.

Graphene has exceptional electrical, optical, and mechanical properties that make it perfect for many applications. Applications currently being researched range from next-generation transistors (Figure 1.3a) to transparent electrodes[18],

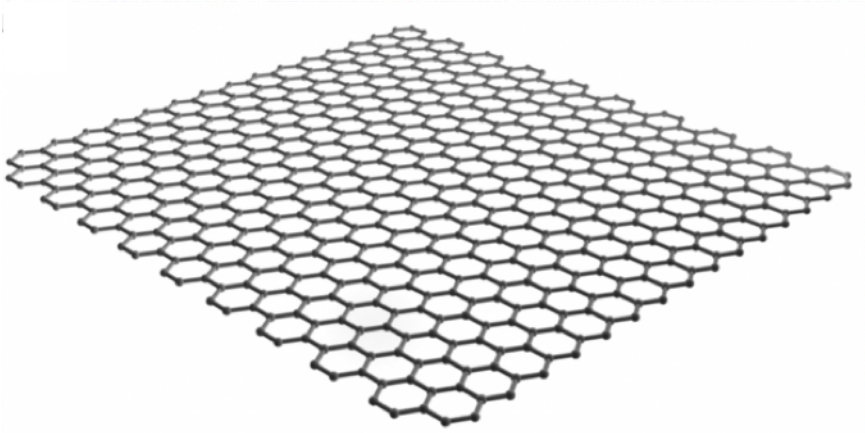

Figure 1.2: Graphene is a sheet of sp-2 bonded carbon atoms arranged in a hexagonal lattice that is only one atom thick.

flexible electronics (Figure 1.3b)[19], atomically thin imaging substrate[20], membranes for nanopore DNA sequencing[3, 4] (Figure 1.3c), and nanomechanical systems (Figure 1.3d). In Chapter 2, we will summarize graphene's exceptional properties and explain how these properties relate to its potential applications.

With all of the excellent electrical and mechanical properties of graphene, it is important to not lose sight of its most wonderful property: graphene is a truly 2D material. It is impossible to make a stable crystal which is thinner than graphene. This wonderful property makes graphene an excellent material both for pushing well established fields such as nanoelectronics and nanomechanics to their ultimate limit to see what happens and for making novel systems taking advantage of these two dimensional membranes.

1.5 A brief history of graphene

One of the most impressive aspects of graphene research is how quickly the field has progressed from the first time graphene was isolated, to becoming the most studied material in physics, to its mass production and use in applications.

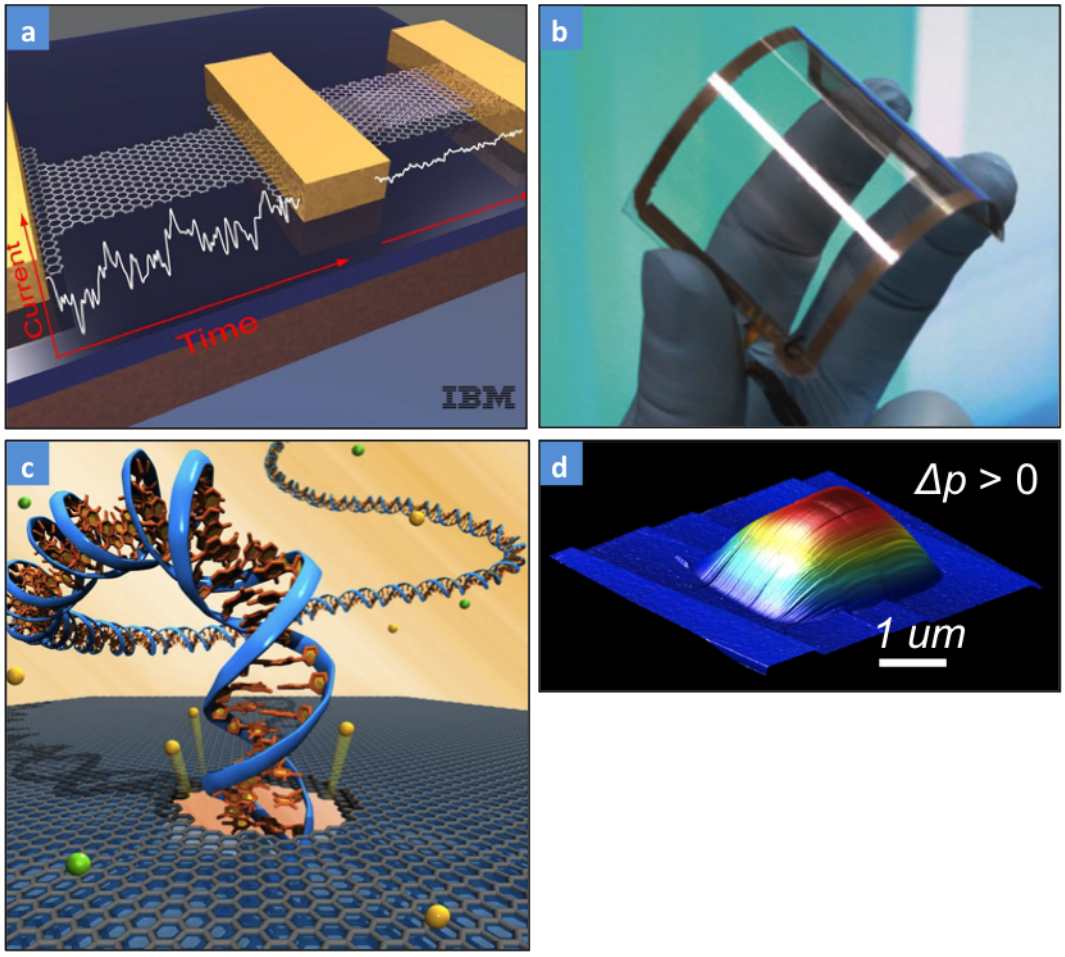

Figure 1.3: a) Single-layer and bi-layer graphene transistors[1]. b) Graphene based circuit on a plastic substrate. The graphene is a transparent, flexible electrode[2]. c) DNA passing through a nanopore in a graphene membrane[3, 4]. Nanopores are being used for next generation DNA sequencing. c) AFM image of a graphene membrane flexing under gas pressure[5]

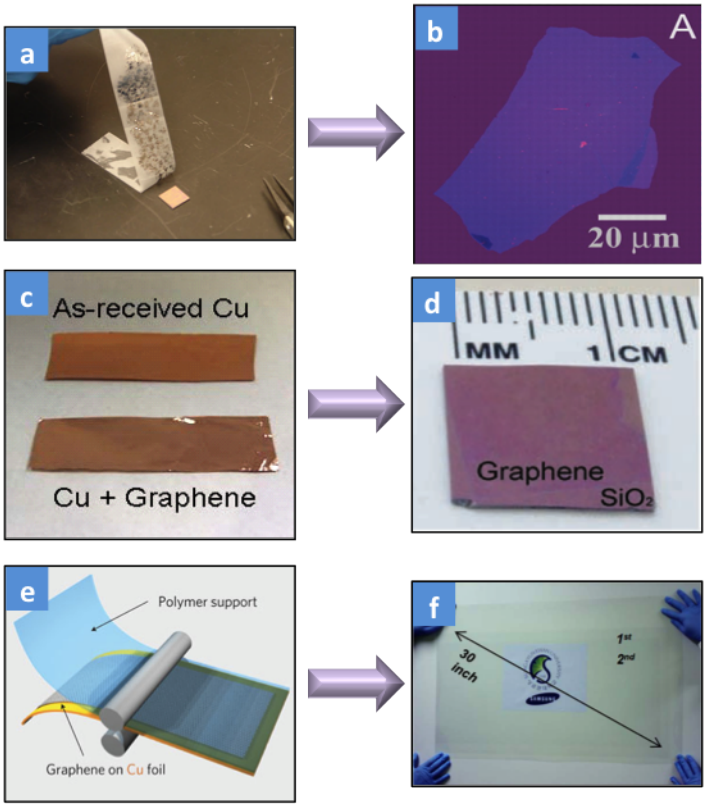

Figure 1.4: a) Mechanical exfoliation process, with scotch tape. b) Graphene on silicon oxide from mechanical exfoliation. c) copper foil with Graphene grown on it[6] d) Large area single-layer graphene transferred on to a silicon piece. e) Using roll-to-roll production to transfer meter scale graphene on to other substrates[2]. f) Meter scale single-layer and bi-layer graphene on a flexible plastic substrate.

Graphite has been around for a long time and is an extremely well-understood material. Even graphene was being made for quite a few years before it was "discovered." Research groups have been growing few-layer graphene on Silicon Carbide[21], and single-layer graphene on metal substrates like Indium and Rubidium[22] for many years. The challenge was to get pristine graphene on to an insulating substrate, making it possible to measure its predicted excellent electronic properties. Several research groups, including the Kim group, Geim group, and McEuen group were trying to do this by taking graphite, which is basically many stacked layers of graphene, and breaking it up by patterning graphite into nanopencils and exfoliatiing them on a surface or dissolving graphite into liquid dispersions[23].

However, it was not until 2004 that the technique for isolating graphene that proved to be successful was developed. Konstantin Novoselov and Andrei Geim managed to isolate few-layer graphene on an insulating substrate for the first time[24] using a remarkably simple technique. First, they took Scotch tape and rubbed graphite on it (See Figure 1.4a). Next, they pushed the tape down onto an oxide surface and looked at it under a microscope. Most of the time, they would find a micron scale piece of graphene on the surface (Figure 1.4b). They used this technique, now referred to as the Scotch tape technique, or mechanical exfoliation, to make graphene and measure the electronic transport of few-layer graphene[24]. A year later, they managed to isolate a single layer of atoms[25], and they and the Kim group at Columbia measured the quantum hall effect in graphene[26, 27]. After that, dozens of research groups started to measure every aspect of graphene's properties.

However, the Scotch Tape technique only produces small amounts of graphene at a time (a few micrometers on a side). There is no control over where to put the graphene or the shape and size of the graphene pieces produced. While these

small flakes are fine for many simple experiments and proof of principle, they are useless for more complicated experiments and for almost any application.

Much of the research on graphene has focused on scaling up production to be able to make large area single-layer graphene. The most promising technique up to date was discovered in 2009. Several groups found that it was possible to use Chemical Vapor Deposition (CVD) to grow few-layer graphene on nickel[28, 19], or single layer graphene on copper foil [6] (Figure 1.4c). The incredible utility of these techniques is that we can also transfer the graphene off the metal on to any arbitrary surface (Figure 1.4d). This technique has exploded in popularity and groups are already using it to start producing single-layer graphene by the meter(Figure 1.4e-f)[2], . In less than a year, production of graphene went from square micrometers at a time, to square centimeters at a time, to square meters at a time. The only limitation seems to be the size of the copper foil that will fit inside of a CVD furnace. We will explain how to make both exfoliated and CVD-grown graphene in much more detail in Chapter 3.

However, with this rapid advance, several questions have gone unanswered. While we know that the graphene being produced by CVD is only one atom thick, very little has been understood about how it grows, what its final structure is, and how it is different from graphene made from mechanical exfoliation. We answer these questions in Chapters 4.

In addition, the new techniques offer us a new opportunity. CVD-grown graphene is a bottom-up synthesized material (the growth is self-suppressed at one atom thick). However, it is a two-dimensional material, which means that it can be shaped and manipulated using the top-down tools developed for CMOS. In other words, graphene offers the advantages of a bottom-up material, with the ease of fabrication of a top down process making it an excellent and easy material

to incorporate in to nanotechnology.

In December 2010, Andre Geim and Konstantin Novoselov, the researchers who developed the Scotch tape technique and have since provided large body of work characterizing many of the properties of graphene, won the Nobel Prize in Physics. Interestingly, this is the third major science award for carbon allotropes. Richard Smalley, Sir Harold Kroto, and Robert Curl won the Nobel Prize in chemistry in 1996 for discovering buckeyballs, and Sumio Iijima won the Kavli Prize in nanoscience in 2008 for characterizing carbon nanotubes. These systems all come from the same base material, but have been folded up in different ways to produce 2D, 1D and 0D systems.

1.6 Nanomechanical Systems

This thesis is about using graphene to produce new nano-mechanical, or nano-electro-mechanical systems (NEMS), which are nano scale objects that flex, move, rotate, or vibrate. Figure 1.5 shows a few different examples of the wide variety of shapes and sizes of different kinds of NEMS. NEMS are useful for electrical signal processing as nanoscale switches, filters, and oscillators, and as small scale manipulators of light or fluid flow[8, 3, 4]. Due to their small size, NEMS respond very strongly to changes in their environment, making them useful in understanding the nature of forces [29], and mechanics[9, 30] on very small length, energy, and time scales. They also have practical applications as tiny ultra-sensitive sensors for measuring acceleration, strain, gas pressure, electrical charge, and the presence of molecules.

Because NEMS are mechanical elements, they obey the rules of mechanical objects, namely, Hooke's law and Newton's 2nd law.

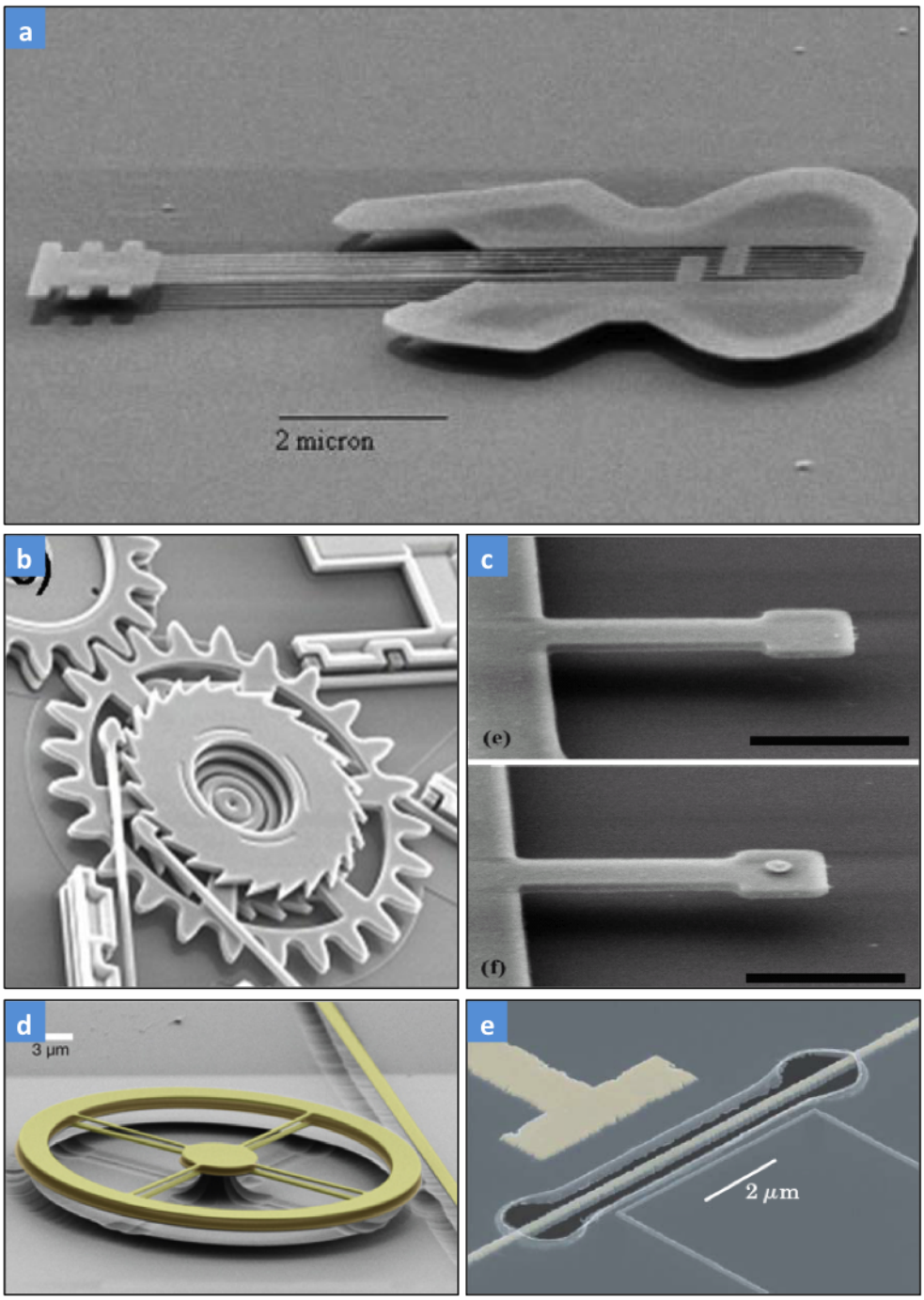

Figure 1.5: a) A silicon nanoguitar (Credit Dustin Carr). b) Micromechanical gears. (http://www.mems.sandia.gov/) c) Cantilever for mass sensing[7]. d) Mechanical ring resonator coupled to a waveguide[8]. e) Mechanical resonator coupled to a single electron transistor for quantum limited motion detection[9].

$$F = -kz \tag{1.1}$$

$$F = ma \tag{1.2}$$

These two familiar equations state that two parameters play a role in how responsive a system is to mechanical forces F: The mass m, and the spring constant k. In order to make a system as responsive as possible to changes in its environment, we want make both k and m as small as possible. The easiest way to do this is simply to make the whole system as small as possible. Traditionally, this has been done using top-down design, cutting mechanical systems out of bulk materials. As we have already discussed, this approach has serious limitations. We will approach this problem from the other direction by using graphene. Graphene provides the ultimate limit in thickness, making it an ideal candidate for making ultra-sensitive mechanical systems.

Unfortunately, making and resonating graphene membranes is not as simple as shrinking a musical instrument down and listening to the sound it makes. For one thing, plucking a nanoscale instrument with your fingers is not possible. Instead, we need to use photons and electrons to induce motion in the membranes. In addition, for the same reason that a violin has higher notes than a cello, as you make an instrument smaller, the resonance frequency f_0 rises as well, following the relation

$$f_0 = \frac{1}{2\pi}\sqrt{\frac{k}{m}} \tag{1.3}$$

For nanoscale instruments, this means that the mechanical resonance frequencies will be in the Megahertz to GigaHertz range, much larger than the 20-20,000 Hz we can hear with our ears. However, these are exactly the frequencies being

used to operate modern electronics, which makes NEMS an excellent choice for radio frequency signal processors, such as oscillators and filters. In this context, when we discuss the "sounds" that the instrument makes, we are referring to changes in electronic currents, or changes in optical reflection happening at radio frequencies as a result of the nanoscale motion, not to sounds that we can hear with our ears.

1.7 Thesis Summary

The questions that a researcher needs to ask when building nanomechanical systems are almost identical to the questions that a violin maker would need to ask in the 16th century.

- What materials do we use to make the instrument?
- How do we work with the material to build the instrument?
- What are the properties of the material?
- How do we play the instrument?
- How does the instrument sound?
- Why does the instrument sound the way it does?
- How do we control the sound, and produce the sounds that we want?

These questions form the basis for the research of this thesis.

Over the course of this thesis, we used the new 2D material of graphene and found that we were able to use mechanical exfoliation to suspend it over a trench for the first time. We used the graphene to form doubly-clamped drumheads with thicknesses down to a single layer of atoms and resonate the membranes using

optical interferometry. The single-layer and few-layer graphene resonators had frequencies in the MHz and quality factors from 20-850, but showed no reproducibility or predictability. Further experiments studying the shape of the eigenmodes of the resonator taught us that the reason for the unpredictability of the resonators was that small non-uniformities in the in-plane tension changed the shape of the eigenmodes from the predicted doubly-clamped beam modes to modes where the motion was greatest along the free edges.

In order to produce predictable and reproducible graphene resonators, we developed methods for making large arrays of single-layer graphene membranes of controlled size, shape, and tension using chemical vapor deposition (CVD) grown graphene. Using electron microscopy, we found that CVD-grown graphene is polycrystalline, with many grains of different size and crystal orientation. The grains of different crystal orientation stitched themselves together with a disordered line of 5-7 defects. Using electron transport and scanned probe techniques, we found that the polycrystalline grain structure reduced the ultimate strength of the graphene, but did not as strongly affect the electrical properties.

We systematically studied the mechanical resonance of the single-layer CVD graphene membranes as a function of the size, clamping geometry, temperature, and electrostatic tensioning. We found that the CVD graphene produces tensioned, electrically conducting, highly-tunable resonators. In addition, we found that clamping the graphene membrane on all sides reduces the variation in the resonance frequency, which makes the behavior more predictable.

1.7.1 Outline of thesis

In Chapter 2, we summarize the electrical, optical, and mechanical properties of graphene and how they relate to its potential applications. In Chapter 3, we discuss

how we make graphene, how we fabricate suspended graphene membranes, and some standard techniques that the graphene community uses to characterize the quality and structure of graphene. In Chapter 4, we examine the grain structure of graphene membranes grown by chemical vapor deposition and go on to examine how the grain boundaries affect the graphene mechanically and electrically. These measurements point the way towards understanding how to grow graphene on very large length scales. In Chapter 5, we discuss how to mechanically resonate a single sheet of atoms and some early results and lessons learned studying exfoliated graphene resonators. In Chapter 6, we systematically study the properties of many graphene resonators and gain control over the tension and quality factor.

Chapter 2

Graphene structure and properties

In the following chapter we will describe the structure of graphene, and then review its exceptional electronic, optical, and mechanical properties to demonstrate why we are interested in using it in nanosystems.

2.1 Structure of Graphene

Everyone is familiar with the two bulk crystals that are formed purely from carbon atoms. Diamond and graphite (Shown in Figures 2.1a-b) are well-understood materials that have been in use for millennia. What exactly is graphene and how does it relate to these well-known materials? The following review borrows strongly from Scott Bunch's Thesis[31] , Andrei Geim's review "The Rise of Graphene"[10], and Saito, Dresselhaus et al[32].

By looking at a periodic table, we see carbon has four valence electrons in the 2s, $2p_x$ $2p_y$ and $2p_z$ orbitals and two tightly bound electrons in the spherically symmetric 1s state. The valence electrons have very similar energies, which allows them to mix easily to form hybridized states. Which hybridized states are formed determines the solid-state properties of carbon structures.

There are two stable pure-carbon crystals. In the first arrangement, carbon is bonded in a sp3 hybrdized state. Each carbon atom forms 4 covalent C-C bonds of 1.54 Å in a face-centered cubic atomic lattice, shown schematically in Figure 2.1c. This lattice forms the 3D bulk crystal diamond. Because there are no free electrons, undoped diamond is a wide-band-gap insulator. In addition, the carbon-carbon bond is one of the strongest bonds in nature, which leads to diamond having an extremely high Young's modulus of $Y = 950$ GPa and thermal conductivity.

The second stable atomic arrangement is carbon bonded in a sp2 hybridized state. Each carbon atom has 3 covalent C-C bonds of 1.42 Å in the x-y plane, leaving one perpendicular, dangling $2p_z$ orbital. This dangling bond combines with its nearest neighbors to form the π orbitals. The sp2 bonded carbon atoms combine together to form a 2D hexagonal lattice shown in Figure 2.1d, which we call graphene. The sp-2 covalent bonds give the graphene its mechanical strength, and the π orbitals make the graphene conducting.

However, because graphene is a 2D membrane in a 3D space, there is more than one stable configuration in addition to the flat one-atom-thick membrane. By stacking sheets of graphene on top of each other, as shown in Figure 2.1e, we get graphite. The π orbitals between the different graphene layers only interact weakly, so the layers are only held together by a weak van der Waals attraction. This weak inter-layer coupling is what makes the graphite in pencils write so effectively.

In addition to graphite, we can imagine taking a sheet of graphene and rolling it up in to a cylinder, as shown in Figure 2.1f. We call these cylinders carbon nanotubes. Carbon nanotubes are the 1D cousin to graphene and they share many of graphene's excellent properties.

Finally, if we roll a graphene sheet into a ball rather than a cylinder, as shown in figure 2.1g, we get a Buckminsterfullerene. Fullerenes are the 0D cousin to graphene.

2.1.1 Thickness in Flatland

We need to make one important note about dimensionality. Unlike most materials, where thickness is defined as the spacing between the top and bottom atoms, graphene is only one atom thick. Instead of a top and bottom atom, it has a top and bottom π electron orbital. This means that graphene does not have a well-

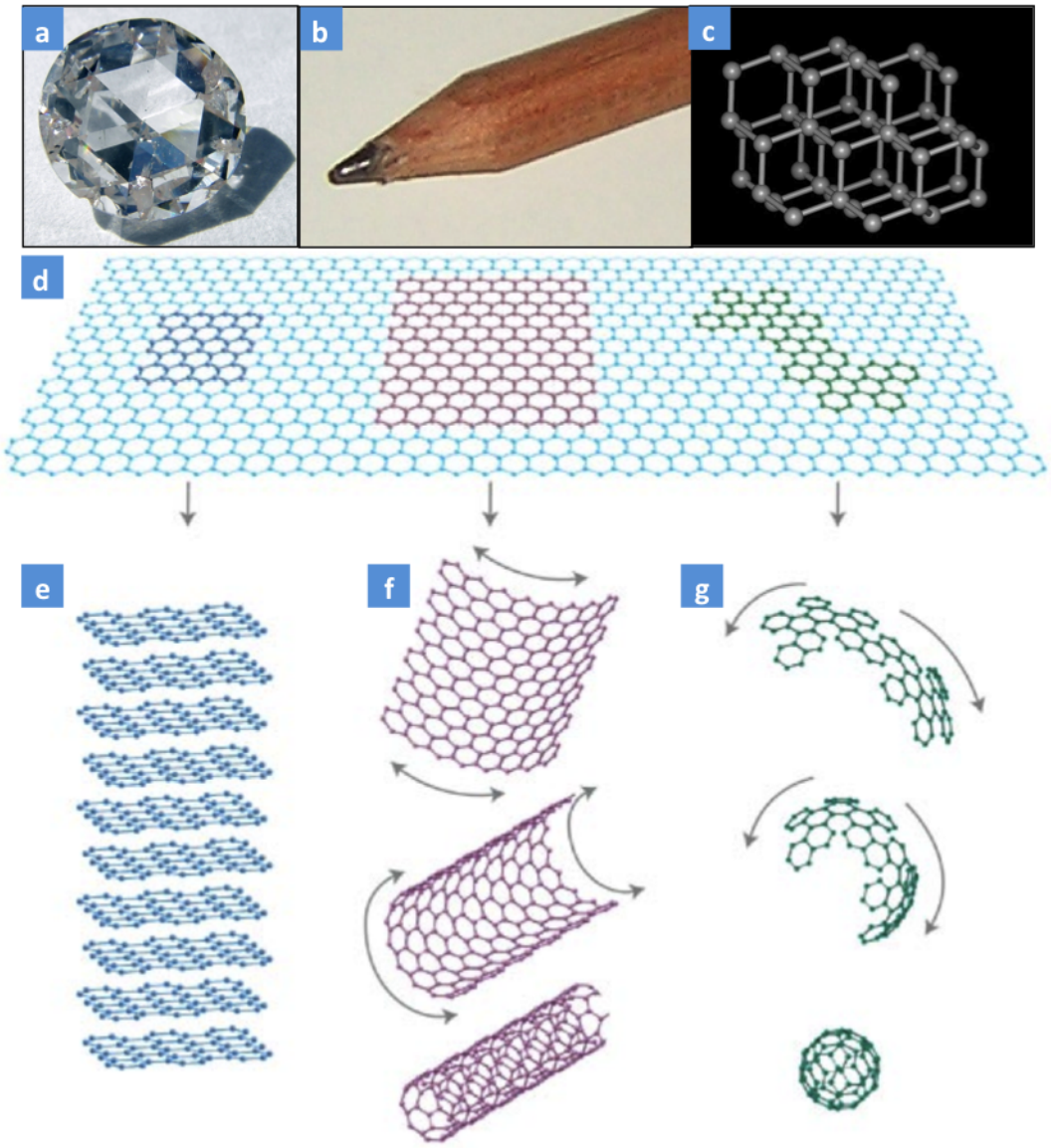

Figure 2.1: a) The Hope Diamond. b) Graphite at the tip of a pencil. c) Schematic of the crystal structure of diamond. The balls represent carbon atoms, and the lines connecting them represent covalent bonds. d) Schematic of the crystal structure of graphene. e) Schematic showing a stack of graphene sheets, also known as graphite. f) Schematic of how to roll up a graphene sheet to form a carbon nanotube. g) Schematic of how to roll up a graphene sheet to form a C-60 Buckminsterfullerene. Figures d-g from[10]

defined thickness, as electron orbitals are a quantum mechanical wavefunction that does not have a well-defined beginning and end. This has implications on the electrical, optical, and mechanical "bulk" properties of graphene.

In most cases, researchers can simply ignore this issue by simply using an effective thickness and defining all parameters in terms of this value. This effective thickness is typically taken to be the interlayer distance of graphite $t_0 = 3.42$ Å. However, in some cases, such as relating the bending and stretching moduli of graphene, using this effective thickness leads to incorrect results.

In order to avoid this pitfall, throughout this thesis, we will use the 2D incarnations of all parameters that depend on dimensionality, such as current density, conductivity, strain, Young's Modulus, etc. For example, when discussing the density of graphene we use $\rho_0 = 7.4 \times 10^{-7}$ kg/m^2. This is related to the density of graphite by

$$\rho_{3D} = \frac{\rho_0}{t_0} = 2163 \text{ kg/m}^3 \tag{2.1}$$

2.2 Electrical Properties

Most of the current interest in graphene is in understanding and utilizing its unusual electrical properties. The simplest property of an electronic system is the (2D) electrical conductivity $G_\square$, which is a measure of how easily charge carriers can move in the system. Of course, the conductivity is the inverse of the resistivity $G_\square = \frac{1}{R_\square}$. The electrical conductivity depends on two material parameters.

$$G_\square = \mu(ne) \tag{2.2}$$

n is the (2D) charge carrier density, μ is the mobility and $e = 1.602x10^{-19}$ is the electron charge. The carrier density is a measure of how many charges are

available to move, and the mobility is a measure of how easily each charge carrier can move in a system.

The carrier density n depends on the band structure of the material and the Fermi Energy of the system. As an example, in semiconductors, where the band structure has a gap, the carrier density goes to zero when the Fermi level is in the band gap of the semiconductor and is non-zero when it is in the conduction or valence bands. This means that semiconductors are insulating when the Fermi level is in the bandgap, and conducting when the Fermi level is in the conduction or valence bands. This phenomena is the basis for Field Effect Transistors (FETs), which are the basic building block of modern electronics.

The two-dimensional band structure of graphene, shown in Figure 2.2a, is what is known as a gapless semiconductor. This band structure rises from the π orbitals and whether the dangling p_z orbitals of neighboring carbon atoms are in a symmetric or anti-symmetric state. In the interest of time and brevity, we will not derive the band structure in this thesis. If a reader is interested in learning more, there are many excellent reviews about graphene and nanotube electronic properties[32, 16, 33].

The conduction and valence bands of graphene meet at 6 points in k-space known as the Dirac points. Near the Dirac points, the band structure disperses linearly as cones with a slope $E = \hbar v_F |\vec{k}|$ where $v_F \approx 10^6$ m/s is the Fermi velocity of graphene. This linear dispersion is unusual in materials and is most similar to the energy dispersion of massless photons as described by special relativity. Because of this relation, many physicists refer to electrons in graphene as massless or relativistic fermions.

At the Dirac point, the density of states goes to zero and the conductivity should go to zero as well. However, at these low densities, the electrons start ex-

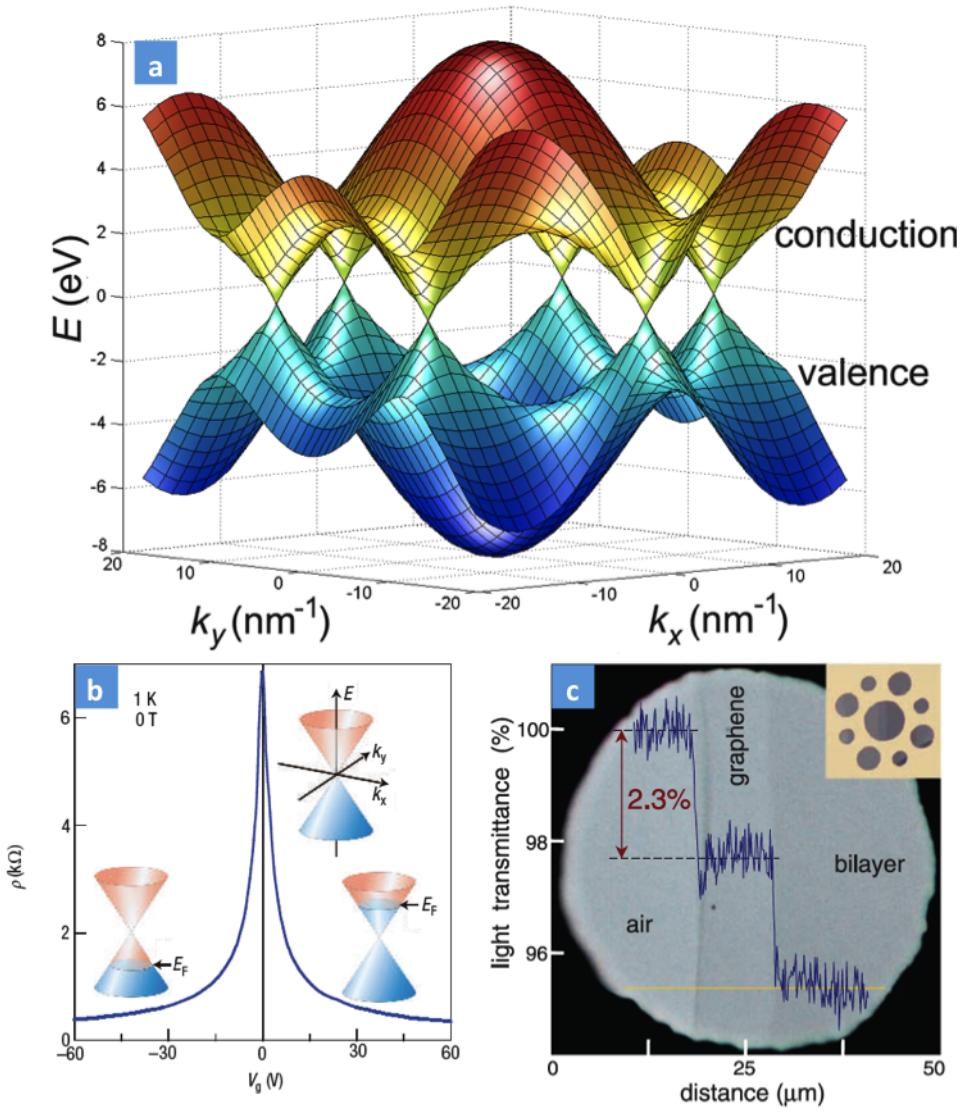

Figure 2.2: a) Electrical band structure of single layer graphene. b) Gate dependent transport of exfoliated graphene c) Optical transmission of white light through on and two layers of suspended graphene. Each layer of graphene absorbes 2.3% of the light[11].

periencing long-range, many-body interactions not captured by the tight-binding model[26, 27], and the conductivity of graphene saturates at the conductance quantum.

$$G_{\square min} = \frac{4e^2}{h} = \frac{1}{6.5k\Omega} \tag{2.3}$$

Note that this value is for the conductivity, rather than the conductance, as it is in most 1D conducting systems. Away from the Dirac point, the carrier density in graphene changes linearly with energy, so the conductance should increase linearly. In the top cone, electrons are the charge carriers. In the bottom cone, holes are the charge carriers. The cones are symmetric so, unless magnetic fields are applied to the sample, the electron and hole behavior is the same.

Figure 2.2b shows the resistivity ($R_\square = 1/G_\square$) of an exfoliated graphene device wired up with an external back-gate. We use the external back-gate to adjust the Fermi level of the graphene, and thus the conductivity. We see that the graphene resistivity peaks at 6.5 kΩ a certain gate bias, which corresponds with the Dirac point. Away from the Dirac point, the graphene resistivity drops as V_g^{-1} with gate bias in both directions (or the conductivity increases linearly with the gate bias), as expected given the linear dispersion in the band structure of graphene. The slope of this curve is related to the mobility of the graphene.

The mobility μ is a measure of the scattering rate of charge carriers in the material. The room temperature mobilities reported for exfoliated graphene on oxide range from (1,000 - 20,000 cm^2/V·s)[10]. Examples of scatterers that can limit the mobility include adsorbed or absorbed impurities on the crystal lattice, inhomogeneous charge doping from the substrate, strain or bending deformations of the lattice, phonon coupling due to temperature, or inhomogeneous charge distributions. Indeed, research groups have found that by suspending the graphene or

using a different substrate[34, 35, 36], they were able to raise mobilities up to $\sim 10^5$ $cm^2/V?s$ at room temperature. These numbers can be compared with the highest room temperature mobilities in bulk semiconductors of 77,000 $cm^2/V?s$ for InSb. While the exact limiting factors for graphene mobility are not understood[37], it is clear that electrically graphene is already competitive with semiconductor technology and is still improving.

We will discuss transport measurements and how to extract the mobility for our devices more in Section 3.4.2.

2.2.1 Optical Properties

The unusual band structure of graphene also affects how it interacts with light. The optical absorption A of graphene follows a surprisingly simple relation.

$$A = \pi\alpha = 2.3\% \tag{2.4}$$

where $\alpha = 1/137$ is the fine structure constant. Figure 2.2c shows an optical image of suspended single and bi-layer graphene on a TEM grid, with white light shining through it. By measuring the intensity of the light, we see that each layer absorbs 2.3% of light.

This strong interaction with light of even a single layer of atoms is what makes graphene visible on a silicon chip, and also allows us to perform optomechanical resonance measurements.

2.3 Mechanical Properties

Graphene's mechanical properties are as impressive as its electrical properties. The static mechanical properties of an isotropic 2D membrane are described by four

parameters: The in plane Young's modulus Yt, the Poisson ratio ν, the breaking stress σ_{int} and strain ϵ_{int}, and the bending rigidity B. These parameters dictate how a graphene membrane will respond to strain and deflections and determine what the frequency of NEMS built out of graphene will be.

2.3.1 In-plane mechanical properties

The definitions of Young's modulus and poisson ratio come from continuum mechanics. The Young's modulus is defined as the relation between the linear restoring force σ_x in a membrane due to a linear (uniaxial) strain ϵ_x on the membrane.

$$\sigma_x = -Y\epsilon_x \tag{2.5}$$

The Poisson ratio is a measure of how much a membrane contracts along a direction perpendicular to an applied (uniaxial) strain.

$$\epsilon_y = -\nu\epsilon_x \tag{2.6}$$

The breaking stress/strain is the point at which the graphene membrane breaks due to in-plane stress.

The Young's modulus of graphene has been known for many years from measurements of the mechanical properties of graphite[38] and Carbon nanotubes[39, 40]. The equivalent measurements on graphene have confirmed what was expected.

Experiments using AFM tips[41, 12, 42] and gas pressure[5] to stretch single and multilayer graphene membranes, as shown schematically in Figure 2.3b showed that the Young's modulus of graphene is $Yt = 340$ N/m. These experiments also showed that graphene is under an initial tension before it is strained further by the AFM tip. These experiments measured the pretension to be $S_0 = 0.07 - 0.74$ N/m which is equivalent to a pre-strain of $s = 10^{-5} - 10^{-4}$. Figure 2.3c, shows

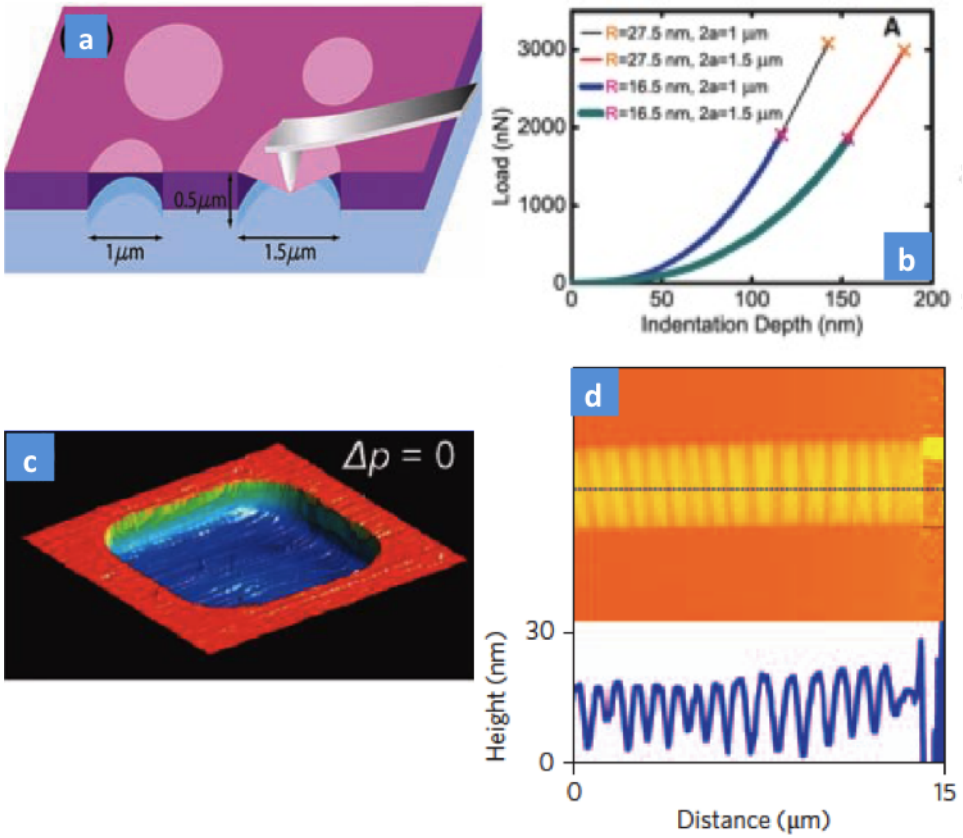

Figure 2.3: a) Diagram of pushing on a graphene membrane with an AFM cantilever[12]. b) A force-indentation curve of an AFM cantilever pushing on graphene[12]. c) AFM image of graphene suspended over a hole shows that graphene self-adheres down along the side wall[5]. d) AFM image of graphene suspended across a trench shows the graphene is rippled[13].

an AFM of unstrained graphene over a hole. The graphene self-adheres down the sidewalls of the hole. This self-adhesion is most likely due to a van der Waal's attraction between the oxide substrate and the graphene. The magnitude of the van der Waal's attraction is the same as the pretension $S_0 \sim 0.1$ J/m^2.

By pushing on the graphene with a diamond AFM tip[12], researchers were able to tear the graphene directly under the AFM tip. They found that the breaking stess is $\sigma_{int}^{2D} = 42$ N/m corresponding with a strain of $\epsilon = 0.25$ or 25%. These measurements tell us that graphene is the strongest material on earth.

The Poisson ratio has not been independently measured in graphene. In this thesis, it is defined to be the in-plane Poisson ratio of graphite $\nu = 0.17$.

2.3.2 Out of plane mechanical properties

The bending rigidity is defined as the amount of energy per unit area needed to curve an object.

$$\frac{E_{bend}}{A} = \frac{B}{2}\frac{1}{R^2} \tag{2.7}$$

In this equation, R is a radius of curvature. In continuum mechanics, this value is normally derived in terms of the Young's modulus by assuming that a curved membrane is a sum of stretching along the top surface and compression along the bottom surface. However, as we discussed in Section 2.1.1, graphene does not have a top and bottom surface, which means that this relation breaks down. Instead, the bending modulus is an intrinsic property of the material due to the interaction of π and σ bonds when bending graphene and will be much less than the value derived from continuum mechanics. According to molecular dynamics simulations, the bending rigidity of graphene is estimated to be $B \approx 1\ eV$[43].

The bending modulus of graphene is more difficult to measure than the stretch-

ing modulus and has not been independently measured to date. There are two reasons for this. First, the intrinsic bending modulus is small, so it will not dominate the mechanical properties of a system. Second, if the graphene membrane has ANY structure (multilayer, ripples, buckling, etc). This will immediately impose an extrinsic bending modulus to the structure. We can intuitively see this by imagining holding a sheet of paper in one hand. If we hold the paper out flat, then it will flop over from gravity. However, if we impose a small amount of curvature to the paper, then it will stay rigid.

The closest measurement of the bending modulus of graphene to date was an experiment studying the rippling of graphene under uniaxial tension[13], shown in Figure 2.3c. This rippling comes from the nonlinear coupling of the bending modulus to the strain in a membrane through the poisson ratio[44]. However, these measurements did not give an actual value for the bending modulus as the imposed strain was not known (and, in fact the used the continuum mechanics version of the bending modulus to extract the strain in the membrane). Future experiments where a known strain is induced on graphene while measuring the rippling will likely allow a direct measurement of the bending modulus.

2.4 Summary

Graphene has excellent electrical, optical, and mechanical properties, which we summarize in Table 2.4. In the next chapter, we will see how to use graphene to fabricate atomically thin membranes.

Table 2.4: Properties of pristine graphene		
C-C bond length	d	1.42 Å
Graphite interlayer distance	t_{eff}	3.42 Å
Density	ρ	7.4×10^{-7} kg/m^2
Fermi Velocity	v_F	10^6 m/s
Maximum resistivity	$R_\square$	6.5 kΩ
Minimum conductivity	$G_\square = 1/R_\square$	152 μS
Typical mobility	μ	1000 - 20,000 cm^2/Vs
Suspended mobility[34]	μ	10^5 cm^2/Vs
Optical absorbance (per layer)	A	2.29 %
Optical transmission (per layer)	T	97.7 %
Optical reflection (per layer)	R	0.0128 %
Youngs modulus	Yt	342 ± 30 N/m
Third order elastic modulus	D	-690 ± 120 N/m
Poisson ratio	ν	0.17
Pretension	S_0	0.07-0.74 N/m
Prestrain	s	$10^{-5} - 10^{-4}$
Adsorbed mass ratio	α	$1 - 10$
vdW adhesion energy	$U \sim S_0$	~ 0.1 J/m^2
Breaking stress	σ_{max}	42 ± 4 N/m
Breaking strain	ϵ_{max}	0.25
Intrinsic bending modulus	B_0	~ 1 eV

Chapter 3

Fabrication of suspended graphene membranes

The aim of this chapter is to describe the necessary techniques for a new researcher to start growing graphene and fabricating novel devices based on suspended graphene membranes. Over the course of our work for this thesis, these techniques have evolved from the humble beginnings of rubbing graphite on oxide surfaces to sophisticated methods of producing large arrays of tensioned single-layer membranes on arbitrary substrates.

We will start by describing the original methods for producing suspended membranes via mechanical exfoliation. We will then describe new techniques for growing graphene using Chemical Vapor Deposition (CVD) and for transferring the graphene onto arbitrary substrates. Next, we will describe how to use these techniques to produce a wide variety of novel graphene-based devices. Finally, we will give an overview of several standard techniques we use to characterize the number of layers and quality of the graphene films. The level of detail of these sections is aimed at individuals familiar with standard nanofabrication techniques but not necessarily graphene fabrication and measurement techniques.

3.1 Graphene from mechanical exfoliation

The reason for the popularity of graphene in the physics community over the last few years lies not just in its interesting optical, thermal, mechanical and electrical properties, but in how obscenely simple it is to make. Anyone with a chunk of graphite, a roll of Scotch tape, and a silicon wafer can start doing original

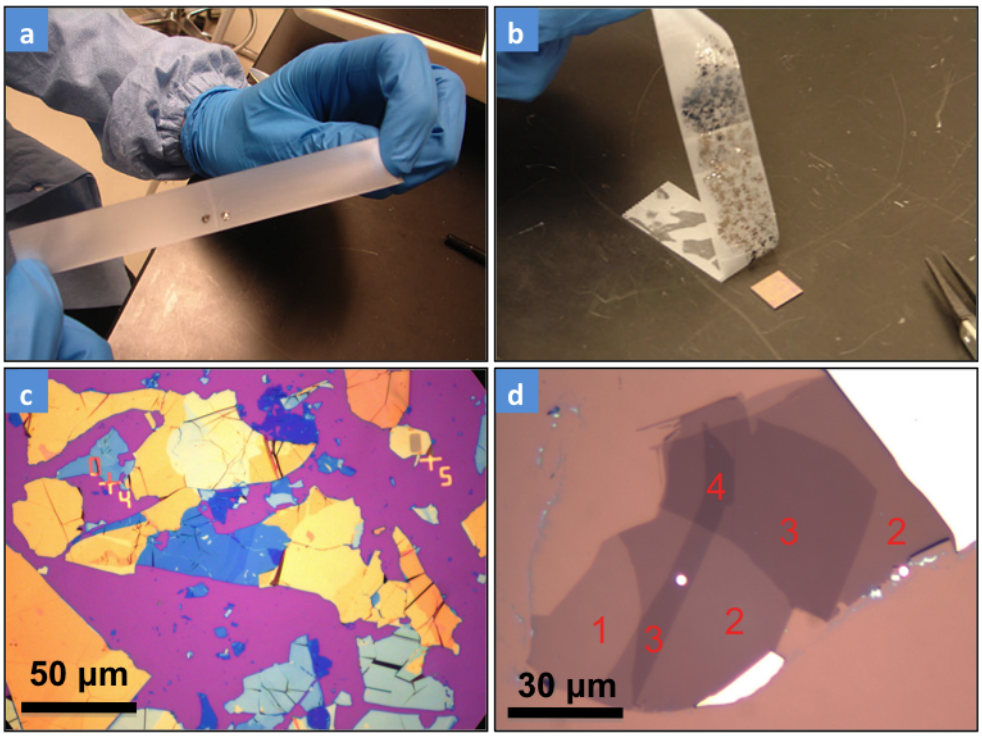

Figure 3.1: a) Kish graphite flake cleaved by Scotch tape. b) Tape covered with graphite pressed down on silicon chip with 285 nm oxide[14]. c) Typical optical image of oxide surface after transfer. Pink is the oxide, Blue are thin flakes (20 nm) of graphite, Gold is thick graphite. d) Optical image of a very nice graphene flake on oxide. One, two, three and more layers are clearly identifiable.

experiments in a few days. In the same way that a pencil can be used to draw on paper, very thin graphite flakes can be exfoliated off of bulk graphite onto a substrate.

Figures 3.1(a-b) shows the Scotch tape technique for making graphene, developed by the Geim group[24, 25, 26]. Starting with a chunk of Kish graphite, we put the graphite on a piece of tape and repeatedly cleave the graphite by opening and closing the tape until the graphite fully covers the tape. The tape is then pressed onto a 285 nm thick silicon oxide layer on a silicon wafer. We use a blunt object like a pencil eraser or curved metal surface to rub on the back of the tape for a couple

of minutes until the tape and graphite are well adhered to the surface. We then slowly remove the tape at a shallow angle from the surface. After removing the tape, we optically examine the surface. Most of the surface resembles Figure 3.1c, with different thicknesses of graphite showing up as different colors ranging from dark pink to gold on the pink substrate. If we are lucky, we end up with a few very thin flakes like those shown in Figure 3.1d, where we see a piece graphene which is one, two, and more layers thick. The key element that allows this technique to work is the 285 nm oxide thickness[45]. Due to thin film interference, having the right thickness of oxide allows us to see even a single layer of graphene and count the number of layers.

3.1.1 Fabricating devices from mechanically exfoliated graphene

Mechanically exfoliated graphene is very high quality and the process for getting it is very simple. However, the mechanical exfoliation process has several downsides. First, it is very time intensive. It can take a day to get even a single flake to use in experiments. Second, there is no control over where the graphene sheet gets deposited, or what size and shape it will be. Third, there are many other flakes of graphite of various thicknesses all over the surface that are deposited at the same time.

These limitations are not a problem if we want to perform very simple fabrication experiments. For example, we can use a custom mask and alignment to place features on top of the deposited flake wherever it ends up as first shown by the Geim group[24, 17]. We can also use a procedure developed by our group, in which we deposit graphene onto a surface which is so dense with features. The result is that the graphene automatically ends up on top of these features[46, 12]. Alternatively, we can use an aligned transfer process to move the graphene flake to a new

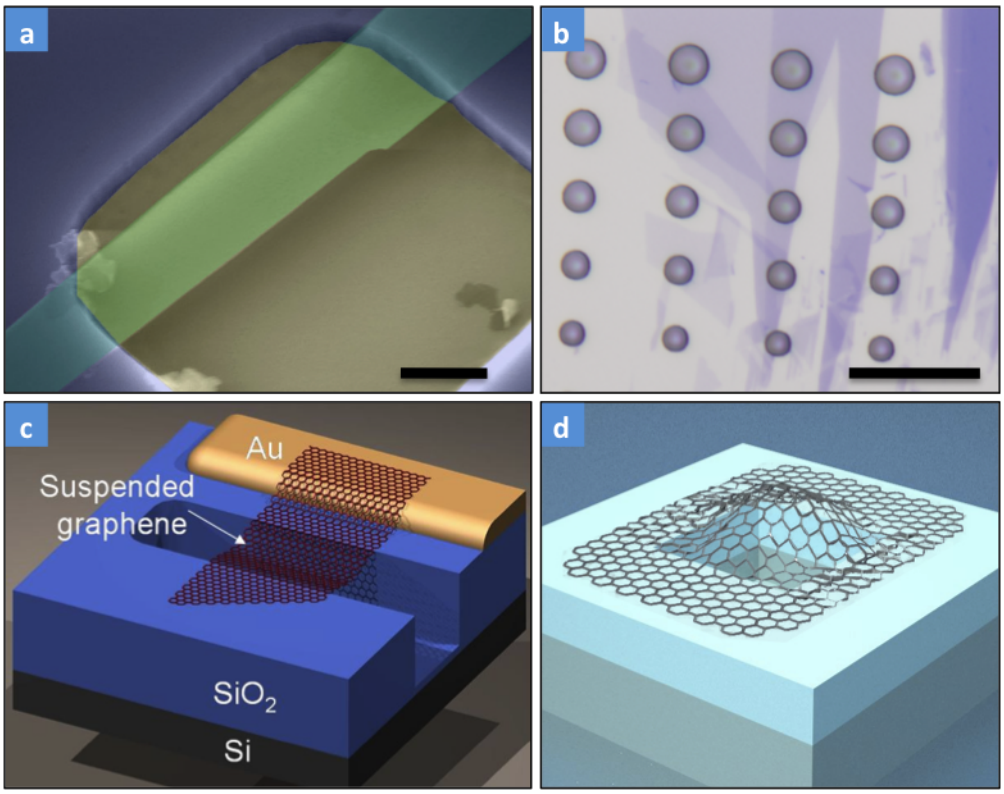

Figure 3.2: a) False colored SEM of few-layer graphene suspended over a trench. b) Optical image of single and few-layer graphene covering circular holes in silicon oxide. c) Schematic of electrically-contacted graphene suspended over a trench. c) Schematic of graphene sealing a hole in oxide.

substrate once we have identified it, as developed by the Columbia group[47, 36]. Figure 3.2 shows some early devices made by our group using the dense feature method.

3.2 Chemical Vapor Deposition grown graphene

Making one graphene device at a time is fine for simple experiments. However, for most applications, and for more elaborate experiments, large arrays of identical graphene devices are required with control over the size, shape, and location of

each piece. For this to work, a better technique for producing graphene is needed. Over the years, several techniques have been proposed and tested[48, 49, 50, 51]. However, the one that holds the most promise is using Chemical Vapor Deposition (CVD) to grow graphene on a metal substrate and then transferring it onto any arbitrary surface.

The idea of growing graphene on a substrate is not a new one. Research labs have been doing it for decades. The two most notable examples are groups using low pressure CVD to grow high-quality single-layer graphene on single crystal ruthenium and iridium[22] substrates, and groups using thermal decomposition of silicon carbide substrates to grow few-layer graphene[21]. These techniques enable the growth of large-area graphene of one or more layers on substrates. However, up until recently, a big challenge was that the grown graphene was sitting on expensive conducting substrates (A 4" silicon carbide wafer costs $2000), and currently, there is no simple way to remove it.

More recently, several groups have found that it is possible to grow few layer graphene on nickel[28, 19], and single-layer graphene on copper[6] using CVD. These metals are cheap, standard materials used in nanofabrication, and the graphene can be transferred off the metal onto an arbitrary substrate.

3.2.1 Furnace setup

Chemical vapor deposition, uses a setup like that shown in Figure 3.3a to flow carbon-filled gas such as methane (CH_4) at high temperature and low pressure over a substrate. The carbon decomposes from the hydrogen and bonds to the substrate. We also include argon and hydrogen to dilute the methane and to change the chemistry of the reaction.

For the CVD proces, we use the adapted CVD furnace shown in Figure 3.3b

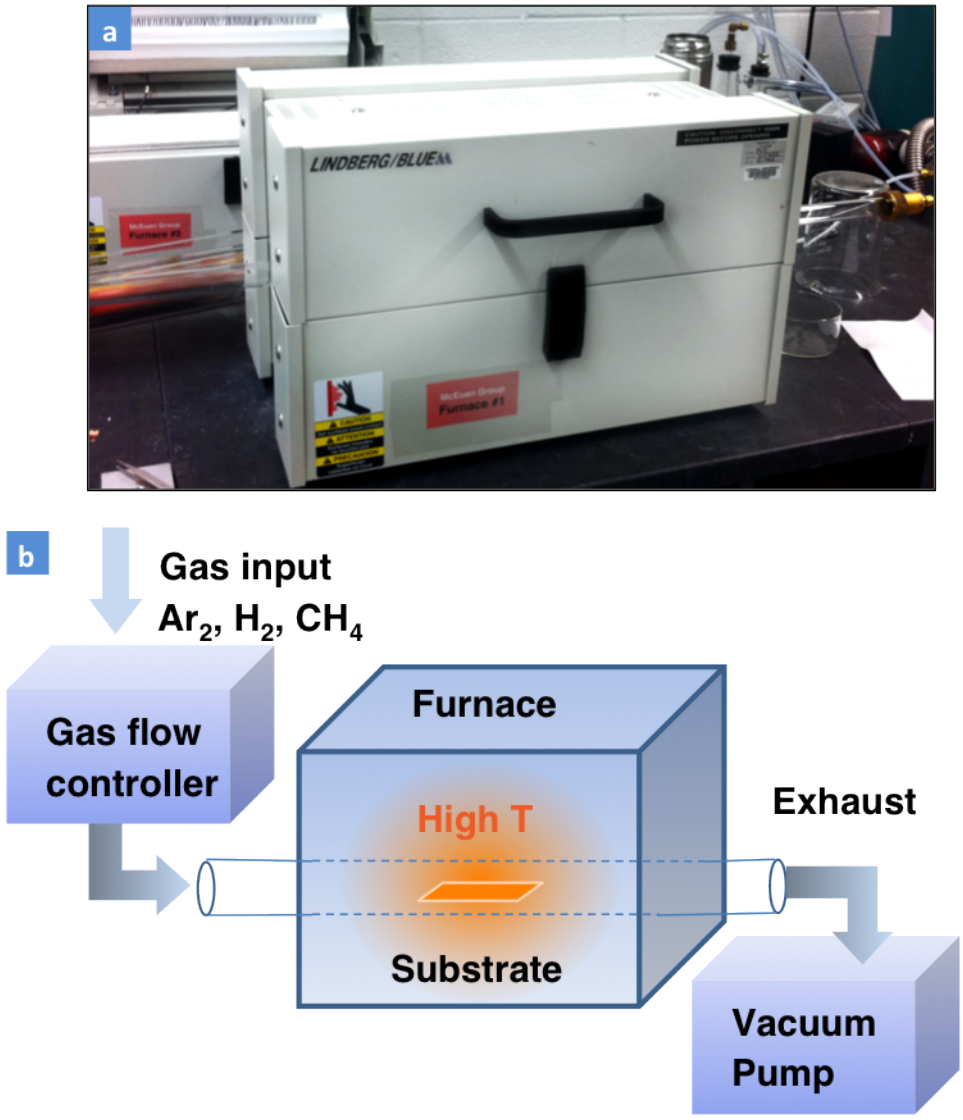

Figure 3.3: a) Picture of CVD furnace used to grow graphene. b) Schematic of CVD graphene growth system

to grow graphene. We use a 1 inch diameter tube in a Lindberg temperature-controlled furnace. We use an MKS flow controller to flow ultra-high purity (UHP) argon, hydrogen and methane through the tube. We achieve low pressure by attaching an oil pump with a cold trap to the gas flow exhaust. The gas flow attachments are tightly clamped to prevent atmospheric contamination. Gas pressure should be < 10 mTorr with no gas flowing and ~ 1 Torr with gas flowing.

3.2.2 Chemical Vapor Deposition Procedure

Following the recipe of Li et al[6], we use Alfa Aesar 0.025 mm, 99.8% pure copper foils shown in Figure 3.4 as the starting substrate for growth. This foil is polycrystalline with grain sizes of $\sim 100\ \mu m$. We will further discuss the relevance of grain size in Chapter 4. The copper substrate does not have to be this foil. Other groups have shown that it is possible to use evaporated copper on a substrate (700 nm thick), single crystal copper, or even a copper penny[52, 53, 54, 55], with similar results.

We prepare the foils for growth as shown in Figure 3.4 by cutting out a 1.5 cm square, notching the edge to indicate orientation for later. We press the foil between glass slides to flatten out any kinks or wrinkles. During the entire growth and transfer process, care must be taken to keep the copper foils as flat as possible. Crumpled foils lead to cracked graphene membranes and poor transfers. We also find that contamination on the copper surface leads to poorer quality graphene growth. In order to clean the surface and de-oxidize the copper that has been sitting out for several months in air, we treat the foil with the following order of solvent dips: acetone (10 Sec), water, acetic acid (10 Minutes), water, acetone (10 Sec), isopropanol (10 Sec). Finally, we gently dry the foil using a low flow nitrogen gun. It is not clear that this cleaning procedure is necessary if one instead anneals

Figure 3.4: Copper foil used to grow graphene on left and a copper penny on right. Pennies minted before 1981 are 100% copper, after that, they are doped with zinc. Credit Melina Blees

the copper for more time before growth.

For the growth, we follow a procedure similar to that used by Li et al[6]. We load 3-5 copper foils into the CVD furnace and pump the system down to a base pressure under 10 mTorr. After the base pressure is achieved, we flow 6 sccm of hydrogen, which raises the base pressure to about 120 millitorr, and heat the furnace to 1000° C. We anneal the sample at 1000° C in the hydrogen for 10 minutes, then do the graphene growth by flowing 157 sccm of methane for 13 minutes. During this time, the base pressure should rise to about 5.5 Torr. After 13 minutes, we let the system cool slowly back down to room temperature for over 1 hour. Once the system is cooled below 150° C, we re-pressurize the tube by replacing the methane and hydrogen with 200 sccm of argon and turning off the vacuum pump.

The graphene growth mechanism on copper is self-suppressing. We have not found that running the growth for longer time results in higher disorder or multi-layer graphene. We and other groups[56] have found that by running very short

($< 10\ s$) or very low pressure growths results in partially grown graphene islands. Other groups have found that by doing growths in ambient pressures and by doing very slow cool downs, they were able to get multilayer[57] and bilayer[58] graphene. We will further discuss the graphene growth mechanism in Chapter 4.

3.2.3 Transferring graphene to arbitrary substrates

In order to transfer the grown graphene off the copper and onto an arbitrary substrate, we use a procedure similar to that developed by several groups[28, 19, 6]. The basic idea is visualized in Figure 3.5. First, we deposit a thin polymer film onto the copper foil after we have grown the graphene, then we etch the foil away in acid, leaving a thin polymer film with graphene on it. We then deposit this film onto an arbitrary substrate and remove the polymer, leaving the graphene on the substrate. Figure 3.5e shows the transferred graphene on 285 nm silicon oxide.

The exact procedure is more complicated. In the rest of this section, I will explain the basic process that works for us that is similar to that used by other groups[6, 28, 19]. Then I will describe some more advanced variations which we have developed, which have allowed us to make more complicated devices.

We make a 500 nm thick polymer film by dripping 8% poly(methyl methacrylate) (PMMA) diluted in anisole onto one side of the foil and spinning itat 4000 rpm for 60 seconds. Baking the PMMA is not necessary. We etch the copper foil away by putting the foil into 1 M ferric chloride (We use Transene CE-200). It is not necessary to remove the graphene on the other side of the foil. The easiest way to do the etch is to carefully float the copper foil with PMMA side up on the surface of the etchant similar to the way that you float a paper clip on water. The PMMA is hydrophobic, so it will float facing up both before and after the copper is etched. After about 1 hour, the copper will be fully etched, leaving the PMMA

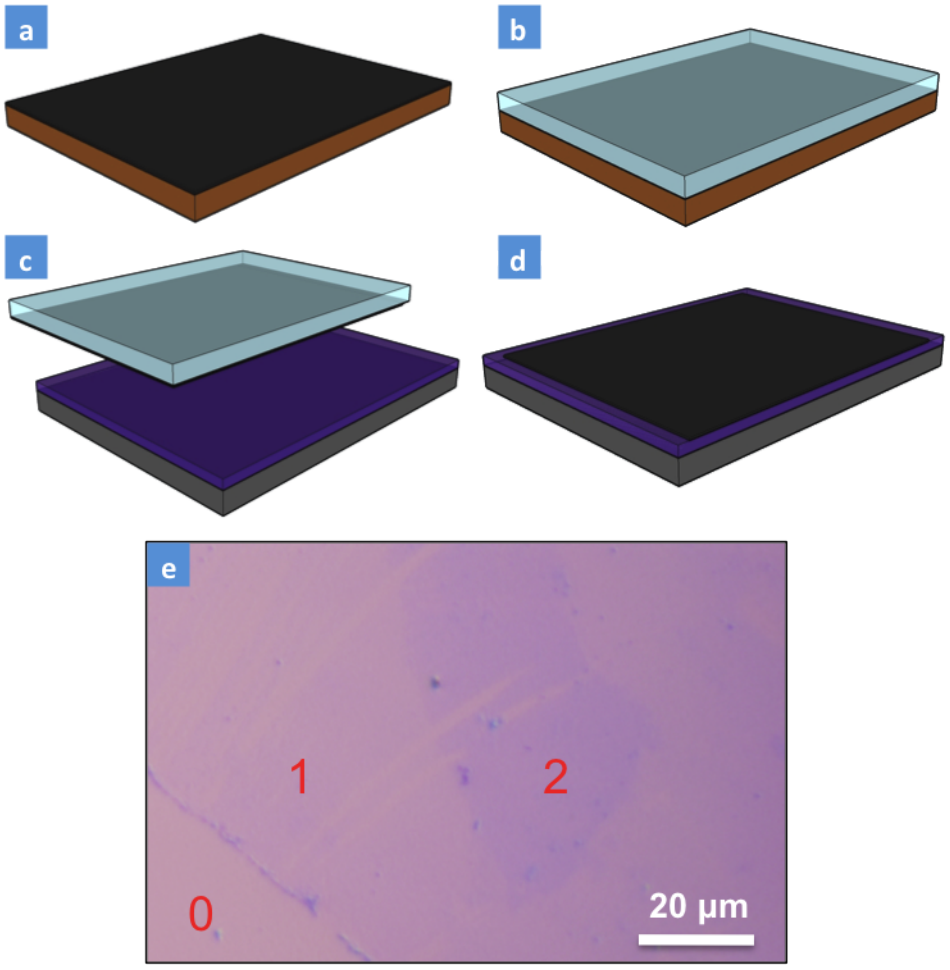

Figure 3.5: a-d) Process flow for graphene transfer on to oxide. a) Graphene on copper foil. b) Spin PMMA film on to copper foil. c) Etch foil away and transfer PMMA film to oxide surface. d) Dissolve PMMA film. e) Optical image of CVD graphene on 285 nm oxide after transfer. Regions with no graphene, one layer, and two layers are marked. Tears are visible in the graphene due to poor transfer.

film floating on the surface with the PMMA side up and the graphene side on the bottom.

We get the PMMA film out of the etchant by scooping it up and transferring it into clean de-ionized (DI) water using a silicon piece slightly larger than the PMMA film. We repeat this until the PMMA film is floating in completely clean water($\sim$ 6 times). We leave the membrane in each DI water bath for $\sim$ 1 minute, and there should be no visible yellowing of the final bath due to the copper etchant, or else the final graphene will be covered in iron oxide. Next we take the desired final substrate and scoop the PMMA-graphene film out of the water. Again, due to the hydrophobicity of the PMMA, the graphene side will always be down, so there is no danger of getting the wrong side.

We let the PMMA dry onto the substrate for at least 8 hours, so all the water has time to wick out from between the film and the substrate. In order to remove the PMMA film, we soak the chip in Dichloromethane for $\sim$ 4 hours and rinse the chip in Acetone and IPA.

This transfer process gives us arbitrarily large substrates with un-patterned single-layer graphene on the surface. The only limitation is how much copper foil you can fit inside your furnace. In fact, groups are using a similar method with rollers to produce graphene on the meter scale[2].

3.2.4 Cleaning Graphene

One of the most difficult tasks is getting graphene to be clean and keeping it clean. Contamination is a huge problem because it keeps the graphene from being flat; gets in the way of good contact resistance; provides a barrier for imaging with electrons or photons; and keeps our wonderful two-dimensional system from being all it can be. In Section 3.4, we discuss in detail how to look at graphene

and determine its cleanliness, but for now I want to discuss how we deal with contamination.

The two simplest ways of cleaning graphene are by using solvents and by annealing. Solvents work well at getting rid of large amounts of contamination, but never leave the graphene completely clean. Annealing works well at getting rid of small amounts of contamination but is not aggressive enough to get rid of large amounts of material and can chemically modify photoresist so that it is not removable. The two techniques together get graphene clean enough for most of our experiments.

For solvent cleaning, we typically soak a sample in dichloromethane or acetone for several hours, then rinse in isopropanol. For anneals, we either anneal in argon/hydrogen 800/200 sccm gas flow at 400 C for 2 hours[59], or in air at 350 C for 2 hours.

In the next section, I will point out when we perform anneals and solvent baths as part of the fabrication procedure. These are used to improve contact resistance or remove extraneous material.

3.3 Fabricating graphene devices: Theme and variation

The next few sections demonstrate the wide variety of graphene devices that we can make using variations on the process outlined above. These include electrically contacted graphene; large arrays of doubly-clamped and fully clamped graphene membranes both near to a substrate and freely suspended; and atomically clean suspended graphene. We will describe the processes that we use to fabricate the above devices and highlight the key innovations that made them possible.

3.3.1 Topgated, electrically contacted graphene

First, we will describe the process similar to that used by several groups for doing purely electrical measurements. We make electrically-contacted, top-gated graphene in a four-probe measurement geometry using the process flow visualized in Figure 3.6a-d. We transfer un-patterned CVD graphene onto a degenerately doped silicon wafer coated with 285 nm of silicon oxide. We then pattern the deposited graphene into an array of rectangles using lithography and a 10 second oxygen plasma etch. We clean the remaining photoresist off by soaking the sample in acetone for 4 hours, then annealing the sample in argon/hydrogen 0.8/0.2 SLM gas at 400 C flow for 2 hours. We mkde electrodes to contact the graphene by using lithography to define the shapes then evaporating 1.5 nm/45 nm thick titanium/gold on top of the patterned graphene. To make the top-gate, we used lithography to define the shape, then used e-beam evaporation to deposit 90 nm of silicon oxide as the gate dielectric and 1.5/45 nm of chrome/gold as the gate electrode. We do not break evaporator vacuum between depositing the oxide and electrode. Figure 3.6a-d shows an optical image and schematic cross section of the resulting devices.

3.3.2 Suspended, electrically contacted graphene

For electrically-contacted suspended graphene membranes, we used the process flow visualized in Figure 3.7. We transferr un-patterned CVD graphene onto a degenerately doped silicon wafer coated with 285 nm of silicon oxide. We then pattern the deposited graphene into an array of rectangles using lithography and a 10 second oxygen plasma. We clean the remaining photoresist off by soaking the sample in acetone for 4 hours, then annealing the sample in argon/hydrogen 0.8/0.2 SLM gas at 400 C flow for 2 hours. We deposite 2 nm/150 nm thick titanium/gold

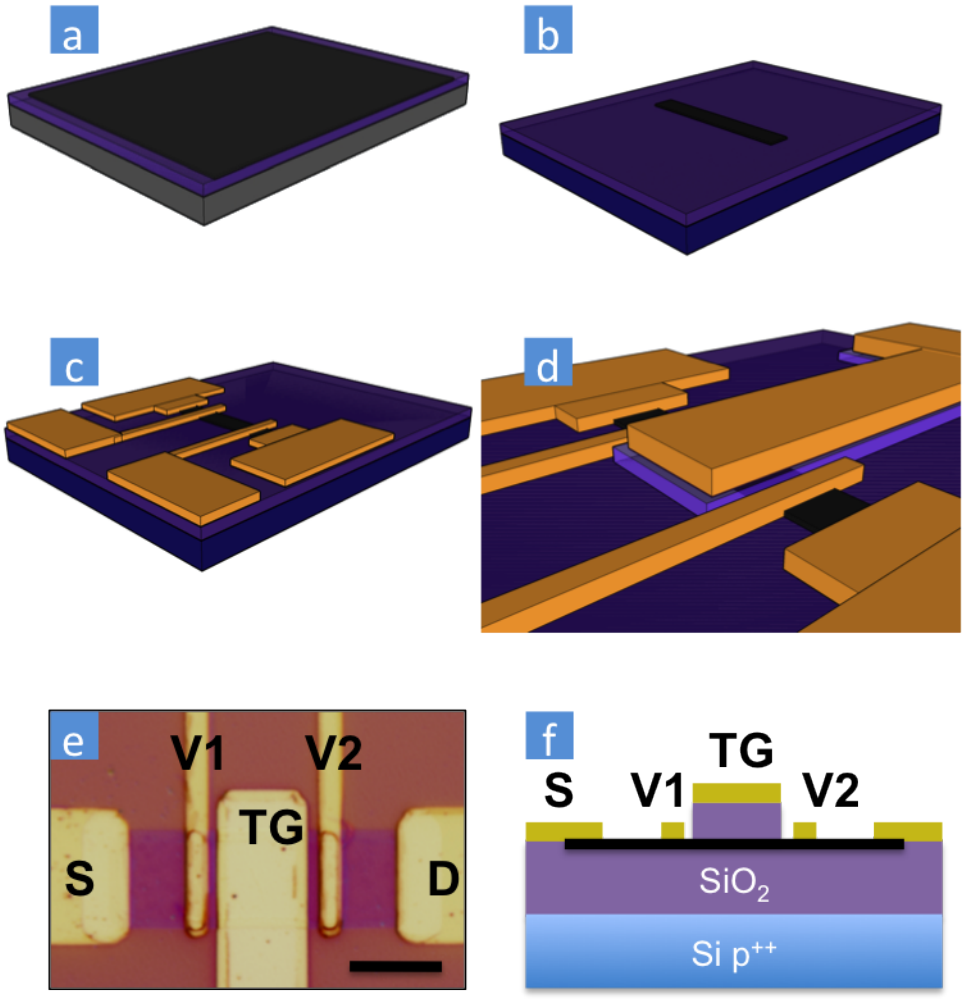

Figure 3.6: a-c) Process flow for fabricating electrically contacted top-gated graphene devices. a) Starting with un-patterned graphene transferred onto 285 nm thermally grown silicon oxide b) Pattern graphene into rectangles using photolithography and oxygen plasma. c) Deposit electrodes in four point geometry on top of graphene using lithography. d) Pattern a gate on top of the graphene using lithography. The gate is made using e-beam evaporation of 90 nm of silicon oxide, and 1.5/45 nm of Chrome/Gold, without breaking vacuum. e) Optical image of one top-gated device. The electrodes are labeled according to their function. Scale Bar is 10 μm. f) Schematic of top-gated device in profile. Thicknesses shown are not to scale.

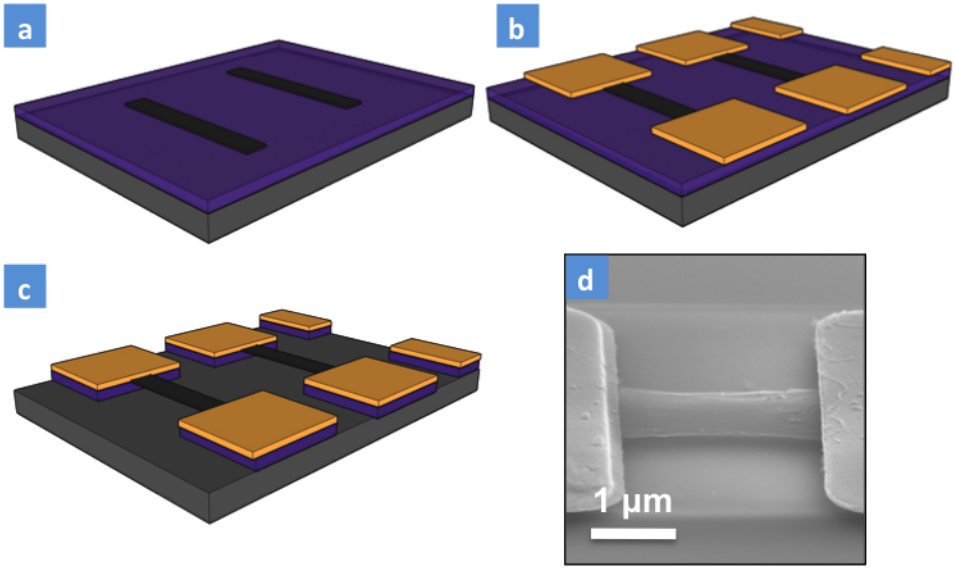

Figure 3.7: a-c) Process flow for fabricating electrically-contacted, suspended graphene. Starting with unpatterned graphene on oxide as seen in Figure 3.5e. a) Pattern graphene into rectangles using photolithography. b) Deposit electrodes on top of graphene using lithography. c) Etch away oxide using buffered oxide etch, and critical-point dry to produce an array of electrically-contacted, suspended graphene membranes. d) Angled SEM of one electrically contacted device. Length 2μm, Width 1μm

electrodes on top of the patterned graphene. Finally, we use buffered hydrofluoric acid etch (BOE 6:1) to completely remove the oxide under the graphene[34, 60], and critical-point dry the chip. Figure 3.7d shows the resulting devices: Doubly-clamped membranes that are electrically contacted and with a silicon back-gate. This process is similar to that used to make electrically contacted, suspended membranes using exfoliated graphene[17, 34]. Our innovation has been to scale it up to produce hundreds of devices at a time, and to control the membrane shape.

3.3.3 Pre-patterned graphene devices

We developed a novel fabrication technique to produce large arrays of doubly clamped graphene resonators using the process flow visualized in Figure 3.8. In order to produce these arrays, we first pattern 3 μm wide graphene ribbons on the copper foil using contact lithography and a 20 second oxygen plasma etch. We then clean the photoresist off the graphene by sonicating the foil in acetone for 1 minute. We then soak the foil for 10 minutes and sonicate again for 1 minute.

Following the transfer procedure described above, we transfer the patterned graphene onto a PMMA membrane and then transfer the PMMA/graphene membrane onto the surface of a silicon wafer with 285 nm of oxide and a patterned array of trenches with length of 1-8 μm and depth of 285 nm. Finally, we dissolve the PMMA in dichloromethane and critical-point dry the chip.

Figure 3.8f shows the resulting devices: large arrays of doubly-clamped graphene membranes, with the graphene on top. The power of this technique is that it allows us to put graphene of a certain size and shape on top of prefabricated features. The patterned graphene is covering most of the surface, so it is possible to put the graphene onto much more complicated circuits. By statistics of surface coverage, the graphene will end up on top of a large fraction of the devices. For example, Figure 3.8g shows electrically-contacted graphene fabricated by using the pre-patterned graphene technique suspended over a local backgate (Credit: Jonathan Alden). Interestingly, these top deposited membranes have low contact resistance, which we demonstrate using scanned probe measurements in Section 4.5.2.

3.3.4 Fully clamped devices by liquid-free polymer removal

We developed a novel fabrication technique to produce large arrays of fully-clamped graphene membranes using the process flow visualized in Figure 3.9. We transfer

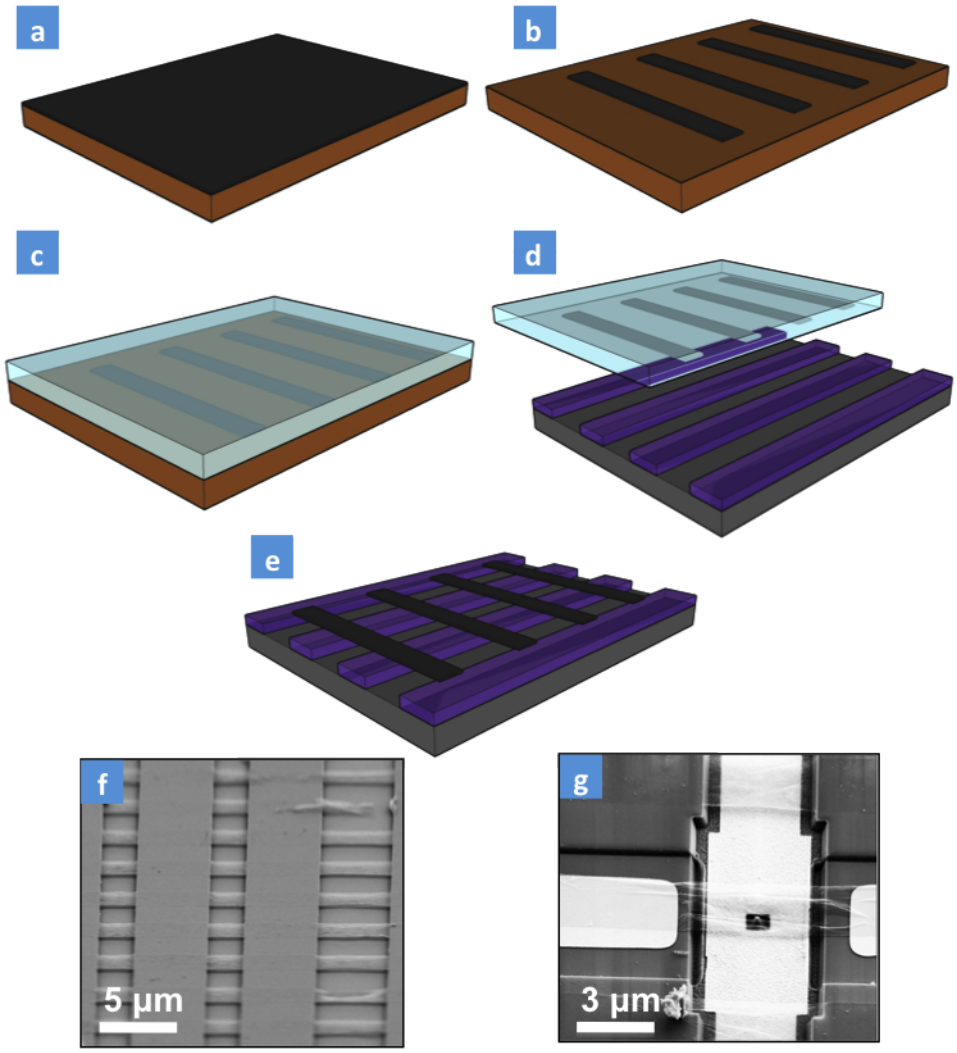

Figure 3.8: a-e) Process flow for fabricating pre-patterned suspended graphene devices. a) Graphene on copper foil grown using CVD. b) Graphene patterned on copper foil using contact lithography. c) PMMA film deposited on copper foil. d) Foil is etched, and PMMA film is transferred to pre-fabricated substrate. e) PMMA is dissolved, and the chip is critical point dried to produce arrays of doubly clamped graphene membranes. f) Angled SEM of resulting suspended graphene array. SEM shows extremely good yield. g) Angled SEM of electrically contacted suspended graphene over a local gate. Graphene is on top of electrodes. Last image credit: Jonathan Alden.

unpatterned CVD graphene using an extra thin 50 nm PMMA membrane onto a 200 nm thick suspended silicon nitride membrane patterned with square or circular holes. We found that using liquids to dissolve the PMMA membrane destroyed the freely suspended membranes. Instead, after letting the PMMA/graphene membrane dry, we anneal the chip at 350 C in air for 2 hours. The thin PMMA membrane gently bakes off the chip leaving the graphene freely suspended in a liquid-free process (Credit: Carlos Ruiz-Vargas). It is very important to use as thin a PMMA membrane as possible for a clean bake-off.

Figure 3.9e shows that we can get large arrays of fully-clamped suspended membranes with $> 90\%$ yield for smaller ($< 3\mu$m). Figure 3.9f shows that we can use the same technique to get atomically thin membranes of $< 30\mu$m in size. These fully clamped membranes are accessible from both sides and can be used for transmission microscopy, NEMS, and nanopore applications. Due to its simplicity, cleanliness, and high yield, we are now frequently using this technique in other device geometries as well.

3.3.5 Polymerless graphene deposition

The polymer membrane is not strictly necessary for the graphene transfer process. Figure 3.10 shows graphene freely floating on the surface of Ferric Chloride. We can transfer graphene onto a TEM grid using a process similar to that developed by the Zettl group[61]. We deposit a silicon nitride TEM grid on top of the copper foil and then deposit a droplet of IPA to adhere the grid to the foil. After the IPA dries, we float the whole pile on top of ferric chloride, as before. After the copper etches away, we scoop the TEM grid out with a TEM hoop, rinse it in water and IPA, and then let it air dry. Later we anneal the chip in air at 350 C for 2 hours. The result is exceptionally clean graphene but the membranes are much more

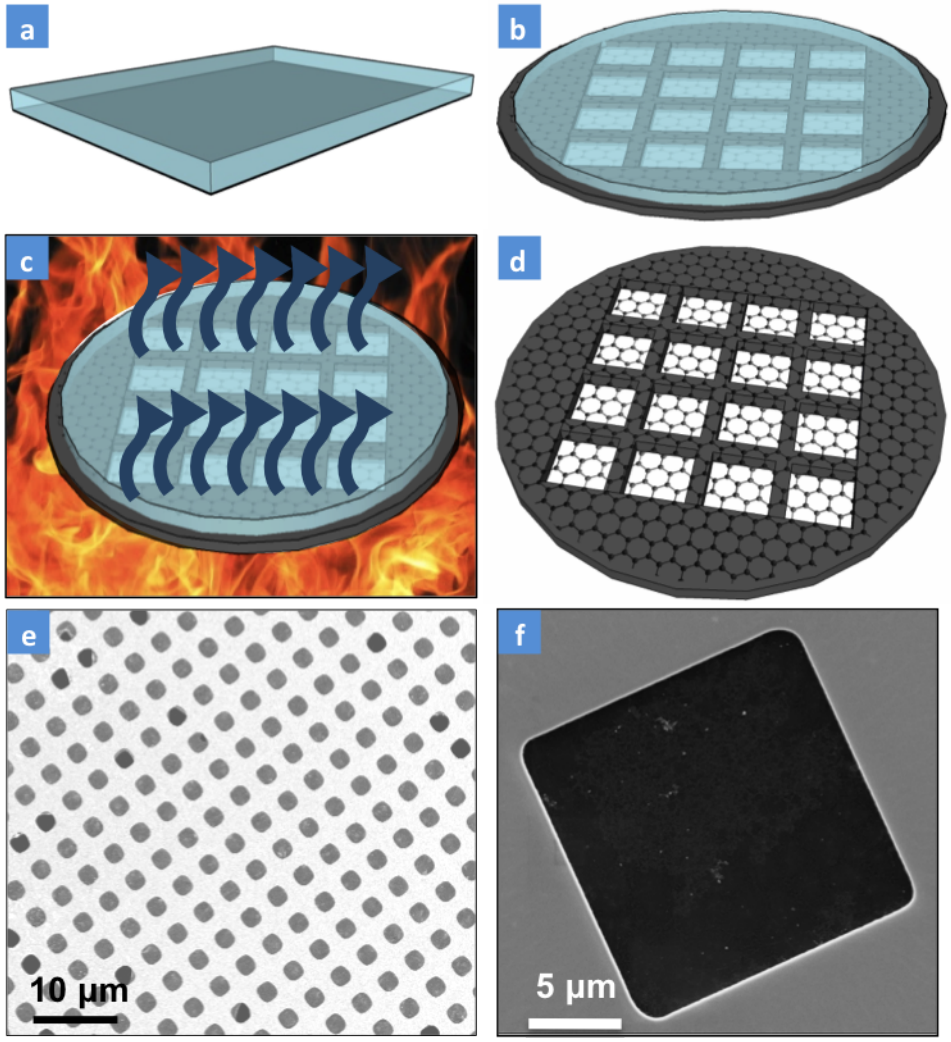

Figure 3.9: a-d) Process flow to make fully-clamped freely-suspended graphene membranes. a) PMMA with graphene b) PMMA with graphene on a silicon nitride membrane. c) Anneal the entire structure. d) Resulting membrane. e) Large high-yield array of 2.5 μm membranes produced using this method. Light spots are holes covered with graphene. Dark spots are holes where the graphene is broken. f) 30 μm membrane produced using this method. Dirt is clearly visible on the membrane surface.

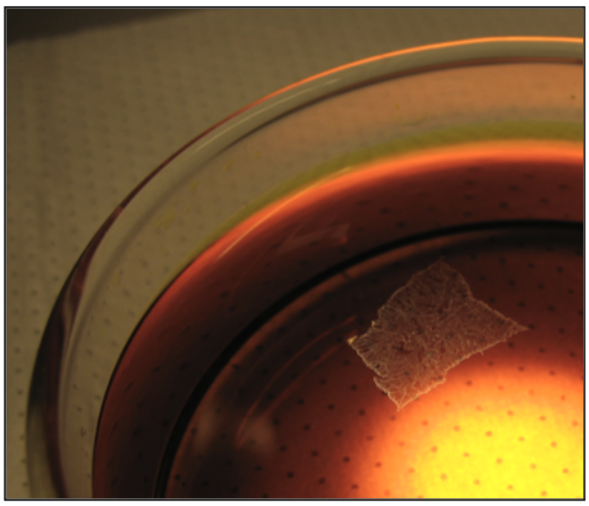

Figure 3.10: Graphene floating on the surface of 1 M ferric chloride with absolutely no polymer support. Surface tension of the liquid keeps the graphene from balling up.

wrinkled and lower-yield ($< 10\%$ for 2.5 μm suspended graphene membranes).

3.3.6 Fabrication Summary

Using all of the fabrication procedures outlined above, we are now reliably producing hundreds to hundreds of thousands of single-layer suspended graphene membranes at a time. For doubly-clamped devices, we get yields of $> 80\%$ for membranes with $L < 3\mu$m and $W < 5\mu$m. For fully-clamped devices, we get yields of $> 90\%$ for membranes up to 5 μm on a side, with lower yields for membranes up to 30 μm on a side.

The techniques developed, in particular the ideas of pre-patterning graphene on copper foil and baking off thin PMMA supports, are currently state-of-the art. The focus of the fabrication methods outlined above was to produce suspended graphene membranes for nanomechanical devices and imaging substrates. However, the techniques developed can be used for a wide variety of other novel

graphene devices. Now that we can reliably and controllably fabricate graphene devices, we expect that the next year will bring an exciting boom of new applications, and new scientific questions .

3.4 Characterizing Graphene

Once we have grown and fabricated the graphene based devices, we wish to characterize them. This section is a compendium of standard graphene characterization techniques used by our group while working with graphene. This section is meant as an introduction to graphene measurement techniques, and can be skipped by experienced researchers. We also use much more specialized techniques for particular experiments. We will discuss those techniques in along with their respective measurements.

3.4.1 Raman Spectroscopy

For a quantitative measure of layer number, we use Raman spectroscopy[15], which measures the energy shift of light due to inelastic scattering with phonon vibrations in the graphene lattice. Over the last few years, this technique has emerged as a powerful tool for carefully measuring the properties of graphene as varied as thermal conductivity[62], and strain[47].

Figure 3.11a shows the Raman spectrum of exfoliated graphite and graphene. Two large peaks are visible at 1580 cm^{-1}, and 2700 cm^{-1}, which researchers have labeled G and 2D for purely historical purposes. There is also one peak which is not visible at 1350 cm^{-1}, which is traditionally labeled D. Figure 3.11b shows a schematic of the phonon modes responsible for these peaks. The G peak is due to a degenerate carbon-carbon atom vibration. The D peak is due to a carbon ring breathing mode. The 2D peak is due to a higher-order double resonance of the

breathing mode. See Ferrari et al[15] for further details on the physical origin of these peaks.

The relative height and shape of these peaks tells us a lot about the layer number and structure of the graphene. In pristine graphene, the D peak is invisible. The D peak only shows up if there is some break in symmetry of the breathing mode of the ring. This symmetry break can be due to adsorbates, impurities, or the presence of sp-3 carbon bonds. The G peak will increase in height as more layers are added to the graphene but will not change shape. The 2D peak is very sensitive to layer number. Figure 3.11c shows that the 2D peak shape changes dramatically for the first few graphene layers, until the peak begins to resemble bulk graphite for $n > 5$. Looking at this shape is the easiest way to determine layer number. There are other more subtle variations such as precise peak position and width, which gives us more information about the graphene, but that is outside the scope of this paper.

Figures 3.11d-e show measurements using a Renishaw InVia Confocal Raman microscope of the typical Raman spectra of CVD grown graphene on (d) the copper growth substrate, and (e) shaped and suspended between gold electrodes in a finished device, like that shown in Figure 3.7d. The non-uniform background in both spectra is due to the presence of nearby copper or gold. In both cases, we can see that the 2D peak is a sharp single Lorentzian, and the 2D peak height is roughly twice the G peak height, indicating that the graphene is single layer. In the graphene grown on the copper, the D peak is below the measurement noise. In the patterned graphene, we see that the D peak has increased to roughly one quarter of the G peak height. Most likely, this increase in measured disorder is due to either the ragged edges created by shaping the graphene with oxygen plasma, or to photoresist contamination.

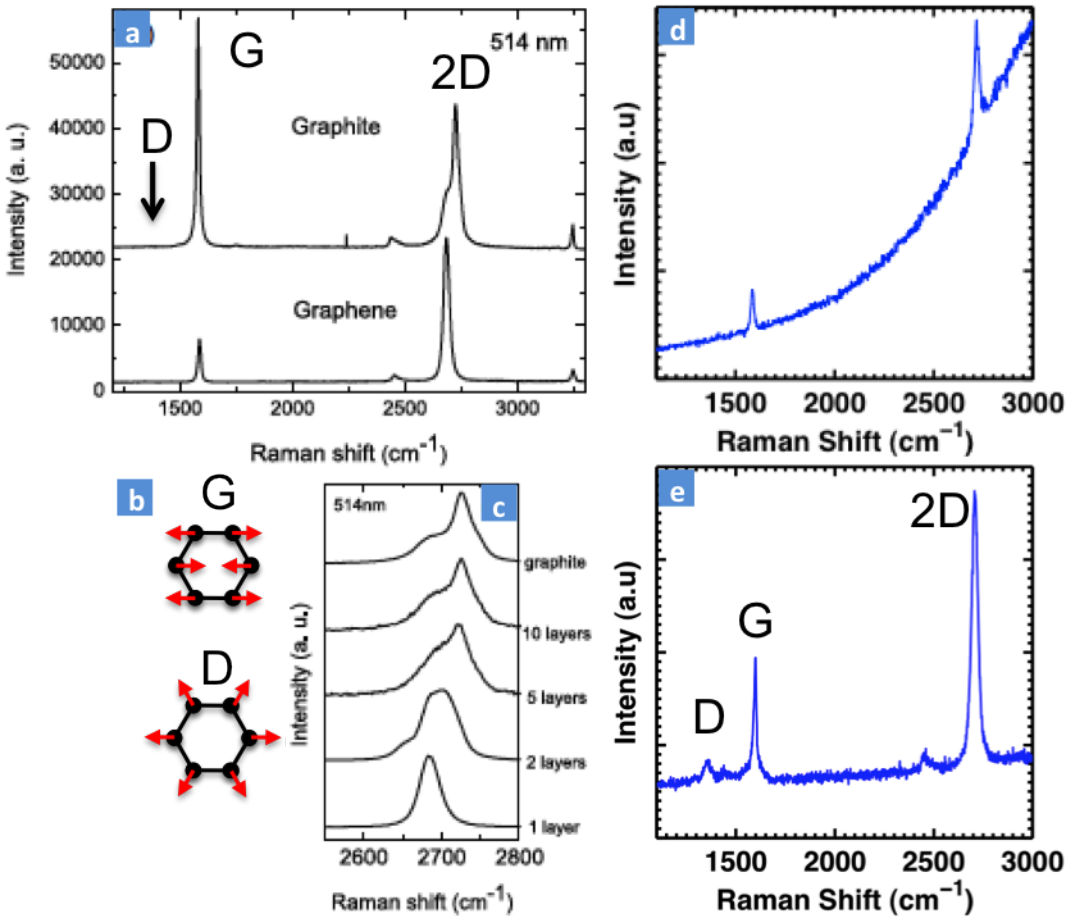

Figure 3.11: a) Raman spectra of graphite and exfoliated single-layer graphene from[15]. b) Schematic of the G and D phonon modes. c) Change in the 2D mode shape as a function of the number of graphene layers from[15]. d) Raman spectra of CVD graphene on copper. e) Raman spectra of CVD graphene as grown on copper foil and e) as a suspended membrane between gold electrodes.

3.4.2 Transport Measurements

We also use electrical transport as a measure of graphene quality.

We use the devices shown in Figure 3.12a to measure the intrinsic resistivity of graphene. In the four-point probe measurements shown, we measure the resistivity of graphene by injecting a current I_{SD} through the source-drain electrodes and then measure the voltage difference $V_1 - V_2$ on our probes. The resistivity of the graphene between the voltage probes is

$$R_{\square} = \frac{W}{L}\frac{V_1 - V_2}{I_{SD}} \tag{3.1}$$

Where W and L are the length and width of the graphene between the voltage probes. The advantage of this technique is that it allows us to ignore the contact resistance of the electrodes and measure the intrinsic resistivity of the graphene.

Figure 3.12c shows the electrical resistivity versus top-gate voltage of the top-gated electrically-contacted devices shown in Figure 3.12a-b. The peaked shape is related to the conical band structure of a graphene membrane as discussed in Section 2.2.

The resistivity is at a maximum when the Fermi level is at the Dirac point, where the density of states goes to zero in graphene. In the simplest case, the density of states will be zero when no potential is applied to the graphene. However, in most cases, the peak is offset away from zero due to trapped charge on the membrane or in the gate dielectric, which electrostatically dopes the graphene. We can roughly estimate the electrostatic doping of the graphene from the peak position.

$$n_0 = -\frac{C_g}{e} * V_{Dirac} \tag{3.2}$$

Where n_0 is the carrier density per unit area, C_{TG} is the capacitance per unit area

between the gate and the graphene, and V_{Dirac} is the position of the peak. We estimate the capacitance for a top-gated device as a parallel plate capacitor

$$C_{TG} = \frac{\epsilon_r \epsilon_0}{d} \tag{3.3}$$

Where ϵ_r depends on the top-gate dielectric material, and d is the dielectric thickness. For the device measured in Figure 3.12, the gate dielectric is evaporated silicon oxide $\epsilon_r = 3.9$ and $d = 90$ nm from which we estimate that the graphene is hole-doped with a density $n_0 = 5 * 10^{11}$ 1/cm^2.

On either side of the peak, the resistance drops off as the graphene is electron- or hole-doped away from the Dirac point. The peak is asymmetric due to hysteresis in the trace direction. Hysteresis is due to mobile charge trapped in the gate dielectric. The mobility is characterized by the amount of scattering of electrons in the graphene, which is a measure of the electronic disorder of the graphene. Mobility is defined as the relation of conductivity to charge doping.

$$G_{\square}(V - V_{Dirac}) = n(V - V_{Dirac})e\mu \tag{3.4}$$

Where $G_{\square}$ is the conductivity per square and $n(V)$ is charge per unit area. We use the differential change in conductivity to measure the mobility at any doping. In terms of measurable quantities on our plot, mobility is:

$$\mu = \frac{1}{R_{\square}^2} \frac{1}{C_{TG}} \frac{dR_{\square}}{dV_{TG}} \tag{3.5}$$

Where $\frac{dR_{\square}}{dV_{TG}}$ is the transconductance. Using this equation, we can extract a maximum mobility of the plot in Figure 3.12 of 9000 cm^2/Vs. We typically find room-temperature mobilities of 400 - 10,000 cm^2/Vs, comparable to previous results on CVD graphene[6, 2, 63] and only marginally less than mobilities reported for exfoliated graphene (1,000 - 20,000 cm^2/Vs)[10]. We will discuss how this mobility

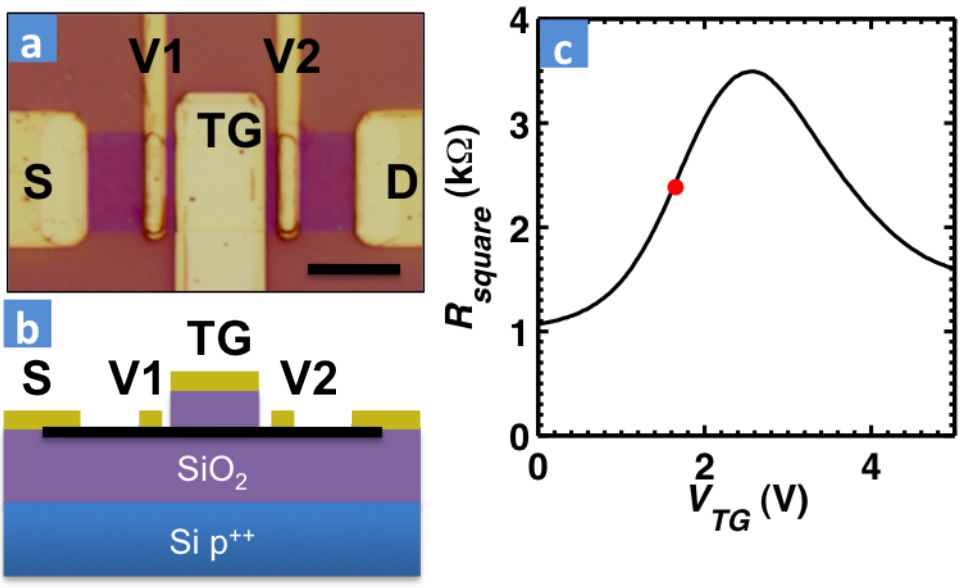

Figure 3.12: a) Contrast-enhanced optical image of top-gated electrically contacted graphene in four-probe geometry (Scale bar 10 μm). b) Side schematic of topgated graphene device. Material thicknesses are not to scale. c) Four-point transport measurement of graphene grown in Growth B as a function of top gate voltage. We extract a mobility of 9000 cm^2/Vs from the point of largest slope (red dot).

depends on graphene growth in the next chapter.

3.4.3 Electron Microscopy

We use both Scanning Electron Microscopy (SEM), Transmission Electron Microscopy (TEM) and Scanning Transmission Electron Microscopy (STEM) to measure the sub-micron structure of graphene, such as the integrity of graphene membranes, and the amount and type of contamination on them. We will discuss STEM measurements in detail in the next chapter.

In scanning electron microscopy (SEM), we raster a nm wide electron beam over a surface and measures the secondary electrons that scatter back towards the

detector. Most of the SEM images in this thesis were taken using either a Leo1150 FESEM or a Zeiss Ultra SEM. We use low extraction voltage of 2 kV to highlight the graphene contrast, and use the in-lens detector. We use SEM to check the integrity of graphene membranes. For example, most of the device images taken in Section 3.3 are SEM images showing whole graphene membranes. Figure 3.13 instead shows the three primary methods in which suspended graphene membranes fail: (a) Partial tearing of the membrane, (b) complete tearing of the membrane, and (c) stick down on to the substrate.

3.5 Discussion

In the first part of this chapter we described the procedures for building novel large arrays of suspended single-layer graphene membranes, with control over the location, size, shape, and clamping. These procedures are a huge step forward in graphene fabrication techniques, and are currently the state-of-the-art. In the second part of the this chapter, we described the standard characterization techniques that we use to characterize the graphene layer number, structural and electronic disorder, and membrane integrity. In the next chapter, we apply more advanced techniques to understand the polycrystalline grain structure and properties of the CVD grown graphene that we are producing and using. In Chapters 6 we use the suspended membranes as nanomechanical resonators, and examine their properties.

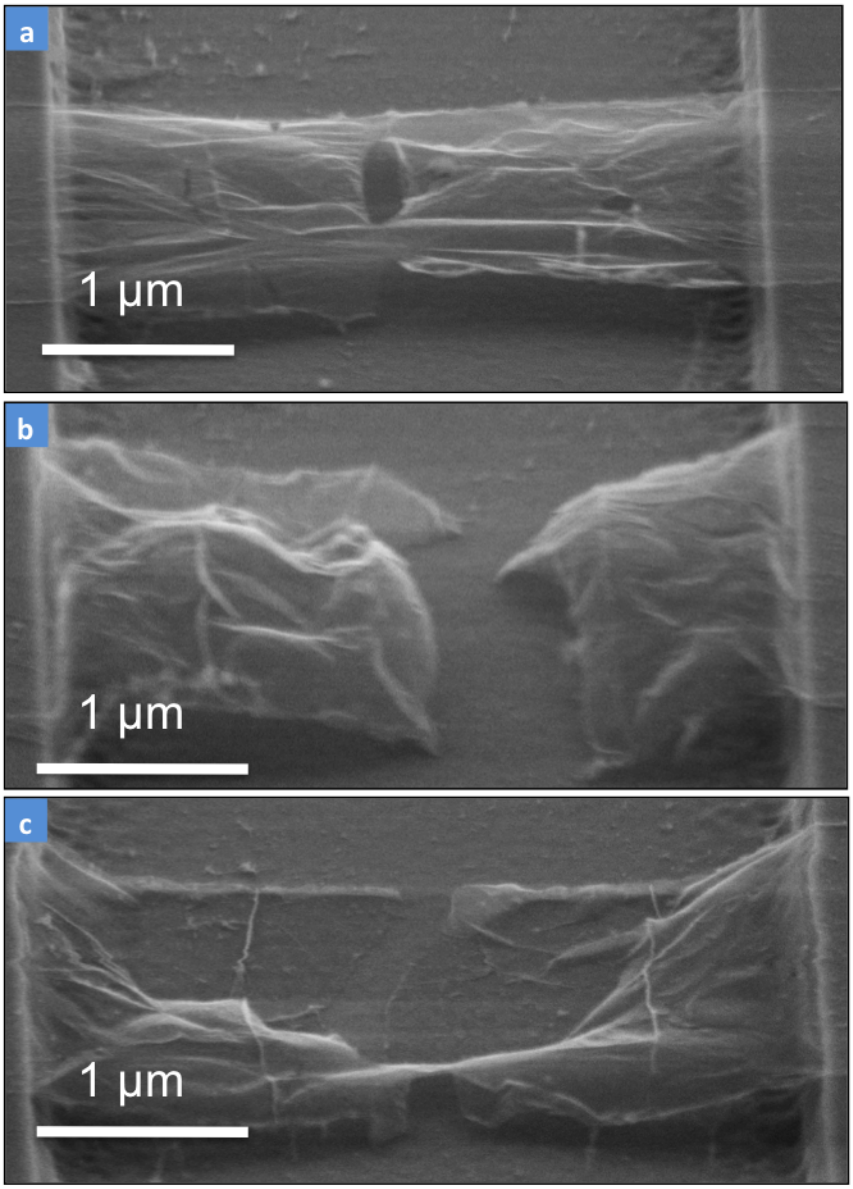

Figure 3.13: SEM of the three primary modes of failure in Doubly clamped graphene membranes. a) Membrane with partial tears in the surface. b) Fully torn membrane. c) Stuck down membrane.

Chapter 4

Grains and grain boundaries in single-layer graphene atomic patchwork quilts

4.1 Introduction

This chapter is adapted from a paper that has just been accepted to Nature, and is currently available on the arxiv[64].

The properties of polycrystalline materials are often dominated by the size of their grains and by the atomic structure of their grain boundaries. These effects should be especially pronounced in two-dimensional materials, where even a line defect can divide and disrupt a crystal. These issues take on practical significance in graphene, a hexagonal two-dimensional crystal of carbon atoms; Single-atom-thick graphene sheets can now be produced by chemical vapor deposition (CVD)[6, 28] on up to meter scales[2], making their polycrystallinity almost unavoidable. Indeed, early experiments have shown that by doing very short growths of graphene on copper, we see nucleation of graphene islands, as shown in Figure 4.1a. Theoretically, graphene grain boundaries are predicted to have distinct electronic[65, 66, 67, 68], magnetic[69], chemical[70], and mechanical[67, 71, 72, 73] properties which strongly depend on their atomic arrangement (Figures 4.1b). Yet, because of the five-order-of-magnitude size difference between grains and the atoms at grain boundaries, few experiments have fully explored the graphene grain structure. In this chapter, we use a combination of old and new transmission electron microscope (TEM) techniques to bridge these length scales. Using atomic-resolution

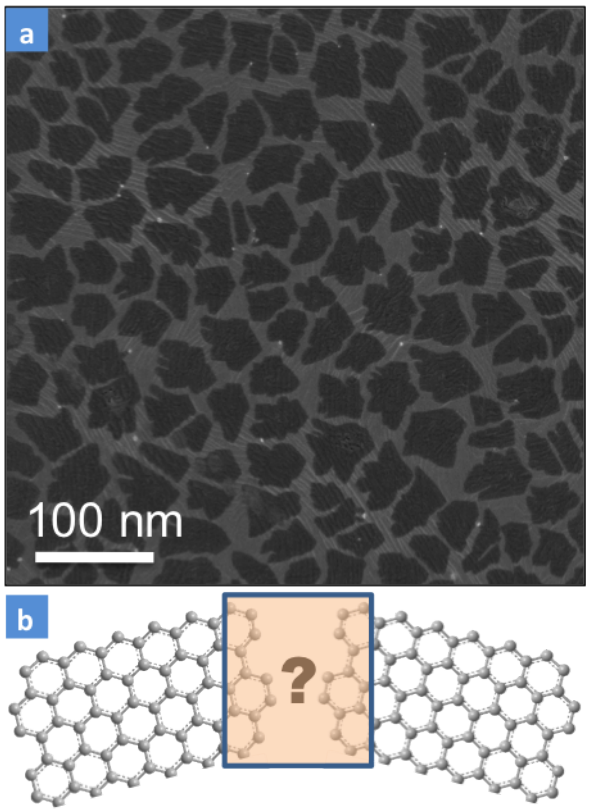

Figure 4.1: a) SEM of a sub-monolayer of graphene on copper. The graphene starts growing in nucleation islands. b) Two graphene crystals intersecting. How do the graphene crystals stitch together? What will be the mechanical and electrical properties of the grain boundary?

imaging, we determine the location and identity of every atom at a grain boundary and find that different grains stitch together predominantly via pentagon-heptagon pairs. Rather than individually imaging the several billion atoms in each grain, we use diffraction-filtered imaging[74] to rapidly map the location, orientation, and shape of several hundred grains and boundaries, where only a handful have been previously reported[54, 53, 75, 22]. The resulting images reveal an unexpectedly small and intricate patchwork of grains connected by tilt boundaries. By correlating grain imaging with scanned probe and transport measurements, we show that these grain boundaries dramatically weaken the mechanical strength of graphene membranes, but do not as dramatically alter their electrical properties. These techniques open a new window for studies on the structure, properties, and control of grains and grain boundaries in graphene and other two-dimensional materials.

Figure 4.2a shows a large array of the suspended, single-layer graphene membranes used in this study. We grew predominately single-layer graphene films on copper foils via CVD[6, 56] using three different growth recipes, which we refer to as Growth Methods A, B, and C. Unless otherwise stated, all data were taken on graphene grown with Method A, which was similar to the recipe reported in Reference 1. Methods B and C are slight variations: Method B uses 99.999% ultrapure copper foils[76] rather than 99.8%, and Method C uses the same recipe except in a rapid thermal processor furnace. These films were transferred them onto holey silicon nitride or Quantifoil TEM grids using the two techniques described in Sections 3.3.4 and 3.3.5. One key innovation over previous graphene TEM sample fabrication[61] was gently transferring the graphene onto a TEM grid using a minimum of polymer support and baking the samples in air to remove the polymer without liquid solvents. This produces large arrays of free-standing graphene sheets covering up to 90% of TEM grid holes.

4.2 Graphene grain boundaries

To characterize these membranes at the atomic-scale, we used aberration-corrected annular dark-field scanning transmission electron microscopy (ADF-STEM), where a 60 keV angstrom-scale electron beam is scanned over the sample while the medium- to high-angle scattered electrons are collected. Keeping the electron beam voltage below the ∼100 keV graphene damage threshold was necessary to limit beam-induced damage. Properly calibrated, this technique images the location and atomic number[77] of each atom and, along with TEM, has been used to study the lattice and atomic defects of graphene and boron nitrene [77, 78, 79]. Figure 4.2b shows an ADF-STEM image of the crystal lattice within a single graphene grain. Away from the grain boundaries, such regions are defect-free.

In Figure 4.2c, two graphene grains meet with a relative misorientation of 27°, forming a tilt boundary. As highlighted in Figure 4.2d, the two crystals are stitched together by a series of pentagons, heptagons, and distorted hexagons. The grain boundary is not straight, and the defects along the boundary are not periodic. While the boundary dislocation resembles structures proposed theoretically[71, 73], its aperiodicity contrasts with many of these models and will strongly affect the predicted properties of grain boundaries. By analyzing atomic scattering intensities[77], we confirm the boundary is composed entirely of carbon. In addition, while high electron beam doses could induce isolated bond-rotations similar to those seen in[80], the boundary was largely stable under the 60 keV electron beam. Thus, the polycrystalline graphene is a strongly-bonded, continuous carbon membrane. We also note that many grain boundaries are decorated by lines of surface particles and adsorbates as seen later in Figure 4.6, suggesting that as predicted[70], they may be more chemically reactive than the pristine graphene lattice.

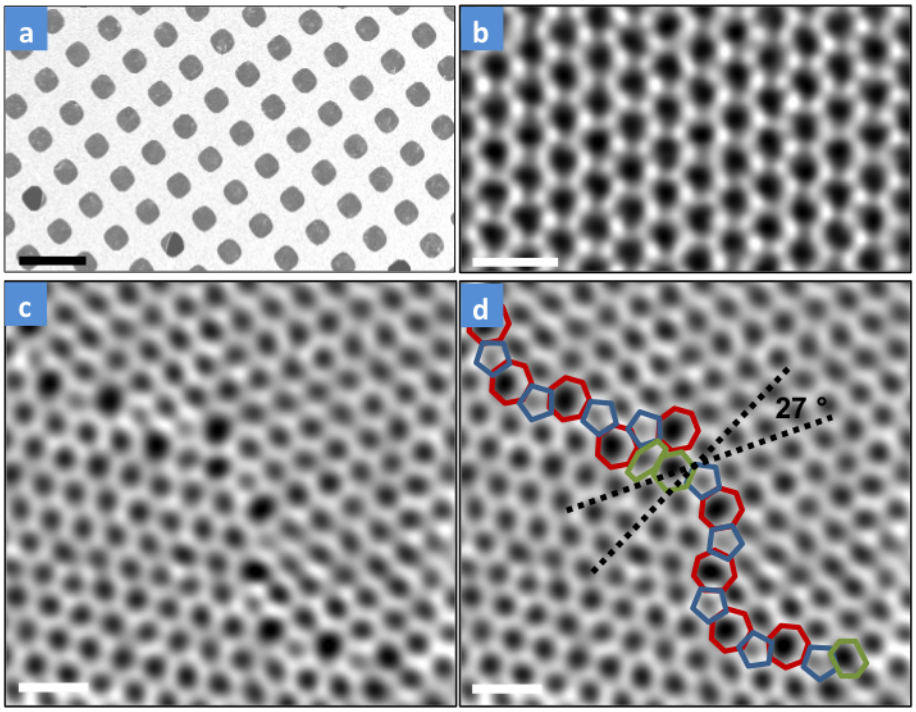

Figure 4.2: Atomic-resolution ADF-STEM images of graphene crystals. a) An SEM image of graphene transferred onto a TEM grid with over 90% coverage via novel high-yield methods. Scale bar 5 μm. b) An ADF-STEM image shows the defect-free hexagonal lattice inside a graphene grain. c) Two grains (bottom left, top right) intersect with a 27° relative rotation. An aperiodic line of defects stitches the two grains together. d) The image from c) is overlaid with a trace of pentagons (blue), heptagons (red), and distorted hexagons (green). Images b-d) were low-pass filtered to remove noise. Scale bars in (b-d) are 5 Å.

4.3 Graphene grain structure

Both (S)TEM, which determines the positions and identities of atomic nuclei, and complementary STM probing valence wavefunctions[54, 53, 75, 81] are invaluable for understanding the local properties of grain boundaries. Using these atomic-resolution approaches, however, tens to hundreds of billions of pixels would be needed to fully image even a single micron-scale grain, with estimated acquisition times of a day or more. Other candidates for characterizing grains on larger scales, such as LEEM[22] and Raman microscopy[56], typically cannot resolve small grains and may be difficult to interpret. Fortunately, electron microscopy offers an ideal technique to image grains on the necessary length scales: dark-field TEM (DF-TEM), a high-throughput, diffraction-sensitive imaging technique[74] that can be implemented on most TEMs built in the last sixty years. While this method is usually applied to hundred-nanometer-thick foils[74], we demonstrate below that remarkably, it also works on single-atom thick sheets − even on samples too dirty for atomic resolution imaging, or on samples on up to 10 nm amorphous substrates. In this manner, DF-TEM provides a nanometer- to micron-scale grain analysis that complements ADF-STEM to give a complete understanding of graphene grains on every relevant length scale.

Figures 4.3a and 4.3b show a bright-field TEM image of a graphene sheet along with the selected area electron diffraction pattern created from this region of the membrane. Due to graphene's sixfold symmetry, electron diffraction from a single graphene crystal results in one set of sixfold-symmetric spots. Figure 4.3b contains many such families of spots, indicating that the field of view contains several grains of different orientations. DF-TEM images these grains one-by-one with few-nanometer resolution using an objective aperture filter in the back focal plane to collect electrons diffracted to a small range of angles, as shown by the

circle in Figure 4.3b. The resulting real-space image (Figure 4.3c) shows only the grains corresponding to these selected in-plane lattice orientations and requires only a few seconds to acquire. By repeating this process using several different aperture filters, then coloring and overlaying these DF-images, (Figure 4.3d,e), we create complete maps of the graphene grain structure, color-coded by lattice orientation, as shown in Figure 4.3e-g.

The images obtained are striking. The grains have complex shapes and many different crystal orientations. In Figure 4.3e-g, we observe special locations from which many grains emanate. Small particles and multilayer graphene also are often found near these sites (e.g. Figure 4.3e, top right). Both the average spacing (2-4 μm) and shapes of these radiant sites in Growth Method A are comparable with previous studies of graphene nucleation on copper foils using Raman and SEM[6, 56], suggesting that these locations are likely nucleation sites. Similar structures have been observed in studies of crystallization in colloids and are consistent with crystallization around impurities[82]. Similar multi-grain nucleation on copper has recently been observed using LEEM[76]. Significantly, each apparent nucleation site gives rise to many grains of different orientation, resulting in a mean grain size much smaller than the nucleation density.

4.4 Statistics

The distributions of grain size and relative angular orientation are readily determined from DF-TEM images. As discussed later in the text and in Figure 4.5, grain sizes are dependent on growth conditions. In Figure 4.4a, we plot a histogram of grain sizes across several samples grown using Growth Method A. The mean grain size, defined as the square root of the grain area, is 250 ± 11 nm. This size is much smaller than the grain size of the copper substrate (100 μm- 1mm)[6, 2]

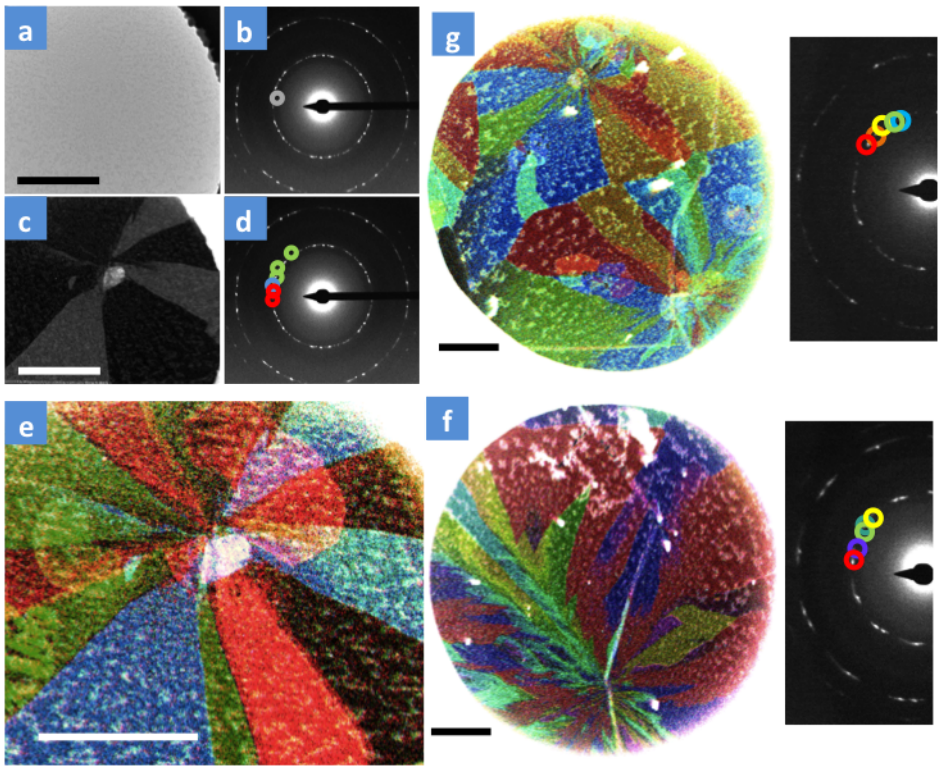

Figure 4.3: Large-scale grain imaging via DF-TEM. a-e), Grain imaging process. a) Samples appear uniform in bright-field TEM images. b) A diffraction pattern taken from a region in a) reveals that this area is polycrystalline. Placing an aperture in the diffraction plane filters the scattered electrons forming c) a corresponding DF-image showing the real-space shape of these grains. d) Using several different aperture locations and color-coding them produces e) a false-color DF-image overlay depicting the shape and lattice orientation of several grains. f-g) Images of regions where many grains emanate from a few points. Scale bars 500 nm.

and typical lateral grains measured in bulk HOPG (6-30 μm)[83]. We find similar results in samples fabricated from several different growth runs and in two separate CVD furnaces. The inset in Figure 4.4a shows the cumulative probability of finding multiple grains in a given area. This plot demonstrates that micron-scale CVD graphene devices produced from this set of films will nearly always contain multiple grains. Figure 4.4b shows a histogram of the relative crystallographic angles between adjacent grains. With graphene's sixfold crystal symmetry, the diffractive-imaging technique only determines grain rotations modulo 60°. Consequently, the measurable difference between grain orientations is from 0-30° (i.e. 31° is measured as 29°). We observe a surprising and robust preference for low-angle ($\sim 7°$)grain boundaries and high ($\sim 30°$) angle boundaries similar to the one seen in Figure 4.2.

Additional information about these orientations comes from the larger-area diffraction patterns in Figure 4.4c, created by averaging diffraction data sampled across 1200 μm^2 regions of graphene. The broadened diffraction peaks in Figure 4.4c (left) show a distinct sixfold pattern, indicating that a significant fraction of the grains are approximately aligned across large areas. This alignment can also be seen in Figure 4.4d, a low-magnification DF-TEM image displaying grains with a small ($\sim 10°$) range of in-plane lattice orientations. Almost half of the membrane appears bright, indicating these grains are all approximately aligned. In contrast, a DF-image of randomly oriented grains would only show roughly one-sixth (10°/60°) of the graphene membrane. In the diffraction pattern of a separately grown sample, (Figure 4.4c, right), we instead find a clear 12-fold periodicity, indicating that there are two main families of grains rotated $\sim 30°$ from one another. These distributions, which often contain smaller sub-peaks, are consistent with the frequent observation of low and high 30° grain boundaries. We

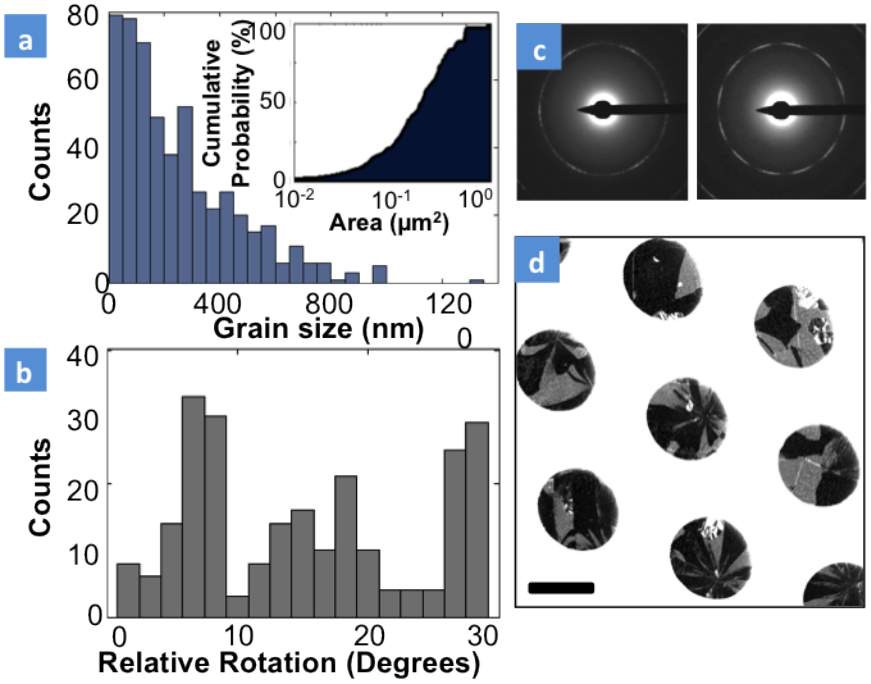

Figure 4.4: Statistical analysis of grain size and orientation. a) A histogram of grain sizes, taken from three representative samples using DF-TEM. The mean grain size is 250 11 nm. a inset) Plot of the cumulative probability of having more than one grain given the area of a device. b) A histogram of relative grain rotation angles measured from 238 grain boundaries. c) Large-area diffraction patterns and d) a low-magnification DF-TEM image show that grains are globally aligned near particular directions. Scale bar 2 μm.

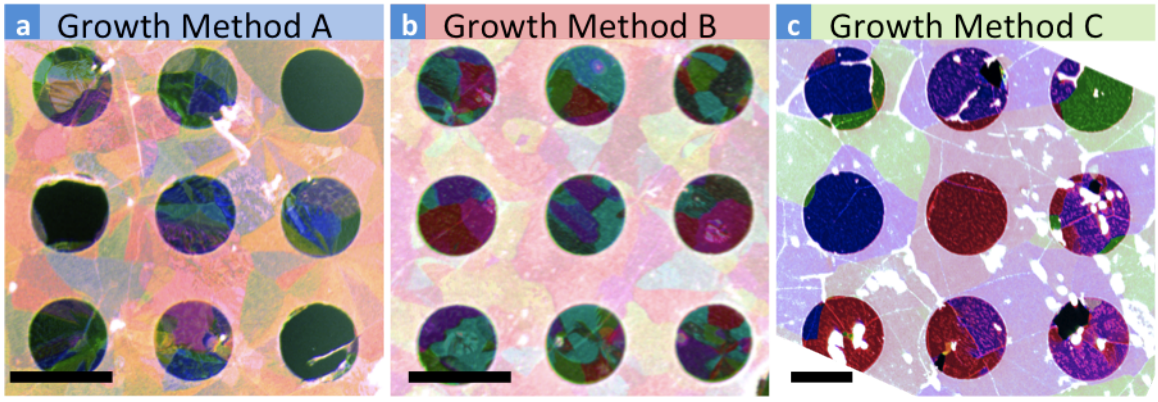

Figure 4.5: a-c) Composite DF-TEM images of grain structure variations with growth condition. Scale bars are 2 microns.

attribute these alignments to registry to the copper substrate used for graphene growth. Such registry has recently been observed in LEEM and STM studies of graphene growth on Cu (100) and (111) surfaces[54, 53, 76].

By directly correlating grain structure with growth methods, these DF-TEM methods can be used to build upon recent studies[84] that have demonstrated links between island nucleation density and growth conditions. Figure 4.5a-c shows three composite DF-TEM images of graphene from Growth Methods A, B, and C. These slight alterations of the growth conditions effected significant changes in the grain size, shape, and crystallographic orientation of the CVD graphene. For example, with Growth Method C, we observed grains averaging 1-4 μm (Figure 4.5c), an order of magnitude larger than the grains in Growth Method A. Our DF-TEM methods provide a powerful characterization tool for understanding and controlling grain growth, which will be a rich field of study important for graphene applications.

4.5 Mechanical and electrical properties of grain boundaries

The ability to easily image the grain structure in graphene monolayers opens the door to the systematic exploration of the effects of grain structure on the physical, chemical, optical, and electronic properties of graphene membranes. We find such studies are further facilitated because grain boundaries are visible in scanning electron microscopy (SEM) and atomic force microscopy (AFM) phase imaging due to preferential decoration of the grain boundaries with surface contamination.

Figure 4.6 demonstrates that the decoration allows us to see the grain boundaries using a variety of different microscopy techniques in addition to DF-TEM and ADF-STEM. Figure 4.6(a-b) show the same region of suspended graphene measured using DF-TEM and SEM. This image shows a strong correlation between grain boundaries and contamination lines seen in SEM. Similarly, Figure 4.6(c-d) shows the same region of suspended graphene measured using STEM and AFM phase imaging. The decoration makes the grain boundaries visible because it has increased electron-sample interaction in SEM and STEM, and because it changes the tip-surface interaction in AFM. For these imaging techniques, the graphene needs to be suspended and relatively clean. Unfortunately, we find that doing photolithography on the graphene deposits enough carbon and other surface particles to obscure the grain boundaries.

Below, we show two examples probing the electrical and mechanical properties of grain boundaries.

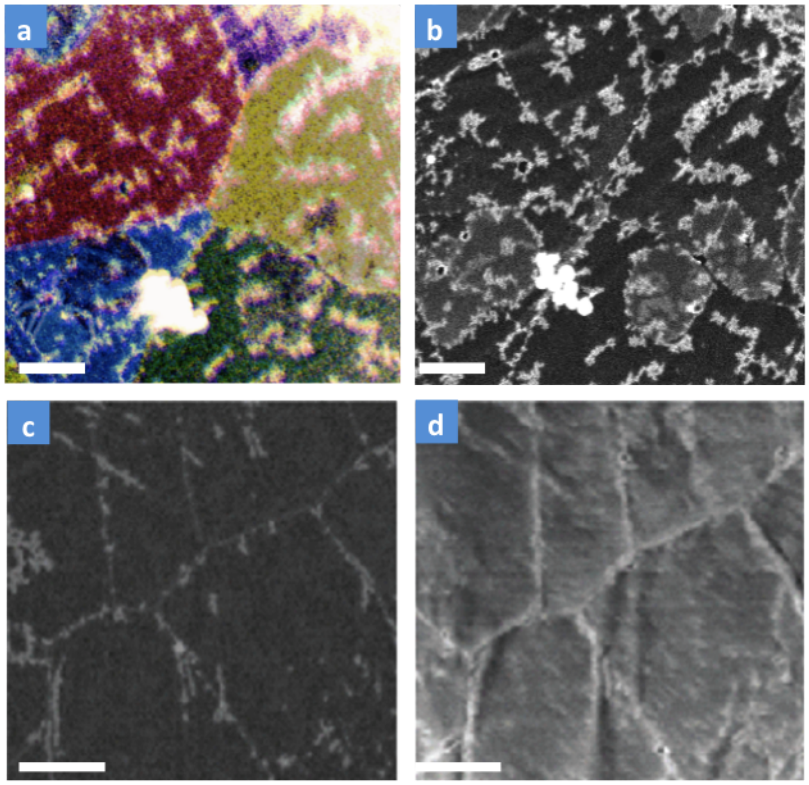

Figure 4.6: Direct comparisons of a) composite DF-TEM and b) SEM images of the same region. We also show similar comparisons between c) ADF STEM, and d) AFM phase images of a second region. Decorated grain boundaries are visible in SEM, STEM, and AFM phase images. Scale bars are 250 nm.

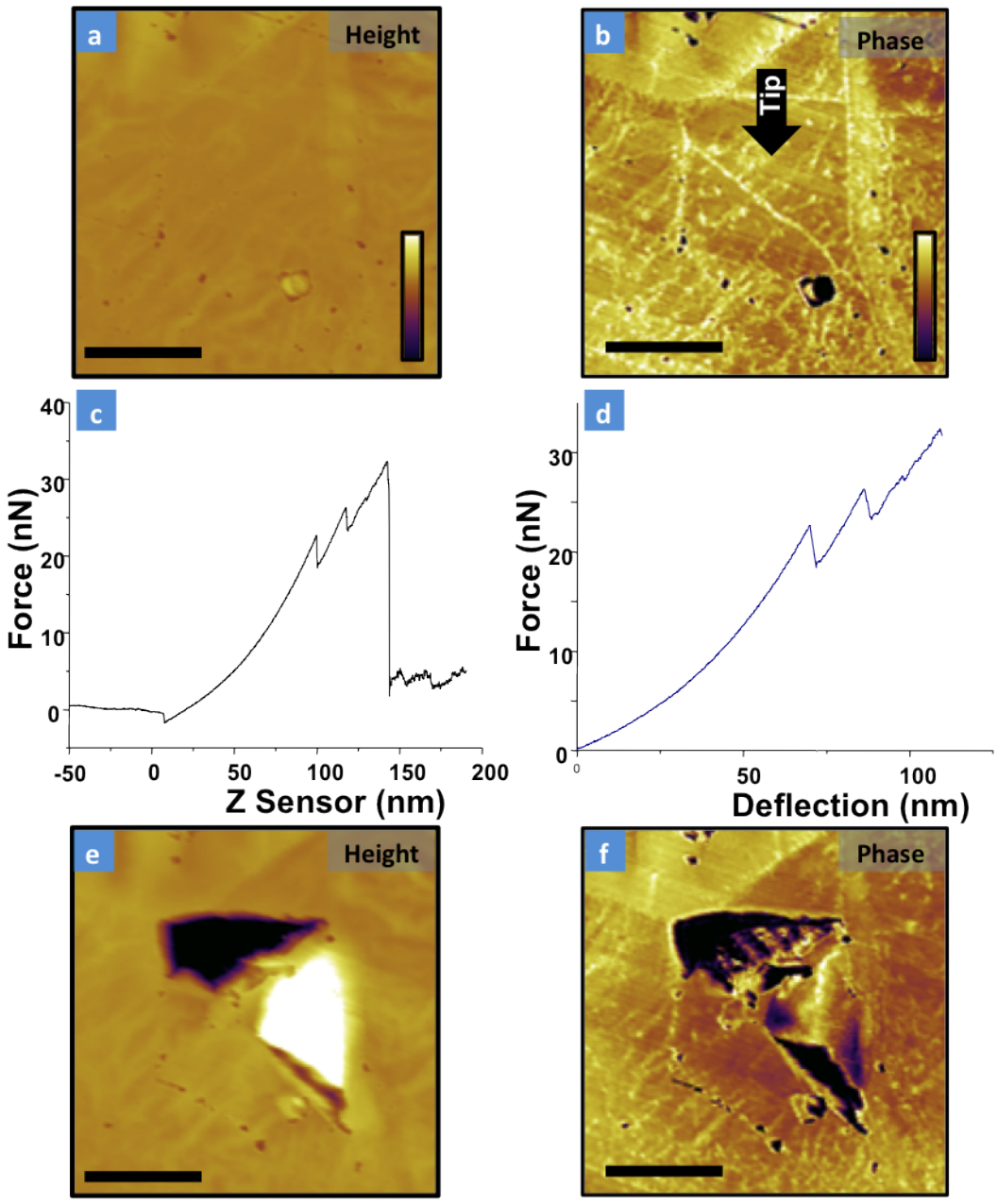

Figure 4.7: a) AFM height and b) phase images of a suspended region of graphene. The grain boundaries are clearly visible in the phase image. c) Force curve from pushing at the point indicated by the arrow in b) with the AFM tip. d) Force versus membrane deflection extracted by assuming the spring constant of the AFM cantilever. The membrane tears at a load is 35 nN in this device. e) The AFM height and f) phase images of the same region after pushing. The graphene has torn along the grain boundaries.

4.5.1 Mechanical properties of grain boundaries

We first examine the failure strength of these polycrystalline CVD graphene membranes (Growth Method A) using AFM. We used AFM height and phase imaging to image a suspended membrane as shown in Figure 4.7a-b) and then pressed downward at the center one grain with the AFM tip to test the mechanical strength of the membranes. Figure 4.7c shows the force on the membrane versus position of the tip. The force is calculated by the simple equation $F = kz_{tip}$ where $k = 3$ N/m is the spring constant of the cantilever and z_{tip} is the tip deflection. The deflection of the graphene membrane is calculated by subtracting the tip deflection from the Z position of the AFM piezo, which we show in Figure 4.7d.

From the force distance curves, we can extract the mechanical properties of graphene. We can use the model described in that study to measure the 2D elastic modulus, obtained by fitting deflection curves to the following equation:

$$F = \sigma \pi z + Yt\frac{(qz)^3}{D^2} \tag{4.1}$$

Where σ_0 is the 2D pretension, D is the radius of the graphene sheet, z is the deflection of the graphene at its center, and q, a function of the Poisson ratio, is taken to be 1.02. We found values for the effective elastic modulus to be a factor of $\sim$6 smaller than those reported by Lee et al for pristine graphene, but further discussion on the possible causes of this diminished elastic response lie outside the scope of this thesis, and is still work in progress.

The breaking load was read from the force curves as the point where the force exerted on the tip returns to zero or nearly zero. We see smaller breaking events in some force plots, where the force experienced only small drops, suggesting that smaller tears in graphene can occur before its complete failure. From repeated measurements, we find that failure occurs at loads of about $\sim$ 100 nN, an order of

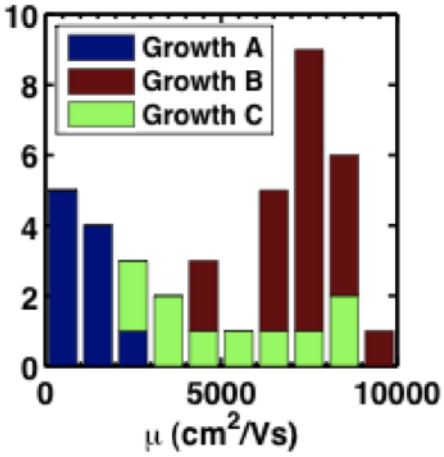

Figure 4.8: Vertically stacked histogram of mobilities from 50 devices for graphene devices grown under the three growth conditions shown in Figure 4.5

magnitude lower than typical fracture loads of 1.7 μN reported for single-crystal exfoliated graphene[12].

Figure 4.7e-f, shows the same region of graphene as Figure 4.7a-b) after tearing. We see that the graphene tears along the grain boundaries. Thus, the strength of polycrystalline graphene is dominated by its grain boundaries.

4.5.2 Electrical properties of grain boundaries

We probed the electrical properties of polycrystalline graphene by fabricating the electrically-contacted devices described in Section 3.3.1 using graphene from the three growth methods shown in Figure 4.5. Following the procedure described in Section 3.4.2, we used four point probemeasurements to extract the mobility for each growth. Figure 4.8 shows a histogram of mobilities extracted from four-point transport measurements. Note that the respective electrical and DF-TEM measurements of each growth method are taken from the exact same pieces of copper foil, which are split after growth. Growth Methods A, B, and C exhibit

room temperature mobilities of 1000 ± 750, 7300 ± 1100, and 5300 ± 2300 (s.d.) cm^2/Vs, respectively. The mobilities of Growth Method A are comparable to previous results on CVD graphene[6], while the mobilities of Growth Methods B and C are closer to the room temperature mobilities reported for exfoliated graphene (1,000 - 20,000 cm^2/Vs)[10]. By comparing these measurements against the corresponding DF-TEM images in Figure 4.5a-c, we find that surprisingly, while mobility is clearly affected by growth conditions, high mobility does not directly correlate with large grain size.

To complement these bulk electrical measurements, we used scanned probe AC-Electrostatic Force Microscopy (AC-EFM)[85] to look for effects from individual grain boundaries. We fabricated suspended membrane devices[63], shown schematically in Figure 4.9a. Figures 4.9c-d show the topography and phase images of an electrically contacted suspended graphene device, which correspond directly to the device schematic shown in Figure 4.9a. Unlike previously shown phase images, no grains are visible on the graphene surface because these features are obscured by extra contamination accumulated during the lithographic shaping. We performed AC-EFM measurements[85] on electrically contacted suspended graphene membranes using the circuit shown in Figure 4.9b. Figure 4.9e shows the measured signal when driving the left electrode, the right electrode, and both electrodes respectively. By taking the ratio of the signals when the device is driven on one side and on both sides, we cancel out signals due to contamination and changing materials and measure the relative electrostatic potential along the device. Figure 4.9f shows the ratios of the data in Figure 4.9e with the images X-Y correlated to account for spatial drift, giving the potential as a function of position.

Figure 4.9g shows the relative potential along a graphene membrane between two biased electrodes measured using AC-EFM. In this plot, high-resistance grain

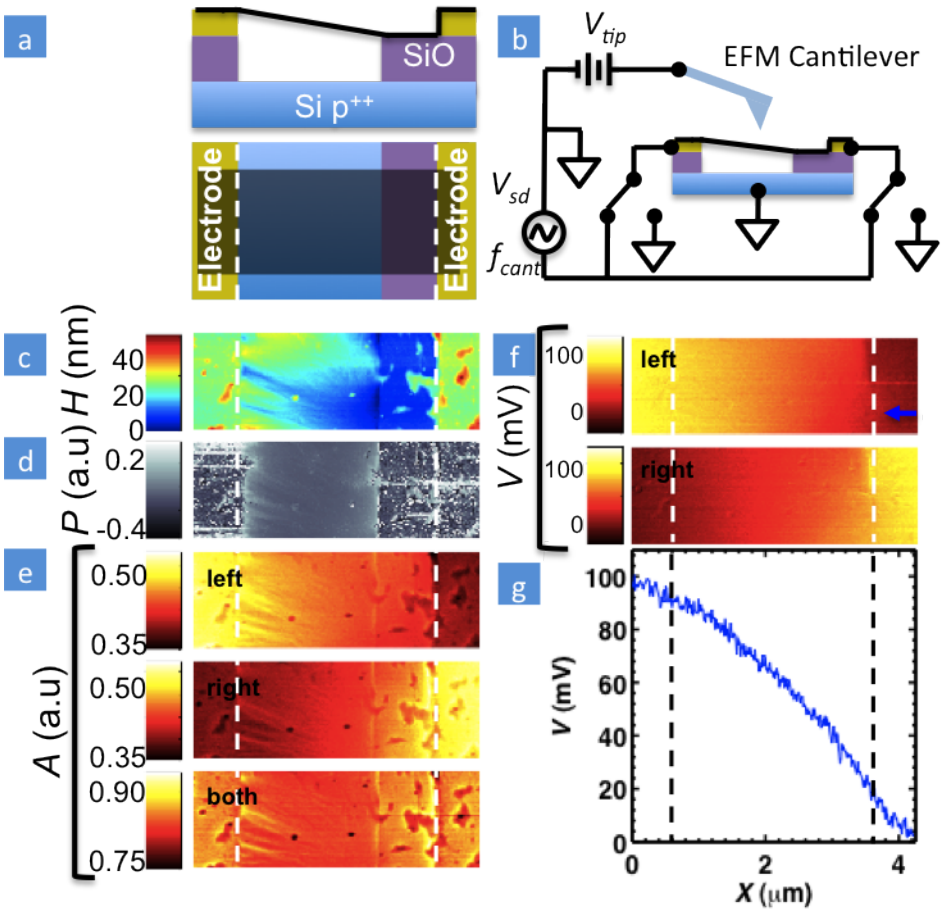

Figure 4.9: a) Side and top schematics of suspended electrically contacted graphene. b) Schematic of AC-EFM measurement setup. c) AFM topography and d) phase images of a suspended electrically contacted sheet of graphene. e) AC-EFM images when driving the left, right and both electrodes respectively. f) Ratio of left and right driven electrode EFM images to both electrode driven image. This ratio is proportional to electrostatic potential along the sheet. Features due to changing contaminants and topography of the images disappear. Color bar rescaled by applied V_{sd} voltage to give electrostatic potential on graphene sheet. g) Single line trace from ratio image taken along blue arrow in figure (f). All images are 4.2 μm across, and dashed lines indicate electrode locations.

boundaries would manifest as sharp drops in potential. Using the mean grain size from Figure 4.4a, a line scan across these 3 μm long membranes should cross an average of 12 grains. However, no noticeable potential drops were detected, indicating that most grain boundaries in these devices are not strongly resistive interfaces. By assuming a grain boundary running perpendicular to the line scan, we estimate an upper bound on the grain boundary resistance of $R_{GB} < 60\ \Omega - \mu m/L$, where L is the length of the grain boundary, compared to $R_{\square} = 700\ \Omega/\square$ for the entire device. In other words, the resistance of the grain boundaries is less than one-third the resistance of a 250 nm grain. This stands in stark contrast to other materials such as complex oxides, where a single grain boundary can lead to a million-fold increase in resistance over single crystals[86]. Measurements on five additional graphene membranes, both suspended and unsuspended, and from different growth methods, produced similar results.

4.6 Conclusions

The imaging techniques reported here provide the tools to characterize graphene grains and grain boundaries on all relevant length scales. These methods will be crucial both for exploring synthesis strategies to optimize grain properties and for studies, such as those demonstrated above, on the microscopic and macroscopic impact of grain structure on graphene membranes. Thus, these results represent a critical step forward in realizing the ultimate promise of atomic membranes in electronic, mechanical and energy-harvesting devices.

Chapter 5

Graphene Mechanical Resonators

In addition to studying the structure and properties of graphene we can also use suspended graphene membranes as a new class of nano-electro-mechanical system (NEMS). In this chapter, we review our early experiments studying graphene-based nanomechanical resonators and describe the measurement techniques that have made this possible.

A mechanical resonator is defined by two simple quantities. First is the resonance frequency: $\omega_0 = 2\pi f_0$, which is the frequency that the structure naturally vibrates at, and the quality factor $Q = \frac{\omega_0}{\delta\omega}$, which defines the width of the resonance. Physically, the resonance frequency is a measure of the stiffness and mass of the system, and the quality factor is a measure of the energy loss rate in the system.

$$Q = 2\pi \frac{E_{total}}{\Delta E_{cycle}} \tag{5.1}$$

The higher the quality factor, the more isolated the mechanical resonator is from its environment, and the narrower the resonance width is.

For most applications of nanomechanical resonators, we want the resonator mass m_{eff} to be as small as possible and the quality factor to be as large as possible. For example, in mass sensing[7, 87], where the minimum detectable mass δm by a resonator of mass m_{eff} is

$$\delta m = \frac{m_{eff}}{Q} 10^{-DR/20} \tag{5.2}$$

Where DR is the dynamic range (in DB) of minimum detectable signal to nonlinear behavior. The ratio $\frac{m_{eff}}{Q}$ sets the ultimate sensitivity.

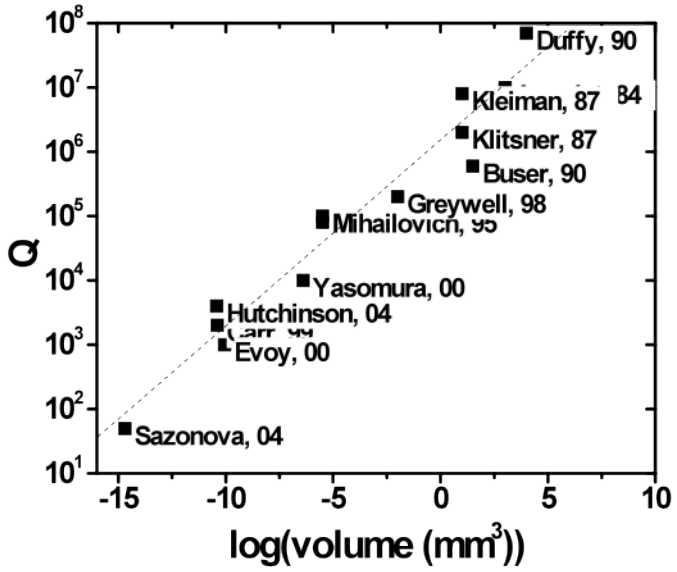

Figure 5.1: Quality factor dependence on the size of mechanical resonators from many different groups.

However, the quality factor and resonator size are not independent. Figure 5.1 shows that the quality factor at room temperature of many different kinds of mechanical resonators decreases with the size of the resonator[88, 16]. Much of NEMS research has focused on decreasing the mass of resonators while still maintaining a high quality factor. Graphene provides the ultimate limit in thickness, and so holds promise for being an excellent material to use for NEMS.

5.1 Flexural mechanical resonators resonators theory

Before reviewing the graphene resonator experiments, we need to discuss what we expect to see. In this section, we review the theory of mechanical resonance and describe the predictions for resonance frequency of doubly-clamped and fully-clamped graphene membranes from continuum mechanics. These theories make

predictions for the mode shape, the fundamental mode frequency, the scaling of frequency with size , and the position of higher harmonics for all of the suspended membrane geometries we use in our experiments.

5.1.1 Simple Harmonic Oscillator

Any mechanical resonator that obeys Hooke's and Newton's laws (Eq. 1.1 and 1.2), from a mass on a spring, to a violin string, to a graphene sheet suspended over a trench, is described by the linear differential equation of motion:

$$f(t) = m_{eff}\frac{d^2z}{dt^2} + 2m_{eff}\Gamma\frac{dz}{dt} + k_0 z \tag{5.3}$$

Where $f(t)$ is a time dependent force, m_{eff} is the effective mass, z is the displacement from equilibrium, Γ is the rate of energy dissipation, and k_0 is the spring constant. This differential equation is called the (damped, driven) simple harmonic oscillator equation, because, if we drive the system with a harmonic force:

$$f(t) = F_0 e^{i\omega t} \tag{5.4}$$

Where F_0 is some arbitrary drive amplitude and ω is a drive frequency, then the system will respond with with oscillating motion $z(t)$:

$$z(t) = z_0(\omega)cos(\omega t + \phi(\omega)) \tag{5.5}$$

where the amplitude $z(\omega)$ and phase $\phi(\omega)$ depend on the frequency, as shown in Figure 5.2.

$$z_0(\omega) = \frac{F_0}{m_{eff}}\frac{1}{\sqrt{\left(\omega_0^2 - \omega^2\right)^2 + \left(\frac{\omega\omega_0}{Q}\right)^2}} \tag{5.6}$$

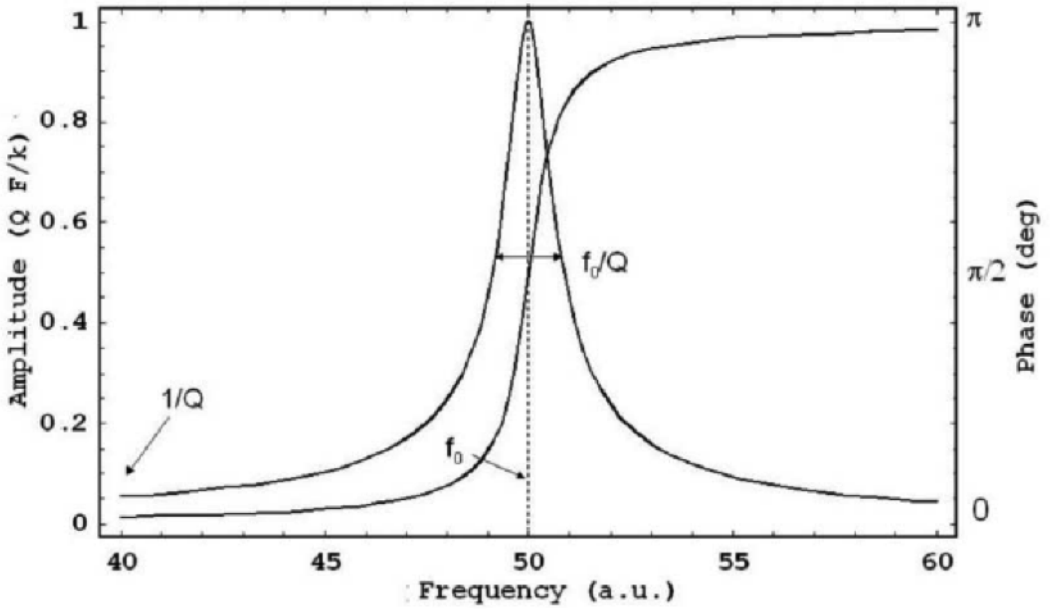

Figure 5.2: Amplitude and phase versus drive frequency from[16].

$$tan(\phi) = \frac{\left(\frac{\omega\omega_0}{Q}\right)^2}{\left(\omega_0^2 - \omega^2\right)^2} \tag{5.7}$$

where

$$\omega_0 = \sqrt{\frac{k_0}{m_{eff}}} \tag{5.8}$$

and

$$Q = \frac{\omega_0}{2\Gamma} \tag{5.9}$$

are the resonance frequency and quality factor as discussed in the previous section.

5.1.2 Mechanical resonance of beams and membranes

We can extend the idea of mechanical resonance to mechanical beams and membranes. Mechanical resonance is a well understood problem in continuum mechanics[89]. We can break up any large object into tiny elements and calculate the forces on

each element using Equation 2.5. We then sum up the forces of all the individual element to get the total force on an object due to any perturbation.

The precise resonance frequency depends strongly on the geometry of the mechanical resonator. We will look at two specific cases relevant to our geometries: perpendicular vibrations of a long 1D beam, and out of plane vibrations of a thin 2D membrane.

1D beam

According to continuum mechanics, the resonance frequency of fluctuations out of plane for a straight beam of length L_0 is

$$\omega_n^2 = k_n^4 \frac{B}{\rho} + k_n^2 \frac{N}{\rho} \tag{5.10}$$

where N is the initial tension in the beam, B is the bending rigidity (Eq. 2.7), ρ is the mass per unit length, n refers to the harmonic mode number, and k_n is a geometric coefficient which depends on the clamping conditions. The first term in Equation 5.10 is the bending frequency. If there is no tension in the beam, then this is the only term that matters.

We can predict the bending rigidity in 3D objects. According to continuum mechanics, the bending rigidity of the beam depends on the material strength and the cross-sectional shape:

$$B = E\mathcal{I} \tag{5.11}$$

where $\mathcal{I}$ is the moment of intertia. For a rectangular beam of thickness t, length L, and width W and curvature along the length in the direction of the thickness, the moment of inertia is:

$$\mathcal{I} = \frac{1}{12}\frac{Wt^3}{L^3} \tag{5.12}$$

In a flat 2D membrane, there is no thickness, and we have to calulate the intrinsic bending modulus $B = B_0 \times W$ from molecular dynamics, as discussed in Chapter 2.

The second term in Equation 5.10 is the change in frequency due to tensioning the beam. In the limit of high in-plane uniaxial strain ϵ, the tension $N = YtW\epsilon$, is large enough to overcome the bending rigidity, and this term dominates.

Clamping

The clamping constants k_n depend on whether the bending term or the stretching term is larger. By taking the ratio of the two terms, we can see if we are in the bending regime or the stretching regime.

$$\frac{k_n^2 \frac{N}{\rho}}{k_n^4 \frac{B}{\rho}} \approx \frac{L^2 N}{B} \tag{5.13}$$

If the stretching energy dominates, the the eigenmodes are string-like, and the resonance harmonics occur at integer multiples.

$$\begin{aligned} &\text{If } \frac{L^2 N}{B} >> 1 \\ &\text{Then } k_n L = n\pi \text{ for } n = 1, 2, \ldots \end{aligned} \tag{5.14}$$

If the bending energy dominates, then the eigenmodes are beam-like, and the resonance harmonics are

$$\begin{aligned} &\text{If } \frac{L^2 N}{B} << 1 \\ &\text{Then } k_n L = 4.730, 7.853, 10.996, \ldots \text{ for } n = 1, 2, \ldots \end{aligned} \tag{5.15}$$

Using the arguments above, we can now predict the resonance frequency for 1d beams of any size or geometry in the bending or stretching regimes.

2D Membranes

In the 2D membrane case, the frequency has vibrational harmonics along both x and y instead of just x. For simplicity, we assume that the membrane is very thin, so we can neglect the bending modulus, and the tension is isotropic. The resonance frequency is:

$$\omega_{nm} = k_{nm}\sqrt{\frac{N}{\rho}} \tag{5.16}$$

where the tension N is biaxial, and the clamping constant k_{nm} depend on the clamping in the x and y directions. For a square membrane of sidelength a, the eigenmodes are a superposition of sinusoidal waves along the x and y directions, giving clamping constants:

$$\begin{aligned} &k_{nm}a = \pi\sqrt{n^2+m^2} = 4.44, 7.02, 9.90, \ldots \\ &\text{for } n, m = 1, 2, \ldots \end{aligned} \tag{5.17}$$

For a circular membrane of diameter D, the eigenmodes are best described by spherical bessel functions that are quantized radially r and circumferentially θ. The resonance frequency is:

$$\omega_{r\theta} = k_{r\theta}\sqrt{\frac{N}{\rho}} \tag{5.18}$$

$$
\begin{aligned}
k_{11}D &= 4.81 \\
k_{12}D &= 7.64 \\
k_{13}D &= 10.29 \\
k_{21}D &= 11.4 \\
&\text{for } r, \theta = 1, 2, 3, \ldots
\end{aligned}
\tag{5.19}
$$

These equations predict the scaling of resonance frequency with membrane size and the relative position harmonics for 1D and 2D membranes. We can use them to interpret the mechanical resonance measurements of graphene membranes.

5.2 Graphene mechanical resonators

Four years ago, we made the first suspended graphene membranes and resonated them for the first time. Since then, many other research groups have started working in this field as well. Our techniques for fabrication and measurement as well as our understanding and control of the material have advanced rapidly. This rest of this chapter is a review of the previous experiments by our group and others on graphene resonators along with the measurement techniques that made them possible.

5.2.1 Opto-Mechanical Resonance Measurements

We used a resonance-modulated optical reflectance measurement developed by the Craighead and Parpia groups to actuate and detect the mechanical resonance of graphene membranes[46, 90]. Figure 5.3a shows a schematic of the setup used in this technique. The suspended graphene membrane sits on a x-y-z translation stage inside of a vacuum chamber under a pressure of $< 10^{-5}$ Torr. We shine two

incident lasers onto the graphene membrane, a 430 nm blue laser and a 633 nm red laser.

To actuate the graphene, we modulate the intensity of the blue laser, which heats and cools the graphene at the modulation rate. The heating causes thermal expansion and contraction, which strains the graphene and causes it to move. If we modulate the laser intensity at the correct frequency, we can drive the graphene into resonance. The red laser detects the mechanical motion by Fabry-Perot interferometry. As shown in Figures 5.3c-d), if the graphene membrane is near to a substrate, the light reflecting off the substrate and the membrane interferes. The amount of interference is very sensitive to the relative position of the membrane to the substrate. We can measure the change in position of graphene membrane by measuring intensity of the reflected light with a fast photodiode. The modulation of the drive laser and the response of the photo diode are controlled and measured using a network analyzer.

We also used the optical reflectance technique to measure the mechanical resonance of micron scale flakes of few-layer and single-layer graphene suspended over trenches in silicon oxide, which were fabricated using mechanical exfoliation. Figure 5.4a shows mechanical resonance of the 1.1 μm long and 1.9 μm wide doubly-clamped single-layer graphene shown in the inset. We fit the resonance to a Lorentzian line shape, predicted by the simple harmonic oscillator equation (Eq 5.6), to extract a resonance frequency of $f_0 = 70.5$ MHz, and a quality factor of $Q = 78$.

Figure 5.4b shows the resonance frequency of 33 resonators with thicknesses ranging from a single atomic layer to 75 nm thick. The frequencies of the fundamental modes vary from 1 MHz to 166 MHz with quality factors of 20-850.

In Figure 5.4b, we plot the fundamental resonance frequency versus t/L^2 for

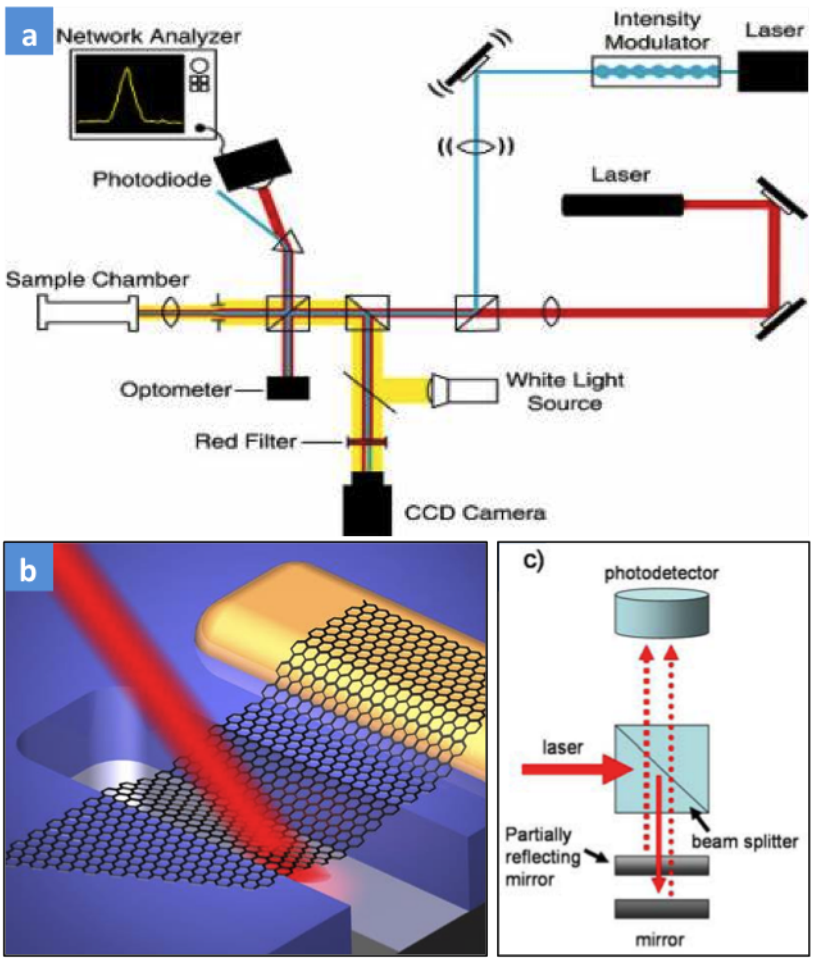

Figure 5.3: a) Schematic of optical interferometry measurement setup. b) The laser shines incident on to the graphene surface. Some of the light reflects off the graphene, some reflects of the substrate. c) A Fabry-Perot interfermetry setup. The graphene is the partially reflecting mirror.

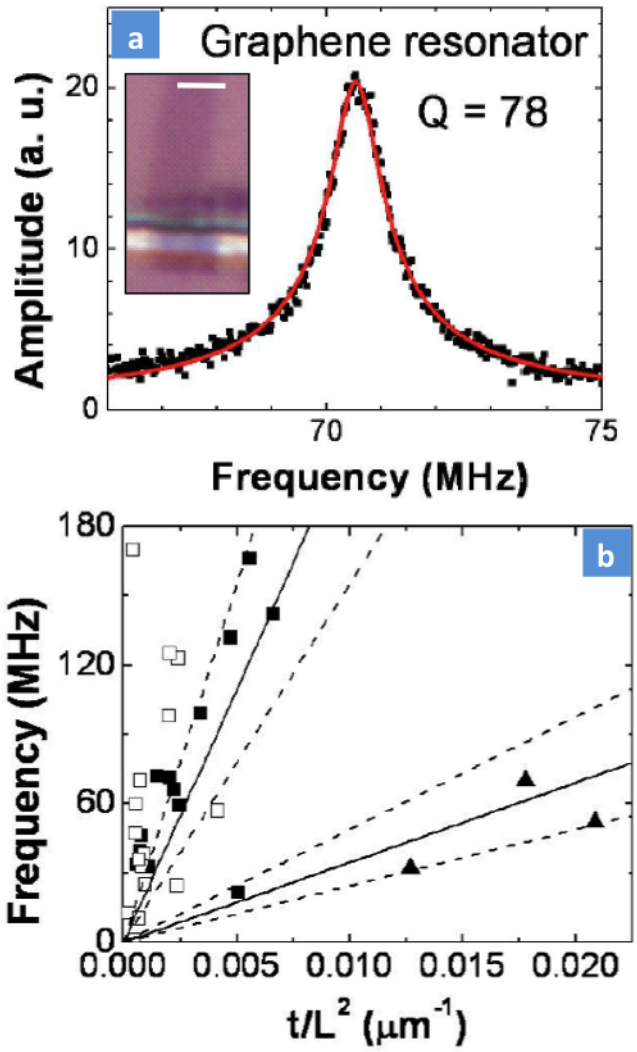

Figure 5.4: a) Mechanical resonance of 1.1 μm long suspended graphene device shown in the inset. Lorentzian fit gives a resonance frequency of $f_0 = 70.5$ MHz and $Q = 78$. b) Fundamental resonance frequency versus device size for few layer graphene in units of $\frac{t}{L^2}$. Dark boxes indicate graphene > 7 nm thick, and light boxes indicated graphene < 7 nm thick. Triangles indicate cantilevers. The lines indicate the expected resonance frequency of graphite sheets in the bending limit for both doubly clamped-beams and cantilevers.

33 suspended exfoliated graphene sheets thicknesses ranging from a single atomic layer to 75 nm thick. The line shows the predicted resonance frequency from Equation 5.10. We see that most of the resonators lie far above the curves expected for bending frequency of a rectangular beam. This suggests that the few-layer graphene sheets are usually under tension. However, we do not see any clear trend of resonance frequency or quality factor with size and shape.

The quality factors of graphene resonators which range from Q$\sim 20 - 850$ are low compared with other nanomechanical systems, which typically have quality factors of $\sim 10^3 - 10^4$ in vacuum. However, the graphene quality factor is similar to that found for single-walled carbon nanotube resonators, which display quality factors of 50-100 at room temperature[40], Nanotubes increase to 150,000 at 100 mK[91]. This similar behavior strongly suggests that the two systems share a common energy dissipation mechanism.

5.3 Imaging the Eigenmodes

In order to image the vibrational modes of graphene resonators, we started a collaboration with the Bachtold group. They had recenlty developed a scanned force measurement to measure the NEMS eigenmodes. As shown in Figure 5.5a, we scan a tapping mode cantilever over the surface of an electrically-contacted suspended graphene sheet. The cantilever measures both the topography of the surface and the amplitude of motion at the same time. The topography is measured by the usual feedback mechanism of atomic force microscopy at the fundamental mode of the cantilever. At the same time, the graphene is electrostatically driven at its resonance frequency f_{RF}. By modulating the amplitude of drive at the second harmonic frequency of the cantilever f_{Mod}, as shown in Figure 5.5b, the cantilever measures the difference in height of the graphene envelope in the driven

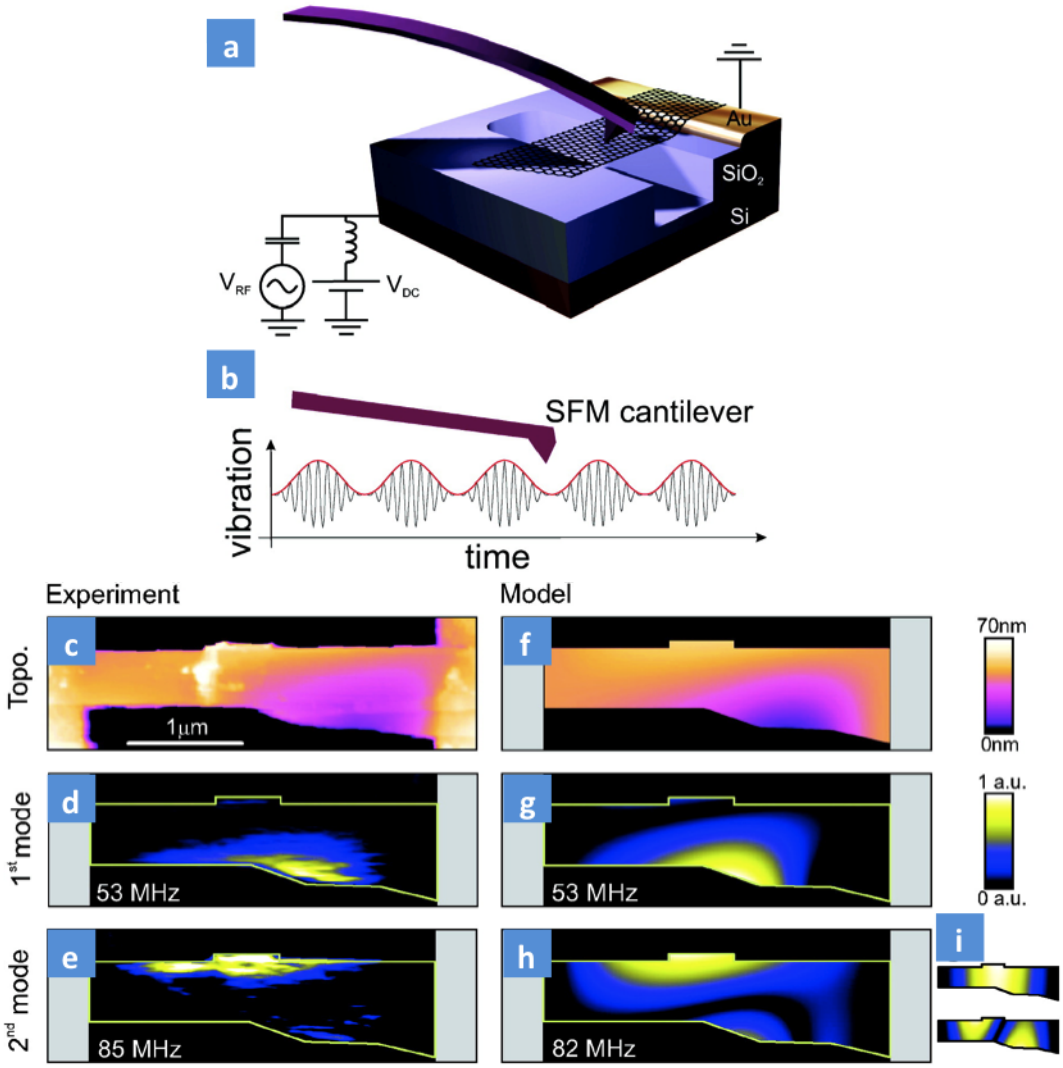

Figure 5.5: a) Schematic of suspended graphene sheet with SFM cantilever. b) Motion of the suspended graphene sheet as a function of time. A high-frequency term at f_{RF} is matched to the resonance frequency of the grpahene, and the resulting oscillation is modulated at f_{Mod}. c) Measured topographic height of the suspended graphene sheet. d-e) the measured amplitude of motion (colorscale) as a function of position for the first d) and second e) mode, which have a frequency of 53 MHz and 85 MHz respectively. f-h) Finite element model showing that we can reproduce the topology f), and eigenmode shapes g-h) and frequencies by assuming a small non-uniform in-plane strain at the clamping edge. i) Eigenmode shapes predicted by beam mechanics.

and undriven states, which is the amplitude of motion. We scan the cantilever over the surface to measure both the topography and amplitude of motion as a function of position.

Figurse 5.5d-e show the topography and first and second eigenmodes measured on a few-layer graphene membrane. The eigenmodes are are a maximum along the edge of the membrane and are very different from the shapes predicted for beams or membranes, shown in Figure 5.5i. Some resonators DO show the predicted shapes, but the majority show these edge modes. Figures 5.5f-h show that we can predict both the topography and shape and frequency of the eigenmodes by using a finite-element model and assuming a small non-uniform in-plane strain at the clamping edges of the membrane.

This measurement shows that mechanical resonance is extremely sensitive to the uniformity of the in-plane strain and symmetry of the clamping of the membranes. Because of small variations in the in-plane tension between different exfoliated devices, the graphene resonance shape and frequency is not predictable or reproducible. If we want to use graphene in applications, we need to improve this predictability and reproducibility by taking control of graphene membrane size, shape, thickness, clamping, and tension. We will show how to do this in Chapter 6.

5.4 Electrical detection of graphene resonance

We are not the only research group studying graphene resonators. The Hone group at Columbia and the Deshmukh group at ITC have shown that by using electrically contacted graphene similar to those shown in Figure 5.6a it is possible to drive and detect the graphene resonance electrically[17, 92]. We will use the same electrical mixing technique in the next chapter, so we give a detailed description here, before

we elaborate on the other groups findings.

5.4.1 Electrical resonance actuation and detection

The electromechanical mixing technique uses electrostatic actuation to drive the graphene and Amplitude Modulation (AM) or Frequency Modulation (FM) mixing detect the mechanical resonance[40, 93]. The AM technique is similar to the one Vera Sazonova developed to drive and detect carbon nanotube resonators. The FM version of this technique was developed by the Ayari group in France for carbon nanotube resonators. We use both AM and FM in Chapter 6, while the Hone and Deshmukh groups exclusively used the AM technique.

We use the setup shown in Figure 5.6b to perform the mixing resonance experiments. In all mixing experiments, we use a Lakeshore vacuum probe station, with four RF probes, on a temperature-controlled mount.

Electrostatic Actuation and Tuning

Using the circuit shown in Figure 5.6b, we apply a DC voltage V_{bg} to the back-gate of the suspended graphene, and a radio frequency voltage $V_{RF}(t)$ to the drain. The suspended graphene forms a capacitor C_{bg}, so applying a voltage causes the graphene membrane to be electrostatically attracted towards the back-gate:

$$F_{bg} = \frac{1}{2} C'_{bg} V_{bg}^2 + C'_{bg} V_{bg} V_{RF}(t) \tag{5.20}$$

where C'_{bg} is the capacitance derivative along the direction of motion.

$$C'_{bg} = \frac{dC_{bg}}{dz} \tag{5.21}$$

The static voltage tensions the graphene membrane and the RF voltage drives the sheet to resonate. By symmetry, the RF voltage can be applied either to the

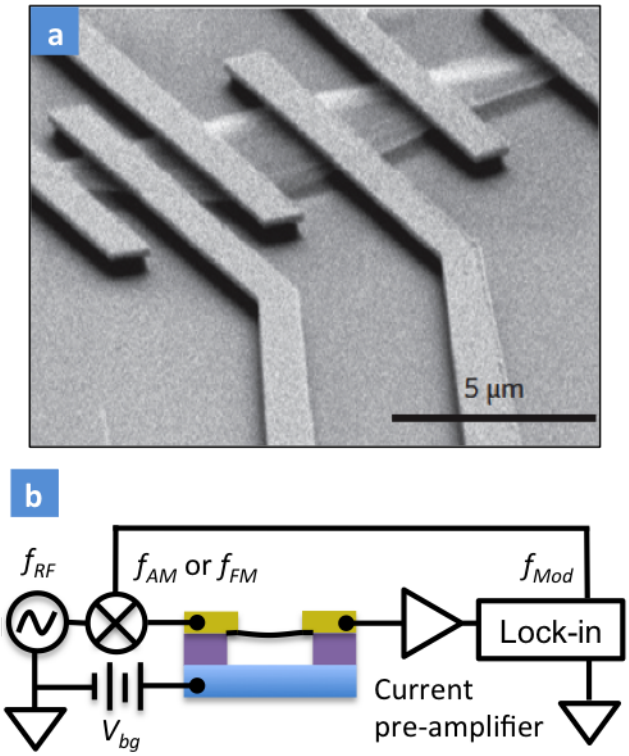

Figure 5.6: a) Electrically contacted suspended graphene membrane. b) Circuit diagram for electrical mixing setup.

gate or to the drain with similar results.

Electrical Mixing Detection

We detect the motion of the resonator by using techniques similar to those used in AM and FM radios, where a high frequency signal is detected by an antenna, and a circuit is used to bring the frequency down to audio frequencies. We take advantage of the semi-metal properties of graphene, where the conductance of the graphene sheet $G(V_{bg}, C_{bg})$ depends on both the applied voltage and gate capacitance. If the gate voltage changes, or the graphene moves, the conductance changes.

$$dG = \frac{\partial G}{\partial V_{bg}} dV_{bg} + \frac{\partial G}{\partial z} dz \tag{5.22}$$

However, it is difficult to directly measure the changes in conductance due to motion at RF because the signal is small and there is a large parallel capacitance in the system. We employ two related mixing techniques to bring the signal down to low frequency. Instead of applying a pure RF signal at the drain, we apply either an amplitude-modulated signal or a frequency-modulated signal

$$V_{AM} = \frac{V_{RF0}}{2}(1 + m\sin(2\pi f_{Mod}t))\sin(2\pi f_{RF}t) \tag{5.23}$$

or

$$V_{FM} = V_{RF0}\sin(2\pi(f_{RF} + f_{\Delta}\sin(2\pi f_{Mod}t)t) \tag{5.24}$$

where V_{RF0} is the drive amplitude of the resonator operating at radio frequency f_{RF}. The RF voltage is modulated at a frequency $f_{Mod} = 1$ kHz. The amplitude of modulation is typically $m = 1$ for AM, and $f_{\Delta} = 50$ kHz for FM in our measurements. We measure the current through the graphene with a lock-in amplifier at f_{Mod}. The total current measured using AM or FM mixing is

$$I_{AM} = \frac{1}{2}\frac{dG}{dq}(C_{bg}V_{RF0} + C'_{bg}V_{bg}Re(z^*(f_{RF}))V_{RF0}\cos(2\pi f_{Mod}t) \tag{5.25}$$

or

$$I_{FM} = \frac{1}{2}\frac{dG}{dq}(C'_{bg}V_{bg}\frac{Re(z^*(f_{RF}))}{df_{RF}}f_{\Delta}\cos(2\pi f_{Mod}t) \tag{5.26}$$

where dG/dq is the transconductance of the graphene, $z^*(f_{RF})$ is the complex amplitude of motion, and $Re(z^*(f_{RF}))$ is the real component of the complex amplitude that is in phase with the drive force

$$Re(z^*) = |z|\cos(\phi) \tag{5.27}$$

There are two important phenomenological observations to make about the mixing equations. First, the AM mixing current has a background due to the pure electrical mixing in the graphene, while the FM mixing current does not. Second, assuming a simple harmonic resonator response to the drive, the AM mixing technique gives a heartbeat shaped mixing response and the FM mixing technique gives a mode shape that is proportional to the derivative of the AM mode shape $\frac{dRe(z^*(f_{RF}))}{df_{RF}}$.

The really exceptional power of the electrical mixing technique is that, unlike many electrical detection techniques, it requires no knowledge of the frequency of the resonator and works perfectly over the entire tunable range of the resonator. In addition, it works well at low temperature and at very high frequency. The downside is that it is a low-bandwidth technique. It is necessary to measure over several modulation cycles of f_{Mod}, which makes it impossible to look at high frequency fluctuations.

The discussion of mixing presented here compares our mixing measurements to known techniques. For extensive derivations of the AM and FM mixing techniques for graphene and carbon nanotube resonators, see references[17, 16, 93].

5.4.2 Tuning the resonance

The Hone group showed that it is possible to electrostatically tune the graphene resonance by up to a factor of two, as shown in Figure 5.7a. In addition, they showed that it possible to tune both the resonance frequency and the quality factor by changing the temperature and by adding mass. In these experiments, they see the quality factor rise from $Q \sim 100$ at room temperature to $Q \sim 10,000$ at 4 K, as shown in Figure 5.7b. While the reason for this change is still not understood, it is very similar to behavior seen with carbon nanotube resonators.

5.5 Large-scale arrays

Other groups, led by the SNOW group at NRL, and the Spencer and Craighead groups at Cornell, have focused on producing many graphene membranes at a time. Before CVD graphene was discovered, the most promising candidates for producing large-scale graphene were epitaxial graphene and reduced graphene oxide from solution. The SNOW group found that it was possible to transfer reduced graphene oxide films onto a substrate, using techniques similar to those later used for single-layer graphene transfer[51]. By creating an array of holes on the target substrate, they were able to produce large arrays of suspended membranes with thicknesses of 2 nm to 20 nm, as shown in Figure 5.8a-b). These membranes were under tension and displayed surprisingly high quality factors of $Q < 3000$, shown in the inset of Figure 5.8b.

The Spencer group showed that it was possible to produce suspended membranes out of epitaxially-grown graphene on Silicon Carbide[94], as shown in Figure 5.8a. The group used an electrochemical etch to release films of few-layer graphene on the silicon carbide surface. Figures 5.8b-c) show that, since epitaxial graphene is under 0.1 % compression due to a lattice mismatch during growth, the

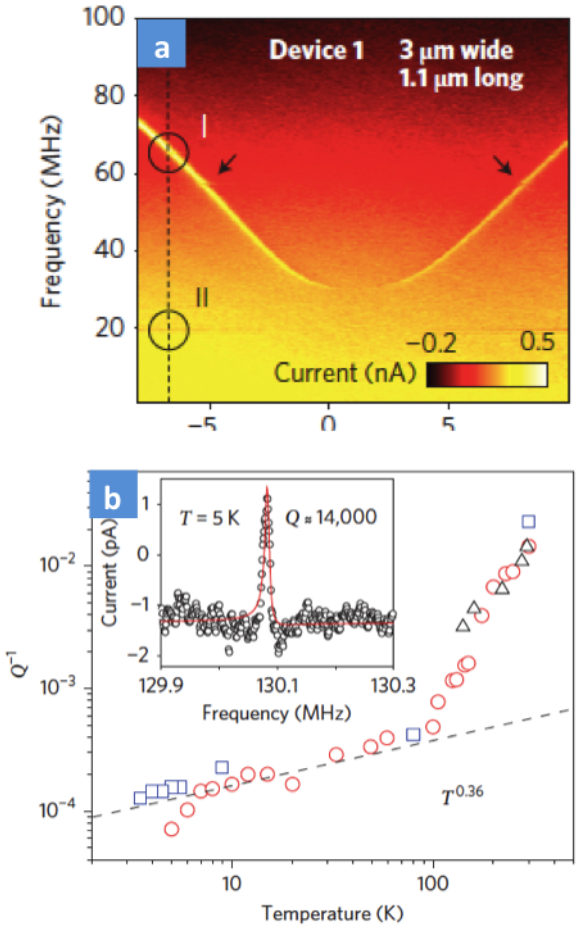

Figure 5.7: a) Electrically contacted, suspended, exfoliated graphene sheet. b) Electrostatic tuning of graphene resonance frequency. Resonance detected using electronic mixing[17]

graphene buckles out of plane by 100 nm when released from the surface. These buckled resonators cannot be under tension, yet they displayed frequencies much higher than expected for a flat beam of the graphene thickness. This is becausee the beams are buckled along both the length and width. This cross-sectional structure increases the bending modulus of the graphene membrane to much larger than that of a flat sheet.

The large array measurements show that both the frequency and quality factor are strongly affected by the boundary conditions and structure in the in the graphene membrane. They also showed that it is possible to create large arrays of few-layer graphene or graphene oxide membranes, taking graphene mechanics out of the experimental playground and into the realm of practical applications.

5.6 Conclusions

The first mechanical measurements on graphene happened less than 4 years ago, and the field has progressed rapidly since. The main lessons learned in the mechanical experiments on exfoliated graphene, reduced graphene oxide, and epitaxial graphene are that graphene is a high frequency, low mass, highly tunable resonator, which makes it an excellent material for use in nanomechanics. However, the resonance frequency is extremely sensitive to size, shape, clamping conditions, and in-plane tension, and the energy-loss mechanisms are still not well understood or controlled. In order to be of real use for applications, we need to understand and control all of the factors that affect the resonance. In the next chapter, we take the lessons learned and use them to make large numbers CVD grown single-layer graphene resonators, with reproducible and controllable resonances.

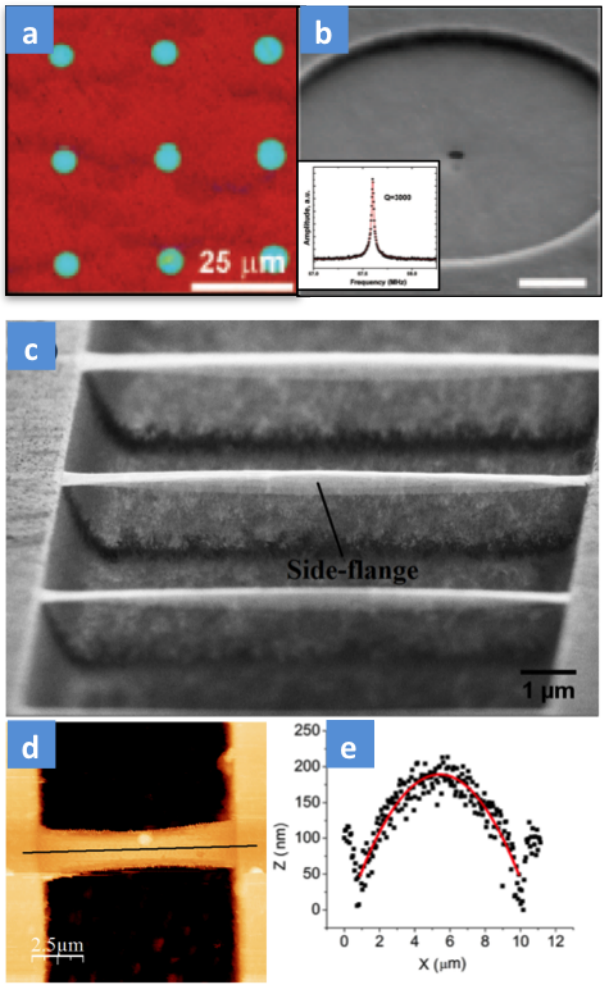

Figure 5.8: a) Optical image of circular membranes produced from reduced graphene oxide. b) SEM of a single reduced graphene oxide membrane. The hole was made using a FIB. Inset shows mechanical resonance with $Q = 3000$. c) Suspended multilayer graphene membranes on silicon carbide. d) AFM topographic image of one membrane. e) 1D cut along line shown in (d) shows that the graphene is buckled.

Chapter 6

Large-scale arrays of single-layer graphene resonators

This chapter is adapted from a paper that is currently in press in Nano Letters[63].

6.1 Introduction

When we look back at the early work on graphene mechanics, a couple of facts stand out. First, we can only make single-layer graphene resonators one at a time. Second, there is no control over the size, shape and, tension of the graphene resonators. In order to make graphene resonators useful in applications, and scientifically tractable, we need to take control over all of these parameters. Specifically, we want to make large arrays of identically-shaped and tensioned single-layer graphene. In this chapter, we show that, using the fabrication techniques described in Chapter 3, we can achieve this goal, and begin doing the first systematic studies of the mechanical resonance properties of single-layer graphene resonators as a function of size, clamping geometry, temperature, and electrostatic tuning. We find that the CVD graphene produces tensioned, electrically conducting, highly-tunable resonators with properties equivalent to exfoliated graphene. In addition, we find that clamping the graphene membrane on all sides reduces the variation in resonance frequency and makes the behavior more predictable.

6.2 Previous Work

Graphene, a single layer of carbon atoms bonded in a hexagonal lattice, is the prototypical two-dimensional membrane. Its unparalleled strength, small mass per

unit area, ultra-high aspect ratio, and unusual electronic properties make it an ideal candidate for nano-electro-mechanical systems (NEMS)[46, 12, 51]. Previously, graphene membranes could only be made in small batches using mechanical exfoliation[46, 12, 17, 92, 95, 5], growth on silicon carbide substrates[94], or as graphene oxide[51]. These techniques are all extremely limiting, as they produce either very small numbers of devices, multilayer graphene on conducting substrates, or resistive functionalized graphene. The ideal solution should produce large numbers of single-layer graphene membranes while maintaining exfoliated graphene's excellent electronic and mechanical properties.

6.3 Graphene Membranes

As we describe in Chapter 3, we started by using chemical vapor deposition to grow graphene on copper foil[6]. The graphene was verified to be predominantly single-layer ($> 90\%$) with low disorder by Raman microscopy and scanning electron microscopy (see Chapter 3.4.1)[15]. We fabricated three different device geometries shown in Figures 6a, 6.3a and 6.5a using variations on the graphene transfer technique developed by[6, 19, 28]. Type A membranes (Figure 6.1a-c) consist of graphene strips suspended over trenches and clamped at both ends (doubly-clamped) by the van der Waals adhesion of the graphene to the substrate. We fabricated Type A membranes by patterning the graphene into strips on the copper foil with photolithography and oxygen plasma then transferring the patterned graphene onto trenches on a 285 nm silicon oxide substrate. Type B membranes (Figure 6.3a) are square graphene membranes clamped on all sides. We fabricated these membranes by transferring un-patterned graphene onto a suspended silicon nitride membrane with square holes. Type C membranes (Figure 6.5a) are electrically contacted membranes suspended between two gold electrodes fabricated by

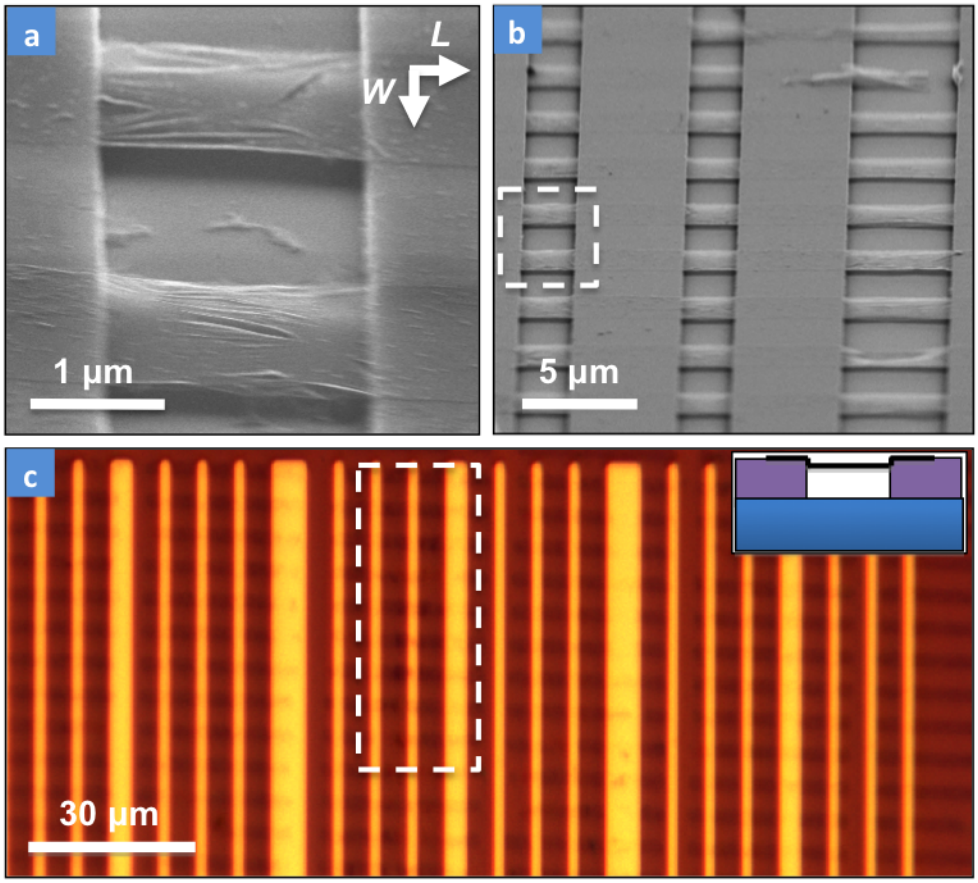

Figure 6.1: a) Angled SEM image of Type A suspended graphene membranes over trenches in silicon oxide. b) Array of graphene membranes (zoomed out from 1a). c) Optical image of large array of graphene membranes. Schematic of cross-section inset.

transferring un-patterned graphene to a 285 nm silicon oxide substrate, patterning the graphene into small bars, depositing gold electrodes on top, and suspending the graphene by wet etching the oxide out from underneath.

With all approaches, we produce hundreds to hundreds of thousands of single-layer suspended graphene membranes in each fabrication run. For Type A and C devices, we get yields of $> 80\%$ for membranes with $L < 3\mu$m and $W < 5\mu$m. For type B devices, we get yields of $> 90\%$ for membranes up to 5 μm on a side, with lower yields for membranes up to 30 μm on a side.

The suspended graphene membranes show complicated conformational structure, including small-scale (∼10 nm in amplitude) ripples such as those seen in Figure 6.1a, larger-scale (∼100 nm in amplitude) buckling of the membrane along the length and width. Ripples and buckling have also been observed in both exfoliated[95, 13] and epitaxial[94] graphene membranes due to in-plane tension, shear, or compression. The amount of rippling and buckling in our devices varies between neighboring membranes produced on a single chip, indicating that the tension, shear, and compression in the graphene membranes is variable. The degree to which this variability influences the resonator properties is addressed below. Finally, in larger membranes, occasional tears occur at mechanically weak grain boundaries between crystals in the CVD-grown graphene[72, 64].

To actuate and detect the mechanical resonance of the graphene membranes, we first used a resonance-modulated optical reflectance measurement[46, 90]. The membrane is actuated with a radio-frequency (RF) modulated 405 nm CW laser, and the mechanical motion is detected using interferometry of the reflected light of a 633 nm Helium-Neon laser. All optical measurements were performed at room temperature in vacuum with $p < 5 \times 10^{-5}$ Torr.

6.4 Doubly clamped graphene resonators

Figure 6.2a is a plot of the fundamental mode for a Type A membrane of length$L$ = 2 μm and width W = 3 μm. The resonance frequency is f_1 = 9.77 MHz and the quality factor is Q = 52. Figure 6.2b-d shows the frequency and quality factor of the fundamental mode for 38 identically-patterned membranes measured along a single trench. Figure 6.2b-c are histograms of the resonance frequencies and quality factors. There is a clear peak in the histogram at $f_1 \sim 15$ MHz, with a spread of 8 MHz. The quality factors range from 25-250, with a peak at 70.

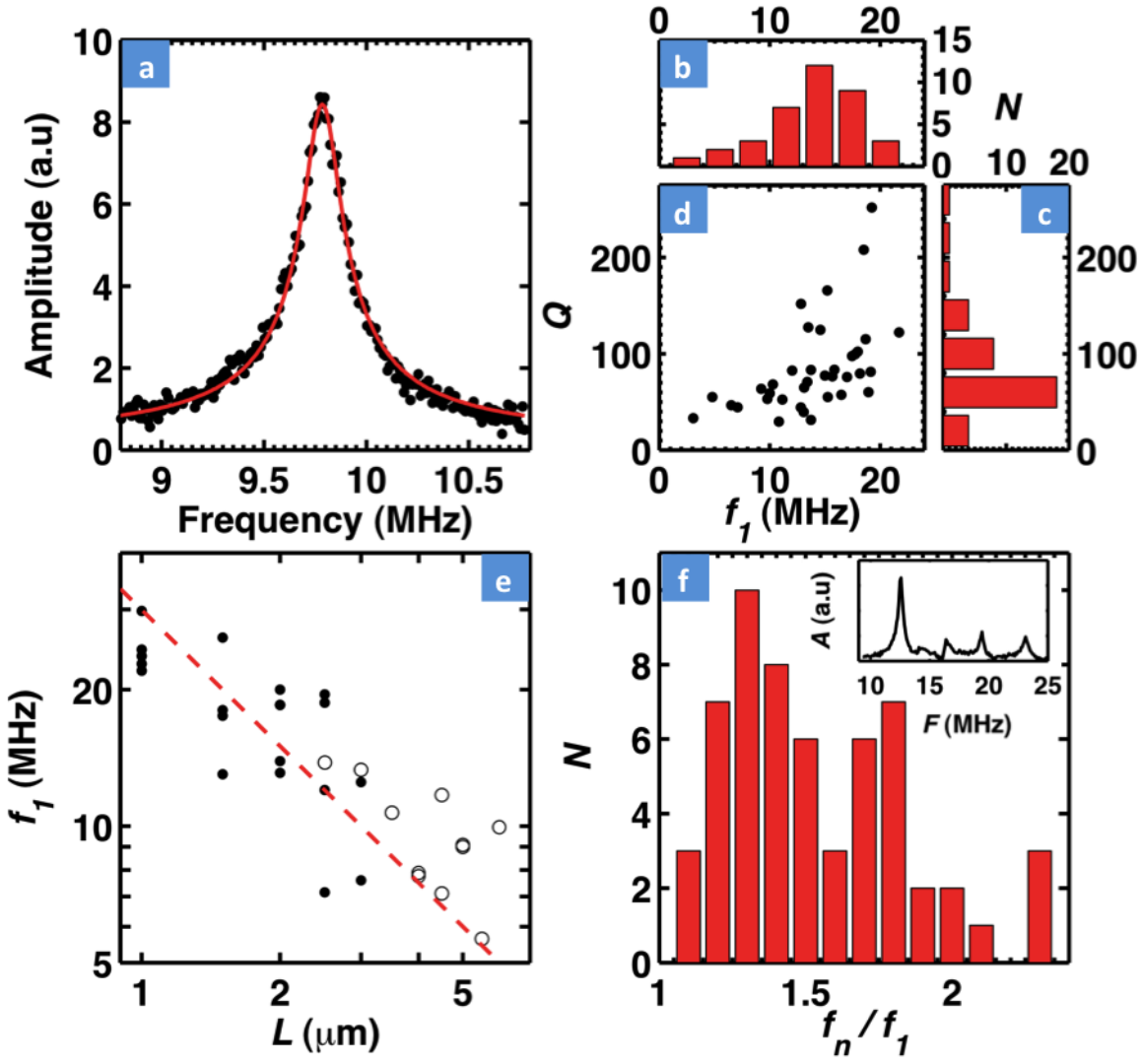

Figure 6.2: a) Optical interferometry measurement of a fundamental mode for a Type A graphene resonator like those shown in Figure 6a. L = 2 μm, W = 3 μm. Histogram of the frequency b), and quality factor c) of fundamental modes for 38 identical Type A resonators along a single trench L = 2 μm, W = 3 μm. d) Quality factor versus resonance frequency for the same devices as Figure 6b-c. e) Fundamental mode frequency versus length. Solid dots are membranes with widths W between 2.5 and 5 μm, open circles are membranes with partial tears in them. f) Histogram of measured higher modes divided by the fundamental mode for same devices as Figure 6.2b-d. Typical resonance spectrum inset.

Figure 6.2d shows that higher frequency is correlated with higher quality factor. These resonators are nominally identical so the variation is due to either differences in adsorbed mass or the strain and conformational structure of the membranes. Figure 6.2e shows f_1 versus L for Type A doubly-clamped membranes with L between 1 and 6 μm and W between 2.5 and 5 μm, plotted on a log-log scale. The resonance frequencies decrease with length and show no discernable dependence on the width. For reference, the dashed line shows an L^{-1} dependence. The black dots represent graphene membranes without tears, while the squares represent partially torn membranes. Interestingly, the torn membranes show similar behavior to the un-torn membranes. The simplest model of a doubly-clamped graphene membrane resonator is as a sheet under tension[46, 12, 17, 92, 5]:

$$f_n = \frac{n}{2L}\sqrt{\frac{Y}{\rho_0}\frac{s}{\alpha}} \tag{6.1}$$

where $Y = 340$ N/m and $\rho_0 = 7.4 \times 10^{-7}$ kg/m^2 are the in-plane stiffness and density of single-layer graphene, $n = 1, 2, 3, \ldots$ is the mode number, s is the in-plane uniaxial strain, and $\alpha = \rho_{total}/\rho_0$ is the adsorbed mass coefficient. Previous results[17, 92, 5] have shown the ratio of the contamination mass to the membrane mass can be large, typically varying between 1 and 10. This model predicts a L^{-1} scaling of the resonance frequencies with length, consistent with the data. From a best fit to the data in Figure 6.2c, we extract the average strain per absorbed mass ratio on the resonators of $s/\alpha \sim 10^{-5}$. This value is comparable to previously measured strains on exfoliated graphene membranes[17, 92, 5]. The strain likely results from the self-tensioning of the graphene as the van der Waals attraction adheres the membrane to the walls of the trench, as shown schematically in the Figure 6 inset[5, 96, 97].

The tensioned-membrane model predicts a second harmonic at twice the fre-

quency of the first. Figure 2f shows the measured higher resonant modes of the identical devices, normalized by the fundamental mode frequency with one example spectrum in the inset. Instead of a peak at 2 f_1, there is a broad distribution in frequencies with peaks around $f_n \sim 1.3 f_1$ and $1.6 f_1$. These most likely correspond to transverse modes or edge modes in the resonator due to non-uniform strain in the resonator. Previous experiments[95] discussed in Section 5.3 have shown that local modes can exist at the edges of exfoliated graphene resonators and the frequencies of these modes are difficult to estimate without a detailed knowledge of the structure in the transverse direction.

6.5 Fully clamped graphene resonators

In order to test the hypothesis that the transverse properties are important, we fabricated and measured the resonance in the Type B membranes shown in Figure 6.3a, where the membrane is clamped on all sides and the transverse modes are identical to the longitudinal ones. Figures 6.3(b-c) show that we observe higher resonant modes at frequencies approximately 1.5 and 2 times the fundamental mode. This result is consistent with the expected values of $f_{21} = 1.58 f_{11}$, and $f_{22} = 2 f_{11}$ predicted for a square membrane of uniform tension clamped on all sides:

$$f_{nm} = \frac{\sqrt{n^2 + m^2}}{2D} \sqrt{\frac{Yt}{\rho_0} \frac{S}{\alpha}} \tag{6.2}$$

With the fully clamped membranes, the reproducibility is also improved, with frequencies of 16.5, 18.8, 19.4, and 19.8 MHz measured for 4 nominally identical devices, which is a spread of less than 15 percent. The frequency also scales as approximately the inverse of the membrane dimension, as shown in Figure 6.3d. The quality factors are also higher, with $Q > 200$ though noise prevents a more accurate determination. Full clamping clearly improves the device reproducibility

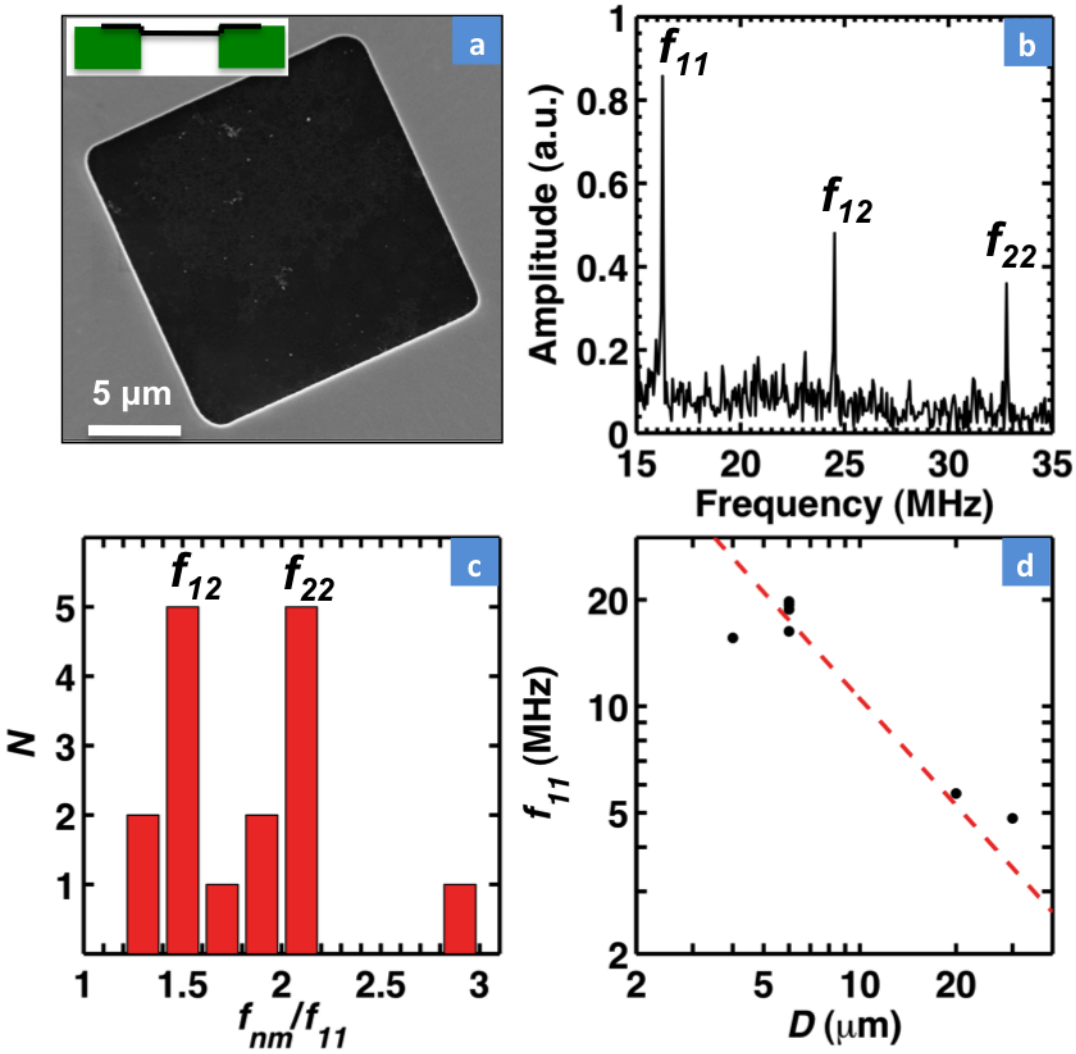

Figure 6.3: (a) SEM of a Type B square graphene membrane on a suspended silicon nitride membrane. Without a substrate behind the graphene to adjust the contrast, the absorbed mass contamination is clearly visible on the graphene. (b) Typical spectrum for a Type B square membrane. (c) Histogram of measured higher modes divided by the fundamental mode for square membranes. Higher modes occur at predictable intervals for square membranes. (d) Fundamental mode frequency versus side length D for square membranes.

and quality factors over those observed in doubly-clamped membranes, likely by eliminating soft degrees of freedom associated with the free edges.

6.6 Tuning the frequency and quality factor

As discussed in Section 5.4, some of the most exciting properties of exfoliated graphene resonators are their ability to be actuated and detected electrically[17], their large voltage-tunable frequency range and their high quality factor at low temperature ($Q \sim 10,000$ for exfoliated graphene at 4 K[17]. We explored these aspects of CVD graphene resonators by fabricating the Type C electrically-contacted resonators shown in Figure 6.4a. Transport measurements show these devices have mobilities of 1000-4000 cm^2/Vs, similar to previous results on CVD graphene[6, 52].

Using the electromechanical mixing measurement reported by Chen et al[17], we actuated the resonators electrostatically and measured the motion using Amplitude Modulation (AM)[17, 40, 16] or Frequency Modulation (FM)[93] mixing, as described in Section 5.4.1. Figure 6.4b shows the electrical mixing response versus drive frequency for AM (blue) and FM (green) mixing techniques, with back gate voltage $V_{bg} = 3$V, and drive $V_{rf} = 7$ mV. Both techniques yield a resonator frequency $f_1 = 19.2$ MHz and quality factor of Q = 44 at this gate voltage.

Figure 6.5c shows the FM mixing current as a function of the drive frequency and electrostatic gate voltage at room temperature. The resonance frequency increases by more than a factor of 2 for large V_{bg} and is symmetric around a minimum close to $V_{bg} = 0$, which is very similar to the behavior previously reported for exfoliated graphene[17, 92].

Figures 6.5(d-f) show the tuning of the same resonance at $T = 200$ K, 150 K, 100 K. As the temperature is decreased, the frequency of the resonator at $V_{bg} = 0$ rises, while the dependence of the resonance frequency on V_{bg} becomes weaker, and

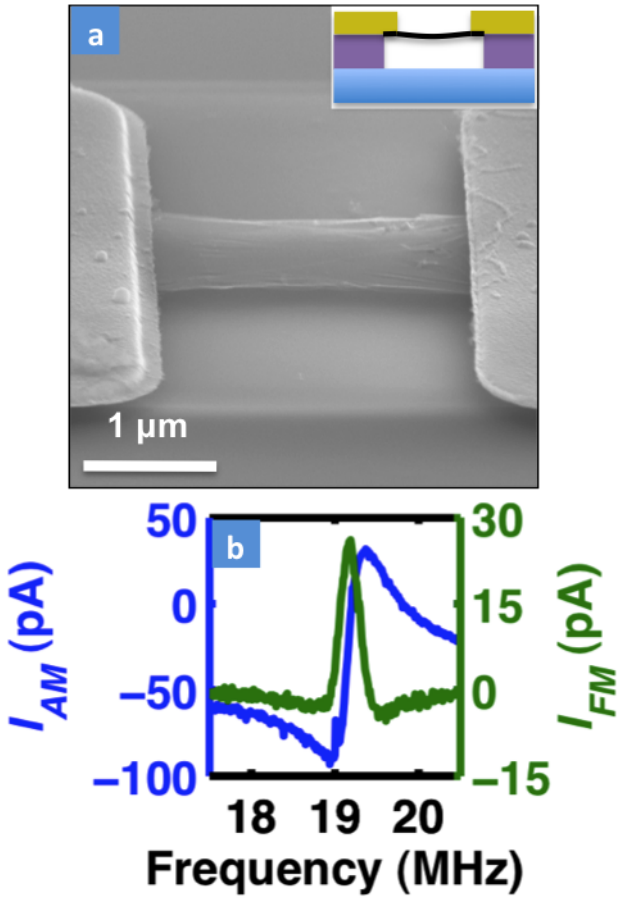

Figure 6.4: a) Angled SEM image of an electrically isolated suspended graphene clamped to gold electrodes. Schematic of cross-section inset. b) Electrical mixing measurement of mechanical resonance of membrane shown in (a) versus frequency, measured using AM (blue) and FM (green) mixing techniques for $V_{bg} = 3$ V, $V_{rf} = 7$ mV.

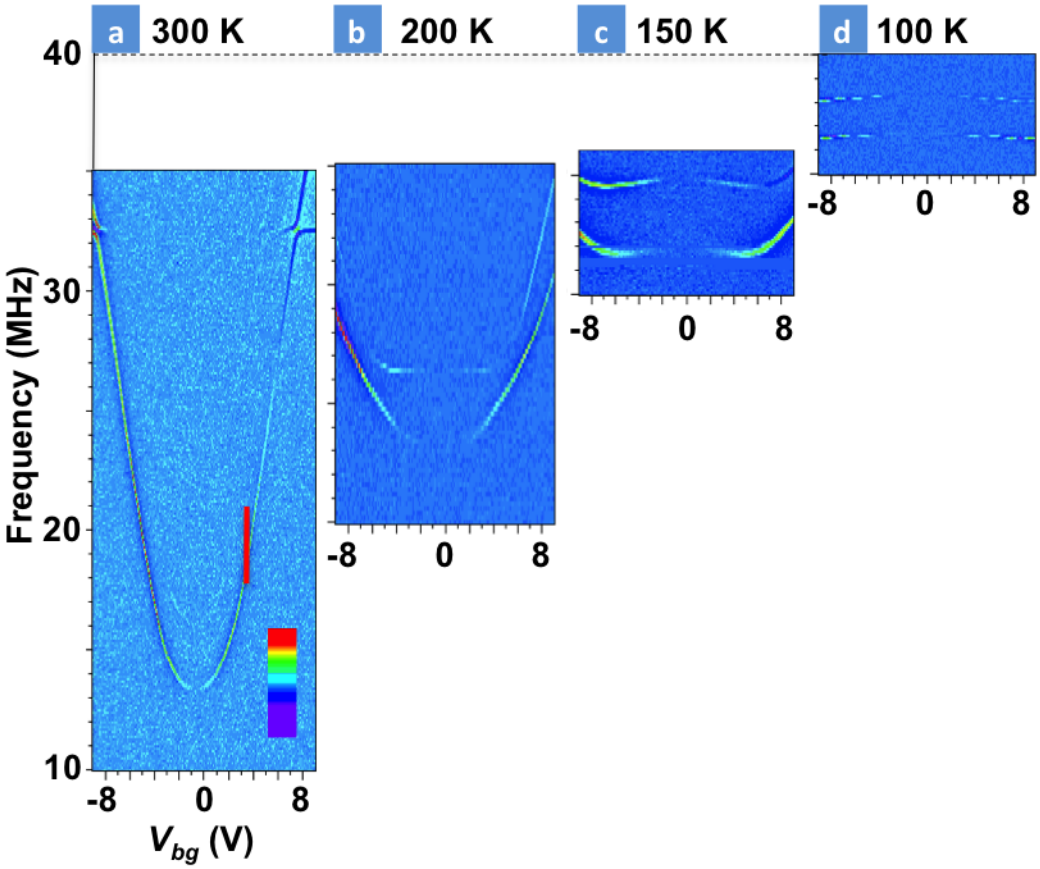

Figure 6.5: a) FM mixing signal (colorscale = -100 pA to 100 pA) versus gate voltage and drive frequency at room temperature. The resonance frequency is tuned by the electrostatic gate voltage. The red line indicates cut taken to get FM data shown in Figure 6.4b. b-d) show the evolution of the tuning for the same resonator at T = 200 K, 150 K, and 100 K respectively.

even reverses sign at 100 K. The change of frequency tunability with temperature is due to changes in the tension of the graphene as it is cooled and is similar to that seen in exfoliated graphene resonators[17, 92]. Figure 6.6 shows the inverse quality factor of a resonator versus temperature for a fixed $V_{bg} = 3$ V. The inset shows the frequency versus temperature over the same temperature range. As the temperature is decreased, the quality factor rises dramatically from 150 at room temperature to 9000 at 9 K. This is comparable to the highest quality factors reported for graphene resonators at that temperature[17].

From Figure 6.6, the inverse quality factor scales approximately as T^{α} where $\alpha = 0.35 \pm 0.05$ from 9 K up to 40 K, and as T^{β} where $\beta = 2.3 \pm 0.1$ from 40 K to room temperature. The temperature scaling is similar to what is found for exfoliated graphene resonators[17]. Similar temperature dependence is also seen in carbon nanotube resonators[91, 16]. While there are many theories examining dissipation in these systems[98, 99, 100, 101] the observed behavior is still not understood.

6.7 Conclusions

The techniques described here provide a step towards practical graphene-based devices. Our results show that it is possible to fabricate large arrays of low mass, high aspect ratio, CVD-grown single-layer graphene membranes while maintaining the remarkable electronic and mechanical properties previously observed for exfoliated graphene. This is an important conclusion, demonstrating that the benefit of wafer-scale processing allowed by CVD graphene comes at little or no cost in mechanical resonator performance. We further show that clamping the membrane on all sides improves resonator performance and reproducibility. The wafer-scale production of low-mass, high-frequency, and highly-tunable nanomechanical mem-

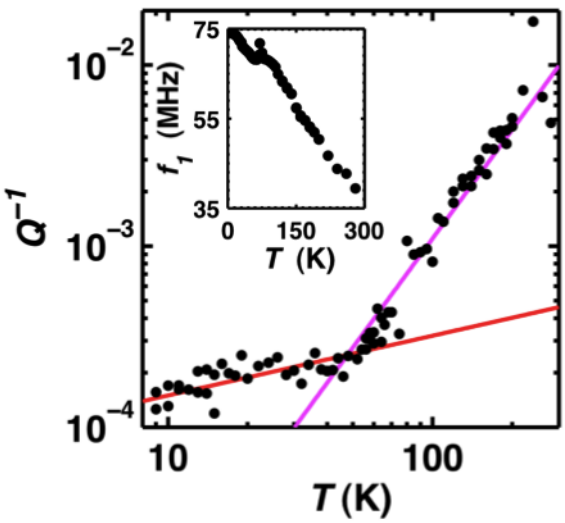

Figure 6.6: Inverse quality factor versus temperature at a $V_bg = 3$V, red and magenta lines show data scales as $T^{1/3}$ and $T^{2.3}$ respectively. Frequency versus temperature is inset.

brane resonators opens the way for applications in areas from sensing to signal processing.

Chapter 7

Conclusions

7.1 Summary

Over the course of this thesis, we took the new 2D material of graphene and found that we were able to use mechanical exfoliation to suspend it over a trench for the first time to form a doubly-clamped drumhead with thicknesses down to a single layer of atoms. This fact was impressive, because at first we were not sure that an unsupported single layer of atoms was even possible[102]. We went on to show that it was also possible to resonate the single layer of atoms. We found that graphene resonators had frequencies in the megahertz, and had quality factors of around 100. Unlike most thin flims, the strength of the material did not degrade as it was thinned down to a single layer of atoms. We then addressed two big problems that were holding us back from learning more.

First, we could not find any relation in frequency and quality factor between different resonators. Further experiments studying the shape of the eigenmodes of the resonator taught us that the reason for the unpredictability of the resonators was that small non-uniformities in the in-plane tension changed the shape of the eigenmodes from the predicted doubly-clamped beam modes to modes where the motion was greatest along the free edges.

Second, we could only make the resonators one at a time using mechanical exfoliation. The amount of work of producing multiple membranes kept us from being able to do systematic studies or integrating the graphene into more complicated devices, like electrically-contacted suspended membranes.

The solution to these two problems came in the form of CVD-grown single-layer graphene. Using CVD graphene, we adapted techniques used by other groups

making graphene-based electrical devices to start making novel suspended single-layer graphene membranes of arbitrary size and shape, with or without electrical contacts. These devices are currently state-of-the-art. We used the new devices for two purposes.

First, we used the CVD membranes to study the structure, growth mechanisms, and properties of CVD-grown graphene to see how it is different from exfoliated graphene. Using electron microscopy, we found that CVD-grown graphene is poly-crystalline, with many grains of different size and crystal orientation. The grains of different crystal orientation stitched themselves together with a disordered line of 5-7 defects. The grains grow out of nucleation sites with many grains growing out of each nucleation site. By changing the CVD growth conditions, we were able to change the average grain sizes from 250 nm to 1-4 μm by changing the CVD growth parameters. Grains of different crystal orientation met at preferred low angles ($\sim 7^\circ$) and high angles ($\sim 30^\circ$).

We probed the mechanical properties of the grain boundaries by pushing on the CVD graphene membranes with an AFM tip. We found that the graphene broke at loads of 100 nN, compared with 1.7 μN breaking load of pristine graphene. By imaging the membranes before and after, we saw that the graphene was tearing along the grain boundaries. We probed the electrical properties of CVD graphene by performing transport and scanned probe measurements. We found that we could dramatically change the room temperature mobility of the CVD graphene from 400-4000 to 8000-10,000 by changing the growth conditions. However, we found that larger grains were not directly correlated with larger mobilities. Finally, we probed the electrical resistance of the grain boundaries with AC-EFM and found that grain boundaries had resistance $R_{GB} < 60\ \Omega\mu m/L$, where L is the length of the grain boundary.

Second, we used the CVD-grown single-layer graphene membranes to do systematic studies of the mechanical resonance as a function of size, clamping, tension, and temperature. We found that while the polycrystalline grain boundaries affect the ultimate strength of the graphene, they do not observably affect the mechanical resonance. The doubly-clamped graphene resonators had frequencies in the megahertz, and quality factors of 25-150. We found that the graphene membranes are under tension with a strain of $\frac{s}{\alpha} = 10^{-5}$, where alpha is the adsorbed mass factor, usually between 1-10. We found that by clamping the membranes on all sides, we were able to improve the the reproducibility of identical membranes and the predictability of the higher harmonics. We showed that we can use electrically-contacted membranes to make tunable graphene resonators, where we can tune the resonance frequency by more than a factor of 2. Finally, we measured the quality factor as a function of temperature, and found that the quality factor increased from ~ 150 at room temperature to $\sim 10,000$ at 8 K, similar to previous measurements on exfoliated graphene resonators[17] and carbon nanotubes[16, 91].

7.2 Outlook

We have made a lot of progress in our understanding and control over suspended graphene membranes. This new understanding and control is now leading to a wide variety of new, exciting experiments and has made graphene membranes useful for many new applications.

On the mechanics front, we have finally developed a level of control, where we can now start to unravel some of the questions that have been plaguing us for a long time, and begin to use suspended graphene membranes in new applications in nanomechanics.

We are able to start unraveling what dominant-loss mechanisms are causing the

surpisingly-low quality factor in graphene. The three experiments that are likely to have the most impact will be: 1) Do temperature dependent measurements on fully clamped graphene membranes; 2) Make a local gate to start measuring the thermal motion in the graphene membrane and measure the coupling between the different modes; And, 3) use large grain CVD membranes to put the graphene under very high tension. Previously, these experiments were largely fruitless because we were not able to assume anything about the graphene tension and eigenmodes and did not have control over the graphene we were producing.

We can now start using the graphene membranes for applications like RF processing and mass sensing, for which it has long shown great promise. By putting a local gate onto a fully clamped membrane, we should be able to produce high frequency, high quality factor, tunable graphene resonators, which will be extremely useful in chemical sensing applications.

On the graphene growth front, we have only just begun to understand the properties of grain boundaries in CVD graphene. These systems are a new form of 1D electronic system, embedded into 2D graphene. While in our experiments, we did not see that the grain boundaries have large resistance compared with the graphene bulk, we were looking at the effects of many grain boundaries added together. There are some really interesting potential experiments exploring the electrical and mechanical properties of an isolated grain boundary and looking at how the properties change as a function of the angle at which grains meet.

There is a lot left to do to understand how the growth process affects the properties of CVD graphene. For most applications, we need pristine graphene. Now that we have developed the tools for studying polycrystalline graphene, we need to use them to unravel the growth mechanisms of CVD graphene and control the growth to fabricate larger graphene grains.

Taking an even wider view, we can use the techniques that we have developed to incorporate graphene into many other nanoscale technologies and to start studying other 2D materials.

For example, one can now start reasonably thinking about integrating graphene with photonic waveguides[8], microfluidic systems, single-electron transistors, and Qubits[9], or as the active element in an optomechanical membrane in the middle system[103].

In addition, there are many other 2D layered materials other than pure graphene that we have yet to understand. Some materials exist naturally, like hexagonal boron-nitride[77], while others are made by chemically functionalizing graphene like fluorinated graphene[104, 105]. In either case, we have developed tools for looking at everything from the structure of these new materials, to what happens to these new materials electrically, optically, and mechanically as they are thinned down to a single layer of atoms. Even more exciting is the possibility of making composite systems by layering insulating and conducting materials on top of each other[36].

BIBLIOGRAPHY

[1] Y.-M. Lin and P. Avouris, Nano Letters **8**, 2119 (2008), PMID: 18298094.

[2] S. Bae et al., Nature Nanotechnol. **5**, 574 (2010).

[3] G. F. Schneider et al., Nano Letters **10**, 3163 (2010).

[4] S. Garaj et al., Nature **467**, 190 (2010), 10.1038/nature09379.

[5] J. S. Bunch et al., Nano Letters **8**, 2458 (2008).

[6] X. Li et al., Science **324**, 1312 (2009).

[7] B. Ilic et al., Journal of Applied Physics **95**, 3694 (2004).

[8] G. S. Wiederhecker, L. Chen, A. Gondarenko, and M. Lipson, Nature **462**, 633 (2009).

[9] M. D. Lahaye, Science **304**, 74 (2004).

[10] A. K. Geim and K. S. Novoselov, Nature Mater. **6**, 183 (2007).

[11] R. R. Nair et al., Science **320**, 1308 (2008).

[12] C. Lee, X. D. Wei, J. W. Kysar, and J. Hone, Science **321**, 385 (2008).

[13] W. Bao et al., Nature Nanotech **4**, 562 (2009).

[14] J. R. Minkel.

[15] A. Ferrari et al., Phys. Rev. Lett. **97**, 187401 (2006).

[16] V. Sazonova, Cornell University Thesis (2006).

[17] C. Chen et al., Nature Nanotech , 1 (2009).

[18] P. Blake et al., Nano Letters **8**, 1704 (2008).

[19] K. S. Kim et al., Nature **457**, 706 (2009).

[20] J. Meyer, C. Girit, M. Crommie, and A. Zettl, Nature **454**, 319 (2008), 10.1038/nature07094.

[21] I. Forbeaux, J.-M. Themlin, and J.-M. Debever, Phys. Rev. B **58**, 16396 (1998).

[22] E. Loginova, N. C. Bartelt, P. J. Feibelman, and K. F. McCarty, New Journal of Physics **11**, 63046 (2009).

[23] J. S. Bunch, Y. Yaish, M. Brink, K. Bolotin, and P. L. McEuen, Nano Letters **5**, 287 (2005).

[24] K. S. Novoselov et al., Science **306**, 666 (2004).

[25] K. S. Novoselov et al., P Natl Acad Sci Usa **102**, 10451 (2005).

[26] Y. Zhang, Y.-W. Tan, H. L. Stormer, and P. Kim, Nature **438**, 201 (2005).

[27] K. Novoselov et al., Nature **438**, 197 (2005), 10.1038/nature04233.

[28] A. Reina et al., Nano Lett **9**, 3087 (2009).

[29] G. Bressi, G. Carugno, R. Onofrio, and G. Ruoso, Phys. Rev. Lett. **88**, 041804 (2002).

[30] A. O'Connell et al., Nature **464**, 697 (2010), 10.1038/nature08967.

[31] S. Bunch, Cornell University Thesis (2008).

[32] R. Saito, G. Dresselhaus, and M. Dresselhaus, *Physical Properties of Carbon Nanotubes*, Imperial College Press, London, England, 1998.

[33] E. Minot, Cornell University Thesis (2004).

[34] K. I. Bolotin, K. J. Sikes, J. Hone, H. L. Stormer, and P. Kim, Phys. Rev. Lett. **101**, 1 (2008).

[35] X. Hong, A. Posadas, K. Zou, C. H. Ahn, and J. Zhu, Phys. Rev. Lett. **102**, 136808 (2009).

[36] C. R. Dean et al., Nat Nano **5**, 722 (2010).

[37] S. Adam, E. H. Hwang, V. M. Galitski, and S. Das Sarma, PNAS **104**, 18392.

[38] B. T. Kelly, *Physics of graphite*, Applied Science, London Englewood, NH, 1981.

[39] E. D. Minot et al., Phys. Rev. Lett. **90**, 156401 (2003).

[40] V. Sazonova et al., Nature **431**, 284 (2004).

[41] I. W. Frank, D. M. Tanenbaum, A. M. V. D. Zande, and P. L. McEuen, J Vac Sci Technol B **25**, 2558 (2007).

[42] M. Poot and H. S. J. van der Zant, Appl. Phys. Lett. **92**, 3 (2008).

[43] C. Y. Wang, K. Mylvaganam, and L. C. Zhang, Phys. Rev. B **80**, 155445 (2009).

[44] E. Cerda and L. Mahadevan, Phys. Rev. Lett. **90**, 074302 (2003).

[45] P. Blake et al., Appl. Phys. Lett. **91**, 63124 (2007).

[46] J. S. Bunch et al., Science **315**, 490 (2007).

[47] M. Huang et al., P Natl Acad Sci Usa **106**, 7304 (2009).

[48] X. Liang, Z. Fu, and S. Y. Chou, Nano Letters **7**, 3840 (2007).

[49] F. Carbone, P. Baum, P. Rudolf, and A. H. Zewail, Phys. Rev. Lett. **100**, 035501 (2008).

[50] A. Sidorov et al., Nanotechnology **20**, 055611 (2009).

[51] J. T. Robinson et al., Nano Lett **8**, 3441 (2008).

[52] M. P. Levendorf, C. S. Ruiz-Vargas, S. Garg, and J. Park, Nano Letters **9**, 4479 (2009).

[53] L. Gao, J. R. Guest, and N. P. Guisinger, Nano Letters **10**, 3512 (2010).

[54] L. Zhao et al., arXiv:1008.3542v1 (2010).

[55] S. Chen et al., arXiv **cond-mat.mtrl-sci** (2010).

[56] X. Li, W. Cai, L. Colombo, and R. S. Ruoff, Nano Letters **9**, 4268 (2009).

[57] D. R. Lenski and M. S. Fuhrer, arXiv **cond-mat.mtrl-sci** (2010).

[58] S. Lee, K. Lee, and Z. Zhong, Nano Letters **10**, 4702 (2010).

[59] M. Ishigami, J. H. Chen, W. G. Cullen, M. S. Fuhrer, and E. D. Williams, Nano Letters **7**, 1643 (2007).

[60] E. Stolyarova et al., Nano Lett **9**, 332 (2009).

[61] W. Regan et al., Appl. Phys. Lett. **96**, 113102 (2010).

[62] A. A. Balandin et al., Nano Letters **8**, 902 (2008).

[63] A. M. v. d. Zande et al., Nano Letters **0** (0).

[64] P. Y. Huang et al., arXiv **cond-mat.mtrl-sci** (2010).

[65] J. Cervenka and C. F. J. Flipse, Physical Review B **79**, 195429 (2009).

[66] N. M. R. Peres, F. Guinea, and A. H. Castro-Neto, Physical Review B **73** (2006).

[67] O. V. Yazyev and S. G. Louie, **doi:10.1038/nmat2830** (2010).

[68] A. Mesaros, S. Papanikolaou, C. F. J. Flipse, D. Sadri, and J. Zaanen, arXiv:1007.1137 (2010).

[69] J. Cervenka, M. I. Katsnelson, and C. F. J. Flipse, Nature Phys. **5**, 840 (2009).

[70] S. Malola, H. Hakkinen, and P. Koskinen, Physical Review B **81**, 165447 (2010).

[71] Y. Liu and B. I. Yakobson, Nano Letters **10**, 2178 (2010).

[72] R. Grantab, V. B. Shenoy, and R. S. Ruoff, arXiv **cond-mat.mtrl-sci** (2010).

[73] O. V. Yazyev and S. G. Louie, Physical Review B **81**, 195420 (2010).

[74] P. Hirsch, A. Howie, R. Nicholson, D. W. Pashley, and M. J. Whelan, *Electron Microscopy of Thin Crystals*, Krieger Publishing Co., Malabar, FL, 1965.

[75] E. Cockayne et al., arXiv:1008.3574v1 (2010).

[76] J. M. Wofford, S. Nie, K. F. McCarty, N. C. Bartelt, and O. D. Dubon, Nano Letters **0** (2010).

[77] O. L. Krivanek et al., Nature **464**, 571 (2010).

[78] A. Hashimoto, K. Suenaga, A. Gloter, K. Urita, and S. Iijima, Nature **430**, 870 (2004).

[79] J. C. Meyer et al., Nano Lett. **8**, 3582 (2008).

[80] K. Suenaga et al., Nature Nanotechnology **2**, 358 (2007).

[81] J. Lahiri, Y. Lin, P. Bozkurt, I. I. Oleynik, and M. Batzill, Nature Nanotechnol. **5**, 326 (2010).

[82] V. W. A. de Villeneuve et al., Journal of Physics-Condensed Matter **17**, S3371 (2005).

[83] S. Park, H. C. Floresca, Y. Suh, and M. J. Kim, Carbon **48**, 797 (2010).

[84] X. Li et al., Nano Letters **10**, 4328 (2010).

[85] A. Bachtold et al., Physical Review Letters **84**, 6082 (2000).

[86] S. Thiel et al., Phys. Rev. Lett. **102**, 46809 (2009).

[87] K. L. Ekinci, J. Appl. Phys. **95**, 2682 (2004).

[88] K. L. Ekinci and M. L. Roukes, Rev. Sci. Instrum. **76**, 061101 (2005).

[89] S. Timoshenko and D. Young, New York, John Wiley and Sons, Inc (1974).

[90] D. W. Carr, L. Sekaric, and H. G. Craighead, J. Vac. Sci. Technol. B **16**, 3821 (1998).

[91] A. K. Huttel et al., Nano Lett **9**, 2547 (2009).

[92] V. Singh et al., arXiv **cond-mat.mes-hall** (2010).

[93] V. Gouttenoire et al., Small **6**, 1060.

[94] S. Shivaraman et al., Nano Lett **9**, 3100 (2009).

[95] D. Garcia-Sanchez et al., Nano Letters **8**, 1399 (2008).

[96] T. Hertel, R. E. Walkup, and P. Avouris, Physical Review B **58**, 13870 (1998).

[97] R. S. Ruoff, J. Tersoff, D. C. Lorents, S. Subramoney, and B. Chan, Nature **364**, 514 (1993).

[98] C. Seoanez, F. Guinea, and A. H. Castro, Physical Review B **76**, (2007).

[99] S. Y. Kim and H. S. Park, Appl. Phys. Lett. **94**, 101918 (2009).

[100] H. Jiang, M.-F. Yu, B. Liu, and Y. Huang, Phys. Rev. Lett. **93**, 185501 (2004).

[101] J. Lischner and T. A. Arias, arXiv **cond-mat.mes-hall** (2010).

[102] J. C. Meyer et al., Nature **446**, 60 (2007).

[103] J. Sankey, C. Yang, B. Zwickl, A. Jayich, and J. Harris, Nat Phys **6**, 707 (2010), 10.1038/nphys1707.

[104] R. R. Nair et al., arXiv **cond-mat.mtrl-sci** (2010).

[105] J. T. Robinson et al., Nano Letters **10**, 3001 (2010).